Optical Properties of Free Tropospheric Aerosol Particles Related to the Relative Humidity as Derived from Raman Lidar Observations at Nagoya: Contributions of Aerosols from the Asian Continent and the Pacific Ocean

(ラマンライダーによって観測された名古屋上空
自由対流圏エアロゾルの光学的性状とその湿度特性:
アジア大陸と太平洋上から輸送されるエアロゾルの寄与)

Tetsu Sakai

酒井哲

要旨

太平洋に近接するアジア地域における自由対流圏エアロゾルの光学的性状とその湿度特性を明らかにするために、ラマン散乱を利用したレーザレーダによるエアロゾル後方散乱・消散係数、偏光解消度（非球形性の指標）と湿度の鉛直分布を同時測定するデータ解析方法を開発し、１９９４年－１９９７年の期間、名古屋（３５.１°N, １３７.０°E）において観測を行った。観測されたエアロゾルの光学的特性と相対湿度、またエアロゾル発生源地域からの輸送経路との対応について解析を行った結果、以下に示すエアロゾル光学的性状の湿度特性と輸送経路との対応が明らかになった。

１９９４年４月１７日における３０分間の連続観測において、高度１.０－２.２kmの領域のエアロゾル光学パラメータに顕著な時間変化が観測された。この領域では湿度の増加とともにエアロゾル散乱比が増加・偏光解消度が減少しており、高湿度大気中でエアロゾルの後方散乱断面積がより大きくかつ球形性が高いことを示した。またこの領域における相対湿度の変化範囲（１３％－３８％）が対流圏の代表的な潮解性エアロゾルの相変化点（固体－液体）に近いことから、観測された時間変化がエアロゾルの吸湿性を反映したものであると推測された。一方高度２.２－３.５kmの領域では、相対湿度が高度１.０－２.２kmの領域の最高値と同程度（~３５％）で高偏光解消度を示した。このことは、２つの高度領域に異なる組成（吸湿性）あるいは湿度履歴をもったエアロゾルが分布していたことを示唆する。

１９９４年３月から１９９７年２月の観測において、高度２－８kmの領域でのエアロゾル光学的特性に以下の季節変動が観測された。エアロゾル後方散乱係数の高度積分値は、２－４kmと４－８kmの両高度領域で春期（３－５月）に鋭いピークとともに年間の最大値が観測された。春期の３ヶ月平均値は、高度２－４kmで年平均値の１.６－２.２倍、高度４－８kmで１.６－１.８倍であった。また高度２－４kmでは夏期中後半（７－８月）に第２極大が観測された。

エアロゾル偏光解消度は、春期の高度２－８kmで頻繁に、また秋期（９－１

１月）と冬期（１２－２月）の高度４－８kmでしばしば２５％程度の高い値が観測された。またこれらの季節の高度４－８kmでは相対湿度約８０％の高湿度で高偏光解消度が観測されたことから、鉱物などの非水溶性の非球形粒子の存在が示唆された。これらの領域の空気塊の多くは、偏西風によってアジア大陸上を通過して来ており、アジア大陸ソースの影響を強く受けていたと考えられる。夏期（６－８月）の高度２－８kmと秋期の高度２－４kmでは、５％以下の偏光解消度が広い相対湿度範囲で観測され、また１０％以上の偏光解消度が相対湿度５０％以下の領域でのみ観測された。このことから水溶性粒子（硫酸液滴など）や潮解性粒子（硫酸塩、海塩など）の卓越が示唆された。これらの領域の空気塊の多くは、太平洋高気圧の循環に伴い太平洋上を通過して来ていたことから、太平洋ソースの影響を主に受けていた考えられる。冬期の高度２－８kmでは、５％以下の偏光解消度が相対湿度２０％以下で頻繁に観測されたことから、水溶性粒子の卓越が示唆された。この領域の空気塊は主にアジア大陸上を通過して来ていた。これらの結果は、エアロゾル発生源地域であるアジア大陸・太平洋からの空気塊の輸送経路とその場の相対湿度が、名古屋上空自由対流圏のエアロゾル偏光解消度を主に規定していることを示している。

以上の結果から、名古屋上空における自由対流圏エアロゾルの光学的性状が、エアロゾル発生源地域（アジア大陸・太平洋）からの空気塊の輸送経路とその場の相対湿度によって強く規定されていることが明らかになった。

Abstract

We have developed the Raman lidar system and the data analyzing procedure that simultaneously measure the vertical distributions of humidity, aerosol backscattering, extinction, and depolarization ratio (particle nonsphericity) in the troposphere. The measurements were carried out at Nagoya (35.1°N, 137.0°) from 1994 to 1997 to study the aerosol optical properties in the free troposphere over the Asian Pacific Rim region. The relation of the observed aerosol properties to ambient relative humidity (RH) and transport pathways of the air parcels from the source areas was studied in order to investigate the aerosol hygroscopicity and the influence of aerosol sources through transportation. The results revealed the following aerosol optical characteristics related to the relative humidity and the transport pathways from the source areas.

Temporal variations of both the humidity and the aerosol optical properties were observed at the altitude range of 1.0 to 2.2 km during the thirty minutes on April 17, 1994. The relationship between the aerosol parameters and the relative humidity indicated that the total volume backscattering cross section and the sphericity of the aerosol particles were larger in moist air than in dry that in this altitude region. The values of relative humidity in this region (13-38%RH) were near the phase transformation (crystallization or deliquescence) humidity of major tropospheric hygroscopic particles. At the altitude range of 2.2 to 3.5 km, high depolarization ratios with the RH values of ~35% that were as high as the maximum at 1.0-2.2 km were observed, suggesting that the two altitude regions had different aerosol constituent (hygroscopicity) or RH history.

Seasonal variations of the aerosol properties were found at the altitude range of 2-8 km for the period March 1994 to February 1997. The vertically integrated aerosol backscattering coefficient (IBC) showed an annual maximum with sharp rises in the spring (March–May) in the altitude range of 2-4 km and 4-8 km and the second maximum in the mid-late summer (July–August) in 2-4 km. The three months mean IBCs in the spring were as large as the annual mean by 1.6-2.2 times for 2-4 km and

1.6-1.8 times for 4-8 km.

Aerosol depolarization ratios as high as 25% were observed frequently in the 2-8 km region in the spring and occasionally in the 4-8 km regions in the autumn (September–November) and winter (December–February). In the 4-8 km regions these high values were found with RH values up to 80%, suggesting the presence of water-insoluble nonspherical particles (e.g., mineral dusts) in the regions. The air parcels in these regions had mostly carried over the Asian continent due to a westerly flow, suggesting that they were largely affected by the Asian continental source. Aerosol depolarization ratios less than 5% were predominant in the 2-8 km region in the summer (June–August) and in the 2-4 km region in the autumn over a wide range of RH values. In these regions high depolarization ratios (> 10%) were observed only with relatively low RH values (< 50%RH). These suggest the predominance of water-soluble particles (e.g., sulfuric acid solution droplets) and water-soluble deliquescent particles (e.g., sulfates and sea-salts) in these regions. The air parcels in these regions had been carried over the Pacific Ocean, suggesting that they were mainly affected by the maritime source. Depolarization ratios less than 5% with RH values less than 20% were predominantly observed in the 2-8 km region in the winter, suggesting the predominance of water-soluble particles in this region; the air parcels had mainly passed over the Asian Continent. These results suggest that transport pathways of the air parcels from source areas (the Asian continent and the Pacific Ocean) and the relative humidity significantly controlled the aerosol depolarization ratios.

Our results suggest that the transportation pathways of the air parcels from the source areas (the Asian continent and the Pacific Ocean) and the ambient relative humidity critically control the aerosol optical properties in the free troposphere over Nagoya.

Contents

1 Introduction

1.1 Free tropospheric aerosol in the Asian Pacific Rim Region and its roles

Aerosol particles in the free troposphere, which lies between about 2 and 10-16 km altitudes in midlatitudes, are frequently transported for more than thousands of kilometers and can affect remote areas. They may affect Earth's radiation balance directly by scattering and absorbing solar and terrestrial radiation (e.g., Toon and Pollack, 1976; Coakley et al., 1983) and indirectly by modifying the cloud properties thorough microphysical processes by acting as cloud condensation nuclei (Twomey, 1977a; Albrecht, 1989; Charlson et al., 1992) and by changing the concentrations of radiatively important gases such as water vapor (Twomey, 1991). They also play important roles in biogeochemical cycle of the Earth's material by providing media for various heterogeneous and multiphase reactions (Ravishankara, 1997) and by serving carriers for the chemical species (Prospero et al., 1983).

The long-range transport of mineral dust particles called Kosa (yellow sand) in Japanese, which originate from the arid and semi-arid land of the Asian Continent, to the North Pacific Ocean has been studied for over twenty years (Duce et al., 1980; Tsunogai and Kondo, 1982; Merrill et al., 1989). Duce (1991) estimated the mean atmospheric mass flux of mineral dust to the North Pacific Ocean to be 5.3 $g\,m^{-2}\,yr^{-1}$ and the total deposition to be 480 $Tg\,yr^{-1}$, which is about a half of the total deposition of dust matter to the world's ocean. The mineral dust particles contain some fraction of iron that is available for use by phytoplankton in surface water of the open ocean, which affects the sulfur cycle in both the ocean and the atmosphere through production of dimethyl sulfide (Zhuang et al., 1992). The particles finally deposit in the marine sediments that have been used for the study of paleoclimate (Rea, 1994).

The radiative effects of mineral aerosols remain highly uncertain because of the lack of detailed data for the optical properties as well as the scarcity of information about the vertical distribution and the spatial homogeneity of the aerosol layer (Parungo

et al., 1995). Nakajima et al. (1989) estimated the solar radiative heating of clear-sky atmosphere during the Asian dust storm event to be from 0.08 to 0.4 K day^{-1} assuming that the aerosol single scattering albedo ranges from 0.85 to 0.97 with the optical thickness of about 0.2 and the scale height of the aerosol layer is 3 km.

In addition to these natural mineral aerosols, there is concern over the influences of anthropogenic emissions from Asian industrial region on the tropospheric chemistry in the Pacific region (Prospero and Savoie, 1989; Hoell et al., 1997; Hatakeyama et al., 1997). Talbot et al. (1997) measured the concentrations of aerosol particulate matter, industrial solvent vapors (C_2Cl_4, CH_3CCl_3, and C_6H_6) and combustion-derived species (C_2H_2, C_2H_6, CO, and NO) over the western Pacific Ocean and found that the mixing ratios of all the species varied by a factor of ten depending on the transport pathways of the air parcels from the source regions of the Asian Continent. However, most of these studies about the influences of particles' sources in Asia on the remote free troposphere have been confined to the case studies and there are few statistical assessments of the source contributions on it.

The importance of chemical reactions of anthropogenic emissions with mineral aerosols in biogeochemical cycles has recently been evaluated by using a three-dimensional chemical/transport model (Zhang et al., 1994; Dentener et al., 1996; Xiao et al., 1997; Zhang and Carmichael, 1999). For instance, Zhang and Carmichael (1999) have shown that the presence of mineral dust could results in decrease in the concentrations of SO_2, NO^p_y ($NO_3 + N_2O_5 + HNO_3$), H_xO_y ($OH + HO_2 + H_2O_2$), and O_3 throughout heterogeneous surface reactions by 10%-53%, 16%-100%, 11%-59%, and 11%-40%, respectively, under typical dust storm conditions in East Asia. Although these model studies have revealed the potential roles of heterogeneous reactions on mineral aerosols, the results remain highly uncertain because few comparisons with the limited observational data have validated them. Since the chemical reactions on mineral aerosols can take place during the long-range transportation that mainly occurs in the free troposphere, it is necessary to measure the aerosol properties in the remote free troposphere to study the chemical effects of mineral aerosols.

Several aircraft observations have provided the information on the physical and chemical properties of the free tropospheric aerosol particles in the North Pacific region (Iwasaka et al., 1988; Yamato and Ono, 1989; Ikegami et al., 1993; Pueschel et al., 1994). The aerosol particles collected by the researchers were mineral dusts, sea salts, ammonium sulfates, sulfuric acid droplets, and their internal mixture, and the constituents varied depending on the season and height.

Relatively little information is available on the vertical distributions and the seasonal variations of the aerosol properties in the free troposphere over the North Pacific Rim region. Sasano (1996) measured the vertical profiles of aerosol extinction coefficient over Tsukuba in Japan in 1990-1993 using the Mie scattering lidar and found that the aerosol optical thickness in the troposphere indicated the maximum in the spring-summer period. Hayasaka et al. (1998) have shown that an accumulation particle mode around 0.1-0.2 μm in radius for volume size distribution was dominant in the summer, corresponding to heavily loaded in the planetary boundary layer, while large particle mode around several micrometers were abundant in the spring with high turbidity in the middle troposphere, on the basis of simultaneous measurements with lidar, a sunphotometer, and an aureolemeter in Tsukuba from 1991 to 1992.

1.2 Raman lidar measurement: necessity for measuring aerosol properties with humidity in their natural state

Raman lidar has been developed to remotely measure the vertical profiles of humidity and aerosol optical properties simultaneously (Melfi, 1972; Whiteman et al. 1992; Ansmann et al., 1992a,b; Shibata et al., 1996a,b). Application of this lidar technique to the atmospheric studies has been accumulating in recent years. The vertical structures of fronts (Melfi et al., 1989), gravity currents (Koch et al., 1991), and marine boundary layer (Cooper et al., 1995) have been revealed by measuring the vertical and temporal distributions of the water vapor mixing ratio and the aerosol backscattering. Shibata et al. (1996a) and Reichardt et al. (1996) demonstrated the device's applicability

for the detection of ice clouds by simultaneously measuring the humidity and aerosol vertical profiles. Ferrare et al. (1998) derived the aerosol hygroscopic factor, real refractive index, and single scattering albedo from the aerosol backscattering and extinction coefficients measured with the ground-based Raman lidar in conjunction with the aerosol size distribution measured with the optical particle counter on board an aircraft.

Since the aerosol properties such as size, shape, phase, and chemical composition critically depend on the ambient relative humidity (Orr et al., 1958; Hänel, 1976; Tang, 1996), it is important to measure aerosol properties with the relative humidity in their natural state. Although this importance has been well recognized, few observational data is available for the shape and phase of the aerosols in their natural state in the free troposphere because of the technical difficulties and analytic limitations. In situ measurement techniques on board an aircraft or a balloon can provide detailed information of the aerosol properties, i.e., aerosol size distribution, morphology, and chemical composition, but they often subject the aerosols to change in relative humidity during the sampling process (Porter et al., 1992; Baumgardner and Huebert, 1993). One of the advantage of the Raman lidar technique is that it can measure the aerosol properties with the humidity without changing the humidity and without disturbing the particles by collection during which possible changes such as evaporation of volatile components, agglomeration, and selective losses are expected.

In addition to the aerosol backscattering and extinction coefficients obtainable with the lidar, depolarization ratio is a useful parameter to study aerosol microphysics because deviations from zero can indicate particle nonsphericity (e.g., Bohren and Huffman, 1983). The particle shape critically controls the particle's optical property (e.g., Koepke and Hess, 1988) and hence affects the Earth's radiative process (Lacis and Mischenko, 1995; Pilinis and Li, 1998) as well as the vertical distribution of the particles (Liao and Seinfeld, 1998). For example, Pilinis and Li (1998) reported that direct aerosol forcing may be underestimated by a factor of 3 if particle nonsphericity is neglected when the solar zenith angle is close to zero, based on the field measurement

and the model calculation assuming that the particles are mass-equivalent prolate spheroids. Also, properly accounting for the particle nonsphericity is necessary for retrievals of satellite reflectance and Mie backscattering lidar signals (Mischenko et al., 1995; 1997).

Since the depolarization ratio is a measure of particles' nonsphericity, it can also be considered as an indication of the particle phase; liquid droplet particles are mostly spherical and indicate near-zero or low depolarization values, whereas solid crystals are generally nonspherical and indicate values substantially larger than zero. The particle phase is the key variable that determines the rates of chemical reaction with gaseous species (Ravishankara, 1997); reaction on solid are almost confined to the surface so that the rates are surface area limited (heterogeneous reactions), whereas those in liquid droplets take place after the molecules has been incorporated into the bulk of liquid so that the rates are both volume and surface area limited (multiphase reactions). For example, Msibi et al. (1994) has shown that the reaction probability for liquid NaCl particle with gaseous N_2O_5 is about 15 times higher than that for solid based on the laboratory experiment.

The hygroscopicity of aerosol particles can be estimated from the relationship between the aerosol depolarization ratio and the relative humidity that are simultaneously obtainable with the Raman lidar, since hygroscopic particles (contain water-soluble compound) can change shape (phase) and the depolarization ratio depending on the relative humidity, whereas nonhygroscopic particles (consist of water-insoluble compound) are not likely to change them according to the humidity. The particle hygroscopicity significantly affects the magnitude of the direct radiative forcing effect (Boucher and Anderson, 1995). Also, it determines whether the particle can effectively serve as a cloud condensation nuclei (Twomey, 1977b). However, there are few observational data on the hygroscopic characteristics of the aerosol particles in the free troposphere.

Besides the use of the depolarization and the relative humidity for the estimate of particle hygroscopicity, it may be important to measure the aerosol properties with the

relative humidity since the chemical reaction rates of gas with aerosol particles depend on the relative humidity as well as the particle phase as mentioned above. A laboratory experiment has shown that reaction probability of gaseous N_2O_5 with NH_4HSO_4 particle increases with increasing relative humidity even below the deliquescence point (Mozurkewich and Calvert, 1988). Haury et al. (1978) and Dlugi et al. (1981) reported that the rate of SO_2 oxidation increases with increasing relative humidity on fly ash which consist mainly of the oxides of silicon, aluminum, iron, and calcium and may serve as a surrogate for mineral dust. From these facts, it is important to measure the aerosol properties with the relative humidity in their natural state to study the effects of the atmospheric aerosols on the Earth's atmospheric system.

1.3 Objectives

The purpose of this study is to investigate the seasonal and altitude characteristics of the aerosol optical properties including the backscattering, extinction, and depolarization ratio in the free troposphere over Nagoya (35.1°N, 137.0°E) in Japan located in the Asian Pacific Rim region by using the Raman lidar. We analyzed the relation of these aerosol properties to the relative humidity that was simultaneously obtained with the Raman lidar and the transport pathways from the source areas. This paper contains five sections. The introduction is followed by a description of the Raman lidar system used in this study (Section 2). Section 3 describes the data analyzing procedure to derive the humidity and aerosol optical properties from the lidar signals. The validity of the derived data is discussed by comparing the humidity with the radiosonde soundings and by comparing the aerosol extinction-to-backscatter ratio with the other theoretical and observational results. Section 4 presents the results of the observations carried out for the period March 1994 to February 1997. We focus on the observed aerosol optical properties in relation to the relative humidity and transport pathways of the air parcels from the source areas. A summary of this study is given in Section 5.

2 System description of the Raman lidar

2.1 Location

The Raman lidar is installed at the Higashiyama campus of Nagoya University (35.1°N, 137.0°E, 75 m above sea level). The measurement site is located in the urban area located 20 km inland from the Ise Bay and 70 km from the Pacific Ocean (Fig. 2.1).

2.2 Instrumentation

The Raman lidar is designed to simultaneously measure the vertical profiles of Raman scattering by oxygen, nitrogen, and water vapor, as well as Rayleigh and Mie scattering in the atmosphere. Figure 2.2 shows the photograph of the lidar system. A schematic diagram and the specification of the system are shown in Fig. 2.3 and Table 2.1, respectively.

The transmitter consists of Nd:YAG laser that simultaneously emits laser pulses in three wavelengths (354.7, 532 and 1064 nm) that are linearly polarized. The repetition rate of the laser pulses is 10 Hz and each pulse lasted 5-8 ns. The average energies of the pulses are 200, 50, and 430 mJ for 354.7, 532, and 1064 nm, respectively. The laser beams are vertically transmitted into the atmosphere by reflecting with mirrors after expanding its diameter to 36 mm and collimating the divergence to 0.2 mrad using collimators. The light backscattered from the atmospheric gases and aerosol particles is collected with Cassegrain telescope with 1-m diameter. The output of the telescope is fed through a field-limiting stop (the aperture is normally adjusted to 1.5 mrad) and then divided into five detector channels by several beam splitters. The five detector channels detect the Raman scattering and Mie/Rayleigh scattering using interference filters, dichroic mirrors, and polarizers (Table 2.2). The detection species and the wavelengths for the normal tropospheric measurements are as follows:

Ch1: Raman water vapor scattering (407.5 nm) excited by 354.7 nm

Ch2: Raman oxygen (or nitrogen) scattering (375.4 nm (or 386.7 nm)) excited by 354.7 nm

Ch3: Parallel component of Mie/Rayleigh scattering at 532 nm with respect to the polarization plane of the emitted laser

Ch4: Perpendicular component of Mie/Rayleigh scattering at 532 nm with respect to the polarization plane of the emitted laser

Ch5: Mie/Rayleigh scattering at 1064 nm

For the Raman channels (Ch1 and Ch2), high rejection of the Mie/Rayleigh scattering component is necessary since the Raman backscattering cross section is smaller than that of Rayleigh and Mie scattering by about three order of magnitude. To reject the Mie/Rayleigh component for the Raman channels, we used the dichroic mirror and the interference filter whose total transmission of the Mie/Rayleigh component is $< 10^{-9}$.

The detectors used in this study are Hamamatsu R331 photomultiplier tubes (PMTs) for the Chs 1-4 and R1767 (or R3236) for the Ch5. The PMTs are cooled to about -30°C and operated in the photon counting mode. The output pulses of the PMTs are filtered by the discriminators and then registered with the photon counter. The photon counter begins to take data when the laser fires by monitoring with a photodiode. The data are recorded with a time-bin width of 2/3 μs (0.2 μs after April 1996) and total 1024 (4096 after April 1996) bins are acquired for a profile. The data are finally stored on a hard disk of a personal computer. The data are normally accumulated for every five minutes in the tropospheric measurements. Thus we obtain the profiles at five spectral channels as a function of height with vertical resolution of 50 m (30 m after April 1996) every five minutes.

Before the calculation of the physical parameters from the raw data, the background noise was subtracted from the data. The background noise was obtained by

taking average of the signals from the altitude above 100 km, from which the backscattered radiation by scattering materials is negligible. Measurement uncertainty was estimated from 1σ confidence of the photon counts assuming the Poisson statistics.

2.3 Observation period

The observations have been conducted on a regular basis since 1994. The operations were normally carried out in the nighttime under almost visible-cloud free conditions. The data were usually taken for 30-60 minutes for the tropospheric range (0.5-15 km) and for 60-120 minutes for the stratospheric range (10-35 km). Total 332 profiles were obtained during the period March 1994 to February 1997.

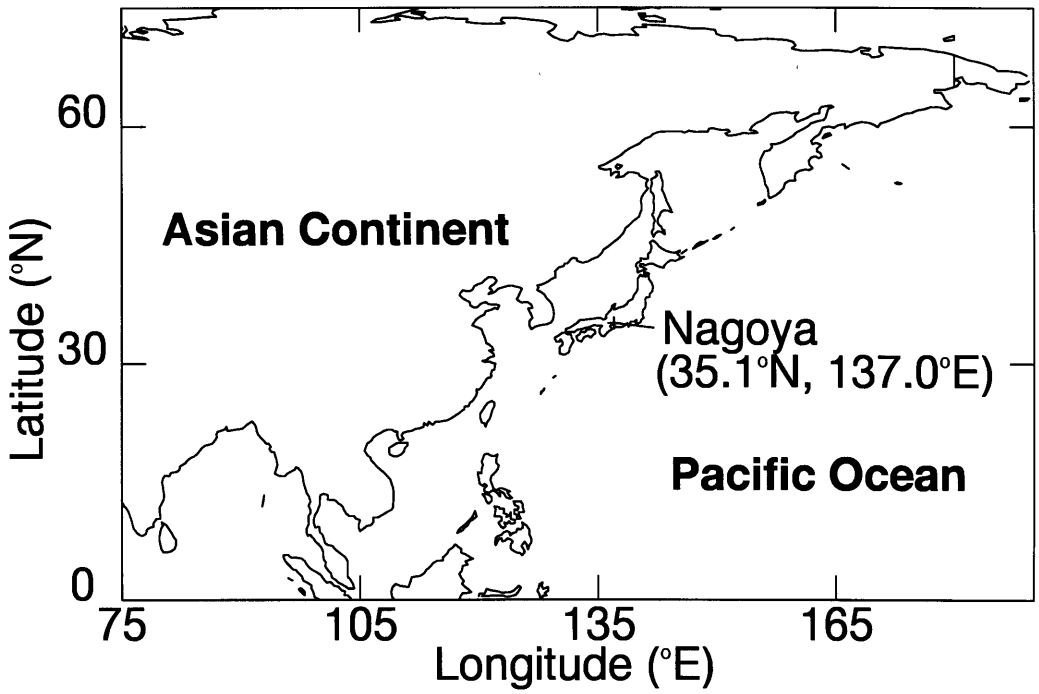

Fig. 2.1 Location of the measurement site.

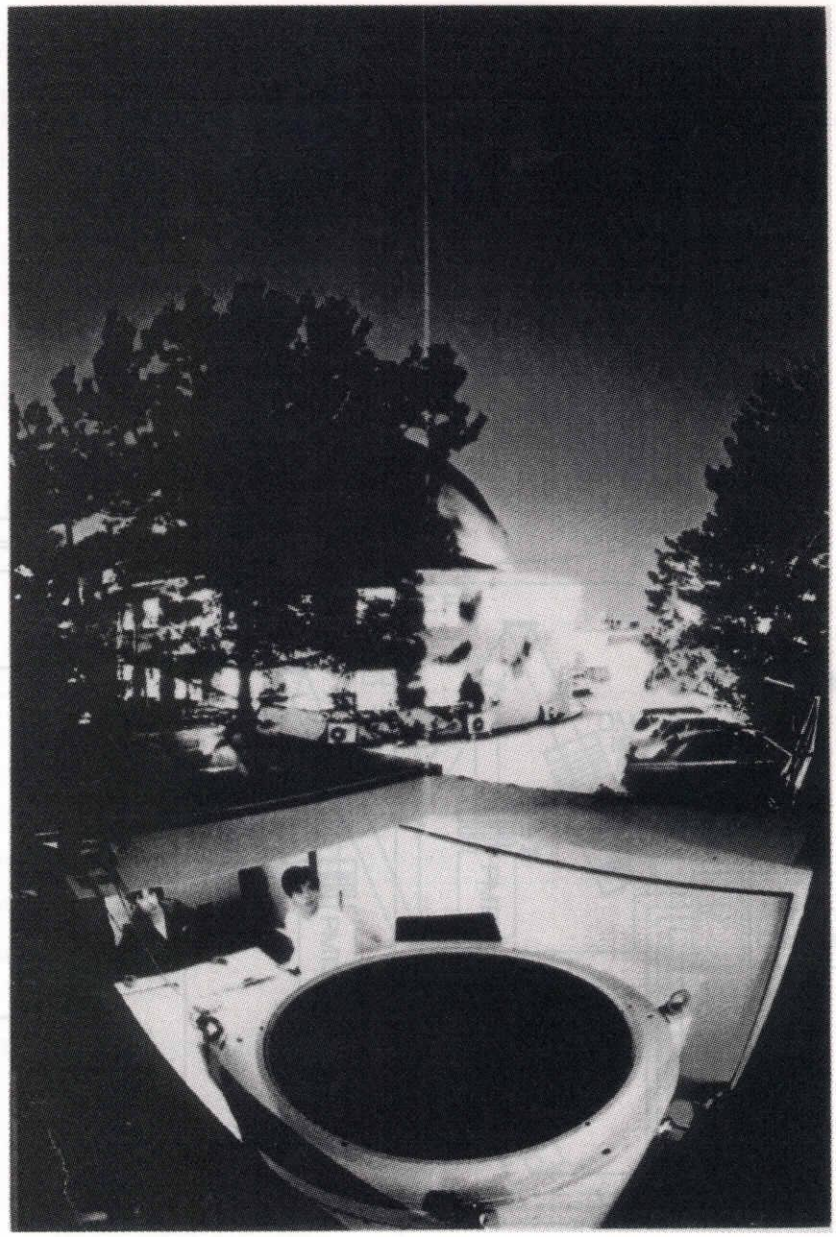

Figure 2.2 Photograph of the Raman lidar at STEL of Nagoya University.

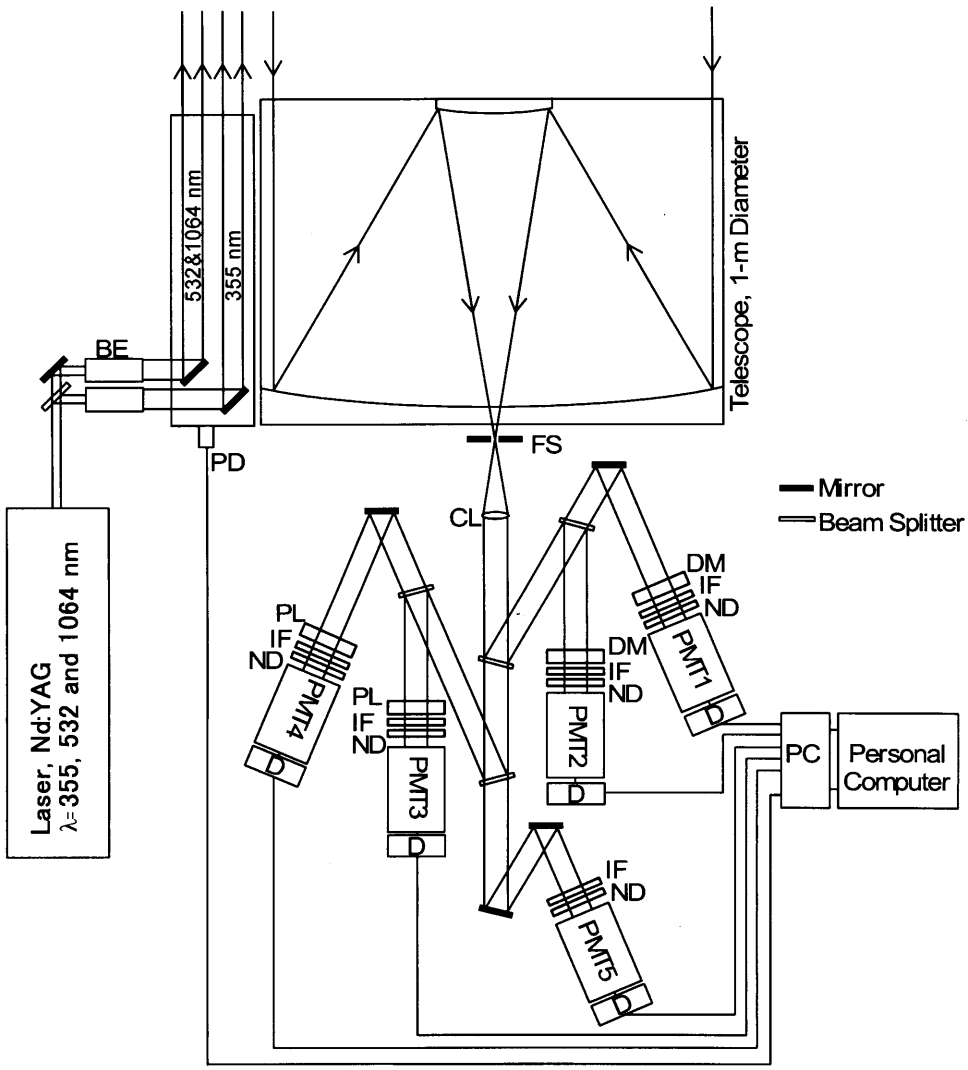

Fig. 2.3 Schematic diagram of the Raman lidar (BE: Beam expander, PD: Photodiode, FS: Field stop, CL: Collimating lens, DM: Dichroic mirror, PL: Polarizer, IF: Interference filter, ND: Neutral-density filter, PMT: Photomultiplier tube, D: Discriminator, and PC: Photon counter).

Table 2.1 Specifications of the Raman lidar at Nagoya University

Transmitter:	
Laser type	Nd:YAG
Wavelength (nm)	354.7 532 1064
Energy/pulse (mJ)	200 50 430
Repetition rate (Hz)	10
Beam divergence (mrad)	0.2 (after collimator)
Receiver:	
Telescope type	Cassegrain
Diameter (m)	1.0, $f/4$
Field of view (mrad)	0.2-5.0
Detector	PMT
Signal detection	Photon counting
Range resolution (m)	50 (30 after April 1996)
Channel number	5

Table 2.2 Characteristics of the detector channels

Channel number		1	2	3	4	5
Detection species		Raman water vapor	Raman oxygen*	Mie/ Rayleigh	Mie/ Rayleigh	Mie/ Rayleigh
Interference filter	Center wavelength (nm)	407.5	375.4	532	532	1064
	FWHM (nm)	0.78	1.00	1.17	1.17	1.10
	Transmission outside pass band	10^{-5}	10^{-5}	10^{-5}	10^{-5}	10^{-5}
Mie/Rayleigh Cut filter	Transmission at 355 nm	$<10^{-4}$	$<10^{-4}$	-	-	-
Polarizer		-	-	//	$\perp$	-
PMT	(HAMAMATSU)	R331	R331	R331	R331	R1767 (orR3236)

*Raman nitrogen scattering (386.7 nm) is detected for the stratospheric measurements

3 Data analyzing procedure for the Raman lidar signals

The single-backscatter signals measured with the Raman lidar can be expressed as

$$P_\lambda(z) = K\frac{O(z)}{z^2}\beta_\lambda(z)T_{\lambda_L}(z_0,z)T_\lambda(z_0,z), \tag{3-1}$$

where $P_\lambda(z)$ is the backscatter signal at the wavelength λ returned from the altitude $z\,(=\frac{ct}{2}$, where c is the speed of light and t is the elapsed time after laser emission), K is a constant that accounts for the detection efficiency of the channel, $O(z)$ is the beam overlap factor, $\beta_\lambda(z)$ is the volume backscattering coefficient of the scattering material at λ, $T_\lambda(z_0,z)$ is the atmospheric transmission at λ between the lidar at altitude z_0 and z that is given by $T_\lambda(z_0,z)=e^{-\int_{z_0}^{z}[\sigma_{m,\lambda}(z')+\sigma_{a,\lambda}(z')]dz'}$ where $\sigma_{m,\lambda}(z)$ and $\sigma_{a,\lambda}(z)$ are the volume extinction coefficients of air molecules and aerosol particles, respectively, and λ_L is the laser wavelength.

The following subsection describes the data analyzing procedure to calculate the humidity, aerosol extinction and backscattering coefficients, and the depolarization ratio from the Raman lidar signals. Section 3.1 describes the methods for calculating the water vapor mixing ratio and the relative humidity. The results of the comparisons with the coincident radiosonde measurements are also presented. Section 3.2 describes the methods for calculating the aerosol extinction coefficient, backscattering ratio, backscattering coefficient, and the depolarization ratio. The potential for discriminating the mineral dust particles from the ice crystals by the extinction-to-backscatter ratio is also discussed by comparing the observed data with the reported results.

3.1 Water vapor mixing ratio and relative humidity

3.1.1 Water vapor mixing ratio

Water vapor measurements through the Raman scattering technique commenced in the late 1960s (Melfi, 1969; Cooney, 1970) and have been improved by taking averages of technical advantages, particularly those in the laser system over the past ten years (Melfi and Whiteman, 1985; Vaughan et al., 1988; Whiteman et al., 1992; Shibata et al., 1996). The Raman backscatter signals for water vapor and oxygen molecule are respectively expressed as

$$P_{H_2O}(z)=K_{H_2O}\frac{O_{H_2O}(z)d\sigma_{H_2O}(\pi)}{z^2}\frac{}{d\Omega}n_{H_2O}(z)e^{-\int_{z_0}^{z}[\sigma_{m,\lambda_L}(z')+\sigma_{a,\lambda_L}(z')]dz'}e^{-\int_{z_0}^{z}[\sigma_{m,\lambda_H}(z')+\sigma_{a,\lambda_H}(z')]dz'}, \tag{3-2}$$

$$P_{O_2}(z)=K_{O_2}\frac{O_{O_2}(z)d\sigma_{O_2}(\pi)}{z^2}\frac{}{d\Omega}n_{O_2}(z)e^{-\int_{z_0}^{z}[\sigma_{m,\lambda_L}(z')+\sigma_{a,\lambda_L}(z')]dz'}e^{-\int_{z_0}^{z}[\sigma_{m,\lambda_O}(z')+\sigma_{a,\lambda_O}(z')]dz'}, \tag{3-3}$$

where $P_X(z)$ is the Raman backscatter signal of X molecules returned from the altitude z, K_X is a coefficient that accounts for the detection efficiency of the channel, $O_X(z)$ is a beam overlap factor, $\frac{d\sigma_X(\pi)}{d\Omega}$ is the differential Raman backscattering cross section of X molecules [m^2sr^{-1}], $n_X(z)$ is the number density of X molecules [m^{-3}], λ_L (=354.7 nm) is the laser wavelength, λ_O (=375.4 nm) and λ_H (=407.5 nm) are the detection wavelengths of the Raman backscattering of oxygen and water vapor, respectively.

Since oxygen is a constant fraction of dry air (21% by volume) at the heights over which the measurements are made, the Raman oxygen signal can be considered as a measure of the number density of dry air. Thus by taking the ratio of the two signals, the water vapor mass mixing ratio (w) is given by

$$w(z) \equiv \frac{M_v}{M_d} \frac{n_{H_2O}(z)}{n_d(z)} = K \cdot r_{ld}(z),$$

where

$$r_{ld}(z) = \frac{P_{H_2O}(z)}{P_{O_2}(z)} e^{\int_{z_0}^{z} [\sigma_{m,\lambda_H}(z') - \sigma_{m,\lambda_O}(z')]dz} e^{\int_{z_0}^{z} [\sigma_{a,\lambda_H}(z') - \sigma_{a,\lambda_O}(z')]dz}, \qquad (3\text{-}4)$$

where M_v(=18.0153) and M_d(=28.9645) are the molecular weight of water vapor and dry air, respectively, $n_{H_2O}(z)$ and $n_d(z)$ are the number density of water vapor and dry air at z, and K is the system calibration coefficient. It should be noted in Eq. (3-4) we assumed the ratio of the backscattering cross sections ($d\sigma_{H_2O}(\pi)/d\Omega / d\sigma_{O_2}(\pi)/d\Omega$) and that of the beam overlap factors (O_{H_2O} / O_{O_2}) between the two channels were constant independently of height. These assumptions are further discussed in later (Section 3.1.4).

In the previous studies of humidity measurements using Raman lidar technique (e.g., Vaughan et al., 1988; Whiteman et al., 1992), Raman nitrogen scattering was generally used to measure the relative atmospheric density. The reason for this was nitrogen is the largest constituent of air so that strong Raman backscatter signal can be obtained. However, we used the Raman oxygen scattering in place of the Raman nitrogen scattering for the tropospheric measurements because signal saturation problem could arise for our system in detecting the Raman nitrogen signals returned from the lower troposphere.

Correction of atmospheric transmission

Correction must be applied to account for the differential atmospheric transmission between the two Raman wavelengths (exponential terms in Eq. (3-4)). The atmospheric transmission is separately calculated for air molecules and aerosol particles by vertically integrating the extinction coefficients.

The volume extinction coefficient for air molecule σ_m at the wavelength λ is given by (Bucholtz, 1995)

$$\sigma_{m,\lambda}(z) = \frac{24\pi^3 (n_s^2 - 1)^2 n_d(z)}{\lambda^4 N_s^2 (n_s^2 + 2)^2} \left(\frac{6 + 3\rho_n^t}{6 - 7\rho_n^t} \right) [\mathrm{m}^{-1}], \tag{3-5}$$

where λ is the wavelength [m], n_s is the refractive index of standard air at λ, N_s is the molecular number density for standard air (=2.54743×10^{25} m^{-3}), $n_d(z)$ is the number density of the air [m^{-3}] at z, and ρ_n^t is the depolarization factor of the air at λ. The values of n_s and ρ_n^t are obtained from the tables of Bucholtz (1995). We calculated the extinction coefficient for air molecule ($\sigma_{m,\lambda}(z)$) using the atmospheric density data obtained with the coincident radiosonde taken on the same night of the measurements. If the radiosonde data were not available, we used the global objective analysis data supplied with the Japan Meteorological Agency (GANAL (or GAPLX after March 1996)).

The volume extinction coefficients for aerosol particles ($\sigma_{a,\lambda}(z)$) can be calculated from the Raman oxygen signals or Mie/Rayleigh signals that is described in Section 3.2. By using the relation $\sigma_{a,\lambda}(z) \propto \lambda^{-k(z)}$ we calculated the differential aerosol transmission between the Raman wavelengths of water vapor λ_H and oxygen λ_O.

For example, the amount of the total differential atmospheric transmissions between altitudes of 0 and 5 km are about 0.94, 0.92, and 0.88 for the aerosol optical thickness of 0 (no aerosols), 0.3 (normal), 1.0 (quite hazy), respectively at λ =354.7 nm.

Temperature dependence of the Raman backscattering cross section

In Eq. (3-4), we assumed that the ratio of the Raman backscattering cross sections are constant. However, the effective Raman backscattering cross sections can vary with temperature depending on the bandwidth of the interference filter. Thus we assessed the temperature variation of the effective Raman backscattering cross sections of oxygen and water vapor for our system.

(Raman oxygen channel)

The Raman oxygen channel detects the 1-st Stokes component of the vibrational-rotational transitions of Raman oxygen scattering excited by the radiation at 354.7 nm. The Raman oxygen lines consist of a strong Q-branch ($\Delta v = +1, \Delta J = 0$) centered at approximately 375.4 nm and O- and S-branches ($\Delta v = +1, \Delta J = -2$ and $\Delta v = +1, \Delta J = +2$, respectively) that distribute both shorter and longer wavelengths of the Q-branch. The total differential backscattering cross section of the Q-branch is independent of temperature for our interest. However, the individual differential backscattering cross sections of the O- and S-branches varies with temperature. Since the interference filter for the Raman oxygen channel used in this study (FWHM=1.00 nm centered at 375.4 nm) passes the full Q-branch and small fraction of O- and S-branches, the effective Raman backscattering cross section of oxygen for our system slightly varies with temperature.

The differential Raman backscattering cross sections can be calculated using Placzek polarizability theory (Kobayashi and Inaba, 1972) that is described in Appendix A. The calculated Raman spectrum of oxygen excited by 354.7 nm radiation at 200 K and 300 K is shown in Fig.3.1. The absolute values of the differential backscattering cross sections are calculated from the data listed in Inaba (1976) assuming $d\sigma / d\Omega \propto \lambda^{-4}$. It is found the pass-band of the interference filter used in this study covers the whole Q-branches and several lines of S- and O-branches. The intensity distributions of the S- and O-branches vary depending on the temperature according to the Boltzmann distribution.

Figure 3.2 shows the temperature variation of the effective differential backscattering cross section for the Raman oxygen channel used in this study. The effective cross section decreases with increasing temperature due to decreasing the intensities of O- and S-branches inside the pass-band (Fig. 3.1). The relative difference of the effective backscattering cross section is less than 3% between 230 K and 300 K range of our interest ($z \leq 10$ km).

(Raman water vapor channel)

The Raman spectrum of water vapor is rather complicated because its molecular structure is asymmetric top. The spectrum of the $\nu = 0 \rightarrow \nu = 1$ vibrational transitions excited by 354.7 nm radiation consists of strong Q-branch centered at 407.5 nm which spans approximately 0.3 nm (Bribes et al., 1976). The total intensity of the Q-branch is independent of temperature for our interest. We used the interference filter whose bandwidth was 0.78 nm (FWHM) centered at 407.5 nm so that the contribution of the temperature dependent rotational lines to the effective backscattering cross section is estimated to be less than 1% (Vaughan et al., 1988).

Accordingly, the temperature variation of the ratio of the effective Raman backscattering cross section between the Raman water vapor and oxygen channels for our system is estimated to be less than 2%. Therefore, we did not take account of this temperature dependence of the ratio in this study.

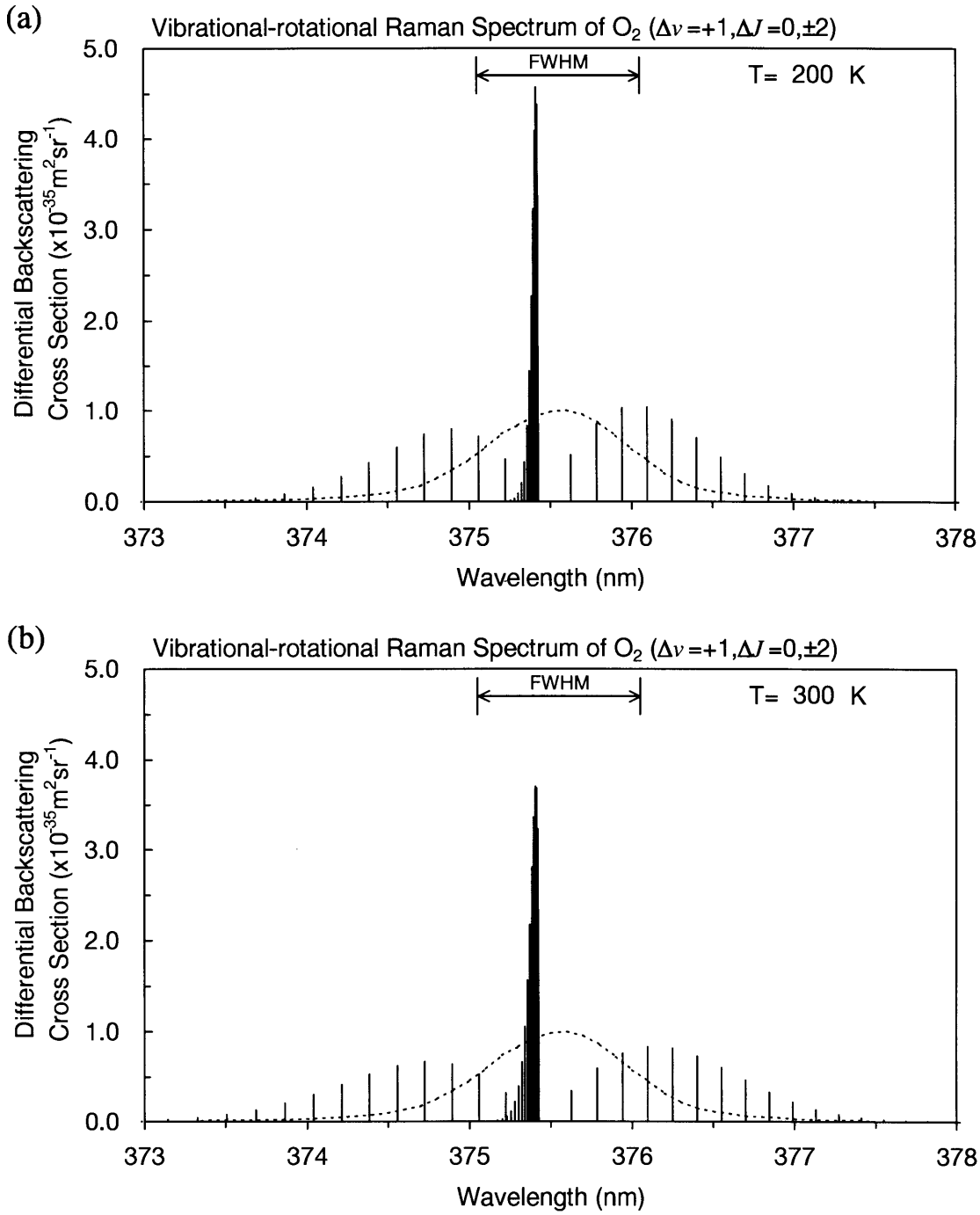

Fig. 3.1 Calculated 1-st Stokes vibrational-rotational Raman spectrum of oxygen molecule excited by 354.7 nm radiation (solid lines) at (a) 200 K and (b) 300 K. The dotted line shows the transmission curve of the interference filter used in this study (arbitrary unit) and the horizontal bar shows the full width at half maximum (FWHM=1.00 nm).

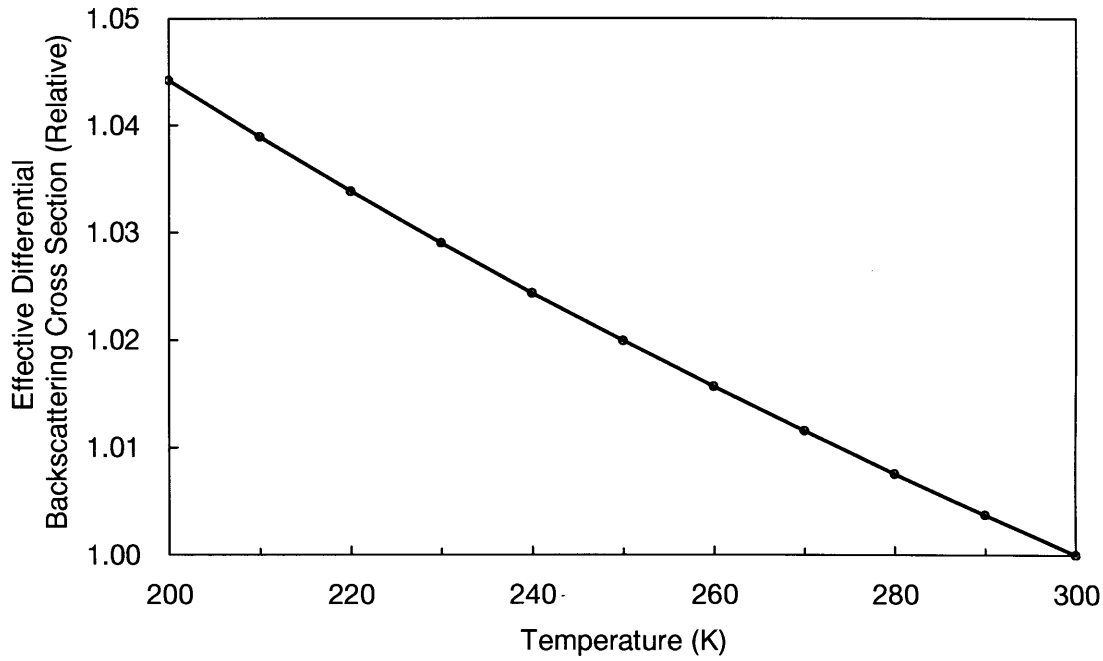

Fig. 3.2 Temperature dependence of the effective Raman backscattering cross section for the Raman oxygen channel used in this study.

Measurement uncertainty in the water vapor mixing ratio

The measurement uncertainty in the water vapor mixing ratio is estimated by 1σ confidence of the photon count assuming the Poisson's statistics:

$$\delta w(z) = w(z)\left[\left(\frac{\delta K}{K}\right) + \left(\frac{\delta P_{H_2O}(z)}{P_{H_2O}(z)}\right)^2 + \left(\frac{\delta P_{O_2}(z)}{P_{O_2}(z)}\right)^2 + \delta T_m(z_L, z) + \delta T_a(z_L, z)\right]^{\frac{1}{2}}, \quad (3\text{-}6)$$

where

$$\delta P_x(z) = \sqrt{P_{x,signal}(z) + 2P_{x,noise}},$$

$$\delta T_m{}^2(z_0, z) = \left\{\left[\left(\frac{\lambda_H}{\lambda_O}\right)^{-4} - 1\right]\frac{d\sigma_{m,\lambda_O}}{d\Omega}\Delta z\right\}^2 \sum_{z'=z_0}^{z}\left(\frac{\delta n_d(z')}{n_d(z')}\right)^2,$$

and

$$\delta T_a{}^2(z_0, z) = \Delta z^2 \sum_{z'=z_0}^{z}\left(\left\{\left[\left(\frac{\lambda_H}{\lambda_L}\right)^{-k(z')} - \left(\frac{\lambda_O}{\lambda_L}\right)^{-k(z')}\right]\delta\sigma_{a,\lambda_L}(z')\right\}^2 + \left\{\left[-\left(\frac{\lambda_H}{\lambda_L}\right)^{-k(z')} ln\left(\frac{\lambda_O}{\lambda_L}\right) + \left(\frac{\lambda_H}{\lambda_L}\right)^{-k(z')} ln\left(\frac{\lambda_O}{\lambda_L}\right)\right]\sigma_{a,\lambda_L}(z')\delta k(z')\right\}^2\right).$$

Here, $P_{X,signal}$ and $P_{X,noise}$ are the signal and the background noise of the photon count, respectively, and k is the wavelength exponent of the aerosol extinction coefficient. The uncertainties δk and $\delta\sigma_{a,\lambda_L}$ are given and discussed in Section 3.2.5. We assumed the relative uncertainty in the atmospheric density was 1% when the GANAL (or GAPLX) data was used.

3.1.2 Relative humidity

Relative humidity with respect to water or ice (RH_x) is calculated from the water vapor mixing ratio w and the atmospheric pressure P and temperature T by

$$RH_x(z) = \frac{e(z)}{e_{s,x}'(T,P)} \times 100 = \frac{w(z)P(z)}{(M_v / M_d + w)e_{s,x}'} \times 100 \ [\%], \quad (3\text{-}7)$$

where $e_{s,x}'$ is the equilibrium water vapor pressure of moist air. The value of $e_{s,x}'$ is calculated by (Buck, 1981)

$$e_{s,x}'(T,P)=e_{s,x}(T)f(T,P), \tag{3-8}$$

where $e_{s,x}$ is the equilibrium vapor pressure of pure water vapor and f is the enhanced factor for moist air that accounts for dissolution of dry air into water, interaction between dry air and water vapor molecules, and the compressibility. The value of $e_{s,x}$ is given by

$$e_{s,x}(T)=a\,exp\left[\frac{(b-(T-T_0)/d)(T-T_0)}{(T-T_0)+c}\right], \tag{3-9}$$

and the enhanced factor f is given by

$$f(T,P)=1+A+P[B+C(T-T_0)], \tag{3-10}$$

where P is the atmospheric pressure [hPa], T is the atmospheric temperature [K], $T_0=273.15$ K and the coefficients $a-c$ and $A-C$ are given as follows: $a=6.1121$, $b=18.729$, $c=257.87$ $d=227.3$, $A=7.2\times10^{-4}$, $B=3.20\times10^{-6}$ and $C=5.9\times10^{-10}$ for water and $a=6.1115$, $b=23.036$, $c=279.82$, $d=333.7$, $A=2.2\times10^{-4}$, $B=3.83\times10^{-6}$, and $C=6.4\times10^{-10}$ for ice.

We calculated the RH from the w measured with the lidar by combining with the P and T measured with a coincident radiosonde or GANAL (or GAPLX).

Measurement uncertainty in the relative humidity

The measurement uncertainty in RH is calculated using the Clapeyron-Clausius equation and is given by

$$\delta(RH)=\left\{(RH)^2\left[\left(\frac{\delta w}{w}\right)^2+\left(\frac{\delta P}{P}\right)^2+\left(\frac{L_x}{R_v}\frac{\delta T}{T^2}\right)^2\right]+(\delta T)^2\left[wP\frac{M_d}{M_v}\frac{1}{6.11}e^{-\frac{L_x}{R_vT_0}}\frac{L_x}{R_vT^2}\right]^2\right\}^{\frac{1}{2}}, \tag{3-11}$$

where L_x is the latent heat of appropriate phase (=2.501×10^6 J kg^{-1} for water and =2.838×10^6 J kg^{-1} for ice), $R_v = R/M_v$ is the gas constant for water vapor. We assumed $\delta P/P = 0.01$ and $\delta T = 1\text{K}$ when we used GANAL (or GAPLX) data.

3.1.3 Determination of the calibration coefficient

The calibration coefficient K in Eq. (3-4) can be obtained by fitting the lidar data to the humidity data measured with the coincident radiosonde. We had carried out nine coincident measurements during the period May 1994 to May 1998. The radiosonde was Väisala RS80-15, which equips humidity sensor of thin-film capacitive element (HUMICAP). The accuracy of this sensor is reported to be 2%RH at 0 - 100% RH range (Larsen et al., 1993)

The calibration coefficient was calculated by taking the weighted mean of the ratio of the water vapor mixing ratio obtained with the radiosonde $w_{sd}(z)$ to the value of the signal ratio of the Raman water vapor to oxygen backscatter $r_{ld}(z)$ in Eq. (3-4) obtained with the lidar that is given by

$$K=\frac{\sum_{z=z_1}^{z_2} w_{sd}(z)r_{ld}(z)}{\sum_{z=z_1}^{z_2} r_{ld}(z)^2}. \tag{3-12}$$

Before the calculation of the coefficient, the vertical resolutions of the two data were adjusted to 350 m (330 m after April 1996) by taking running mean. We calculated the value of K by using the data between 1 and 8 km because the uncertainties in the lidar data generally exceeded 20% above this altitude range. The number of the data between 1 and 8 km was 141 (234 after April 1996).

3.1.4 Comparisons of the humidity profiles between Raman lidar and Radiosonde

Coincident measurements were made on the nights of May 20, September 10-11, November 28 and 30 in 1994, June 5, and September 14 in 1996, September 27 in 1997, and February 13 and May 19 in 1998. The radiosondes were launched about 30 m (from May 20 to November 30, 1994) or 200 m (from June 5, 1996 to May 19, 1998) away from the lidar. The radiosonde normally ascended at about 5.5 m s^{-1} and reached the height of 10 km about 30 minutes after the launch. The Raman lidar were continuously operated before and after the launch.

Figures 3.3-3.5 show the vertical profiles of the water vapor mixing ratio and the relative humidity obtained with the Raman lidar and radiosonde on May 20, 1994, September 10-11, 1994, and June 5, 1996, respectively. The vertical resolutions were 350 m in Figs. 3.3 and 3.4, and 330 m in Fig. 3.5. The humidity profiles measured with the lidar and radiosonde showed agreement in the troposphere as low as 0.5 km. This suggests the beam overlap factors of the water vapor and Raman oxygen channels were almost the same and canceled by taking the ratio of the two signals (Eq. 3-4). The relative uncertainty in the water vapor mixing ratio measured with the lidar was about 5% at 2 km and increased with height to 20% at 8 km.

The profiles obtained with the two instruments on September 10-11 (Fig. 3.4) showed slight discrepancies in their vertical distributions: the heights where steep vertical gradient of the humidity were found in the lidar profile (3.6, 8.0 and 10 km) were slightly shifted from those found in the radiosonde profile. One possible reason for

this was that the two instruments did not observe the same air parcels because the measurement period of the two instruments differed by about 2 hours. Moreover, the lidar data indicated the mean values of the air that passed over the lidar site for thirty minutes, whereas the radiosonde measured the spontaneous humidity of the surrounding air while ascending and drifting horizontally with the wind. Thus, discrepancies between the two data could arise due to horizontal inhomogeneity of the humidity distribution and horizontal displacement of the radiosonde during the ascent.

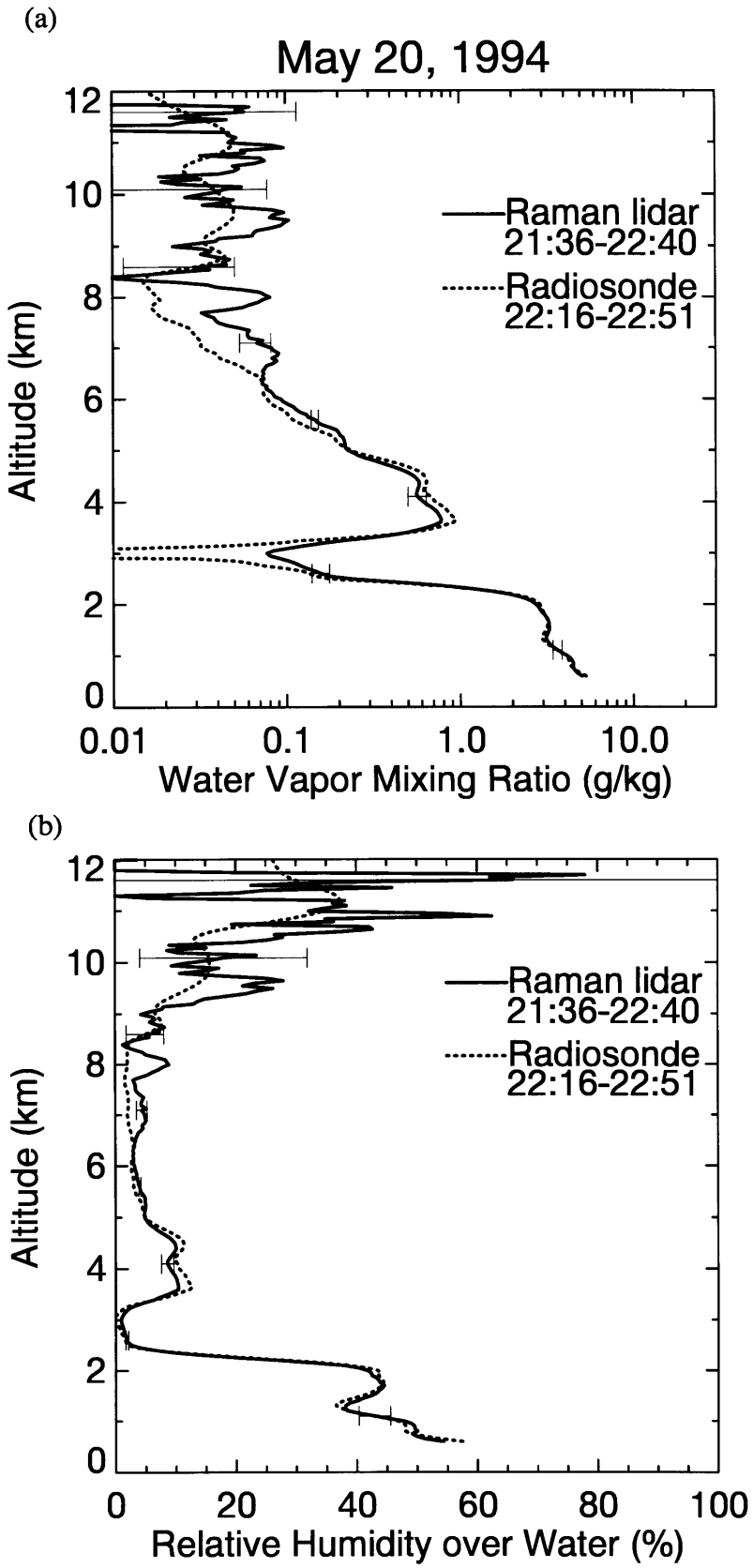

Figure 3.3 Comparison between Raman lidar (solid) and Vaisala radiosonde (dotted) water vapor mixing ratio (a) and relative humidity (b) profiles on May 20, 1994 at Nagoya. The lidar data were integrated from 21:36 to 22:40 JST. The radiosonde was launched at 22:16 JST and reached 12 km at 22:51 JST. The vertical resolution was 350 m.

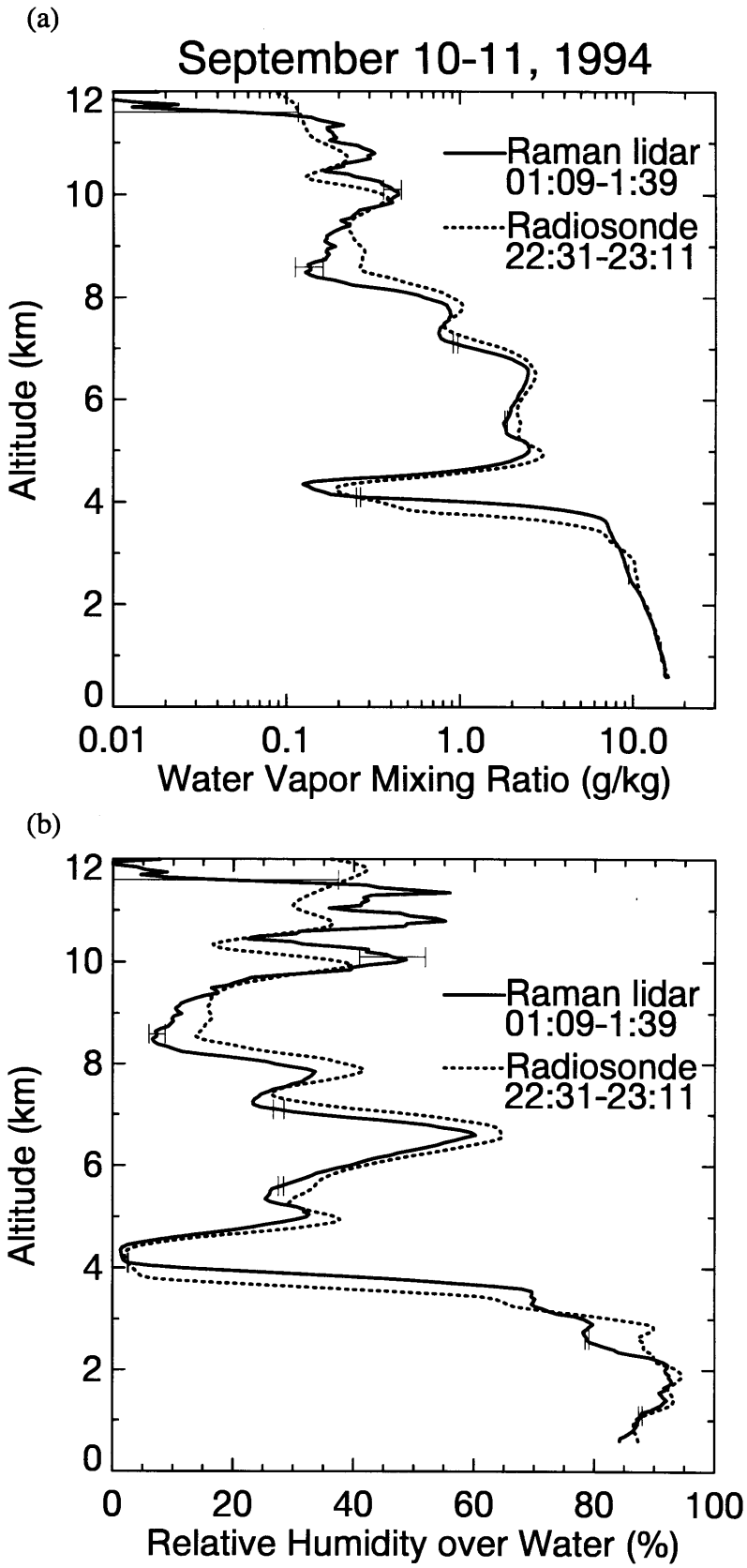

Figure 3.4 Same as Fig. 3.3 but for the profiles on September 10-11, 1994. The lidar data were integrated from 01:09 to 01:39 JST. The radiosonde was launched at 22:31 JST and reached 12 km at 23:11 JST. The vertical resolution was 350 m.

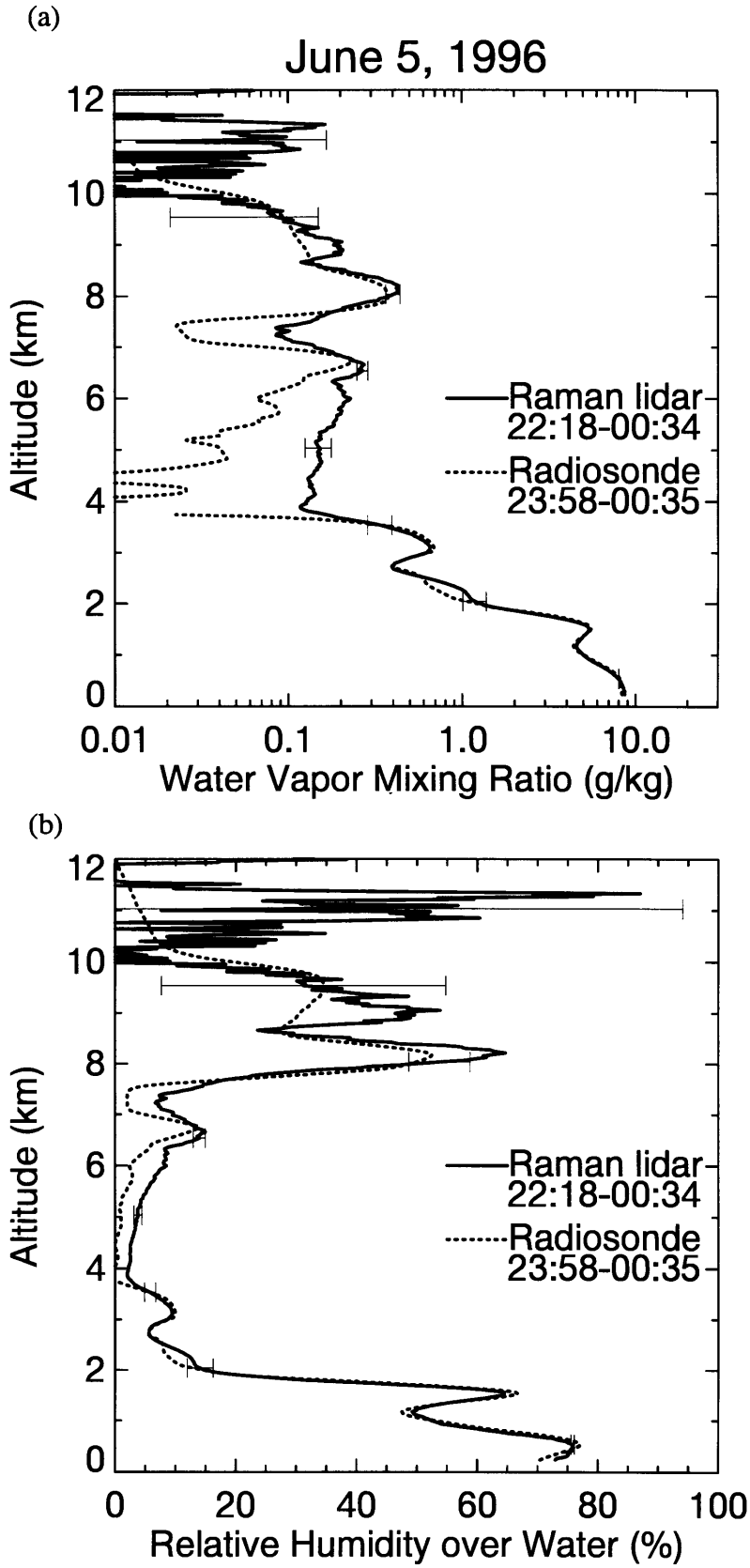

Figure 3.5 Same as Fig. 3.3 but for the profiles on June 5, 1996. The lidar data were integrated from 22:18 to 00:34 JST. The radiosonde was launched at 23:58 JST and reached 12 km at 00:35 JST. The vertical resolution was 330 m.

Considerable discrepancies were found between the humidities obtained with the two instruments at dry regions: above 6 km on May 20, 1994 (Fig. 3.3) and between 4 and 8 km on June 5, 1996 (Fig. 3.5). Figure 3.6 shows the scatter diagram of the water vapor mixing ratio between 1 and 8 km derived from the coincident radiosonde and lidar measurements made in 1994-1998 (We excluded the data on February 13, 1998 because of the low quality of the lidar data due to presence of cloud). The discrepancies are evident below the value of approximately 0.2 g kg^{-1}, where the lidar data indicated larger values than the radiosonde data. Because the calibration coefficient K was calculated by taking weighted average (Eq. 3-12), the lidar data were fitted more closely to larger values of the radiosonde - water vapor mixing ratio.

Ferrare et al. (1995) and Soden et al. (1994) have reported a systematic discrepancy in the relative humidity between the Raman lidar and Väisala radiosonde measurements. Ferrare et al. (1995) have shown that the lidar data indicated higher value of RH than the Väisala radiosonde data above the height of about 7.5 km, in which the difference of RH between them increases from 5% at 7km to 20% at 9.5 km. We made a comparison for our RH measurement data as the same manner of Ferrares', as shown in Fig. 3.7. The lidar data above 8 km indicated slight larger value than the radiosonde data. The difference was about 10% at 9 km. This tendency was consistent with Ferrares' results. However, this discrepancy might be essentially the same as that found in the dry region ($w \leq 0.2$ g kg^{-1} in Fig. 3.6) mentioned above because the value of w generally decreases with height. Ferrare et al. (1995) mentioned that the signal-induced noise (SIN) in the photomutiplier tube (PMT) might cause this discrepancy at high altitudes where the return signals are small. However, this is uncertain because it is difficult to evaluate the effect of SIN. The discrepancy cannot be explained only by the temperature variation of the effective Raman backscattering cross sections (e.g., Fig. 3.2) with height. The reason for these discrepancies remains to be solved. It may be due to the difference of the detector's sensitivity at low water vapor concentration and/or low temperature.

Table 3.1 shows the summary of the comparisons. The root mean square (RMS) difference between the lidar- and radiosonde-relative humidity between 1 and 8 km was 8% for average and varied 2~23% depending on the meteorological conditions such like cloudiness, wind speed, and horizontal inhomogeneity of the humidity. The calibration coefficients K changed when the voltages of the PMTs changed (July 18 and December 29, 1996) or the threshold levels of the discriminators changed (December 27, 1995). The temporal variation in the value of K was 6% during the period when the PMTs voltages and the discrimination levels were carefully adjusted to fixed values (from September 29, 1997 to May 19, 1998). In this study we calculated the humidity profiles for the data taken on the other days of the coincident radiosonde measurements by using the calibration coefficient obtained at the nearest coincident measurements.

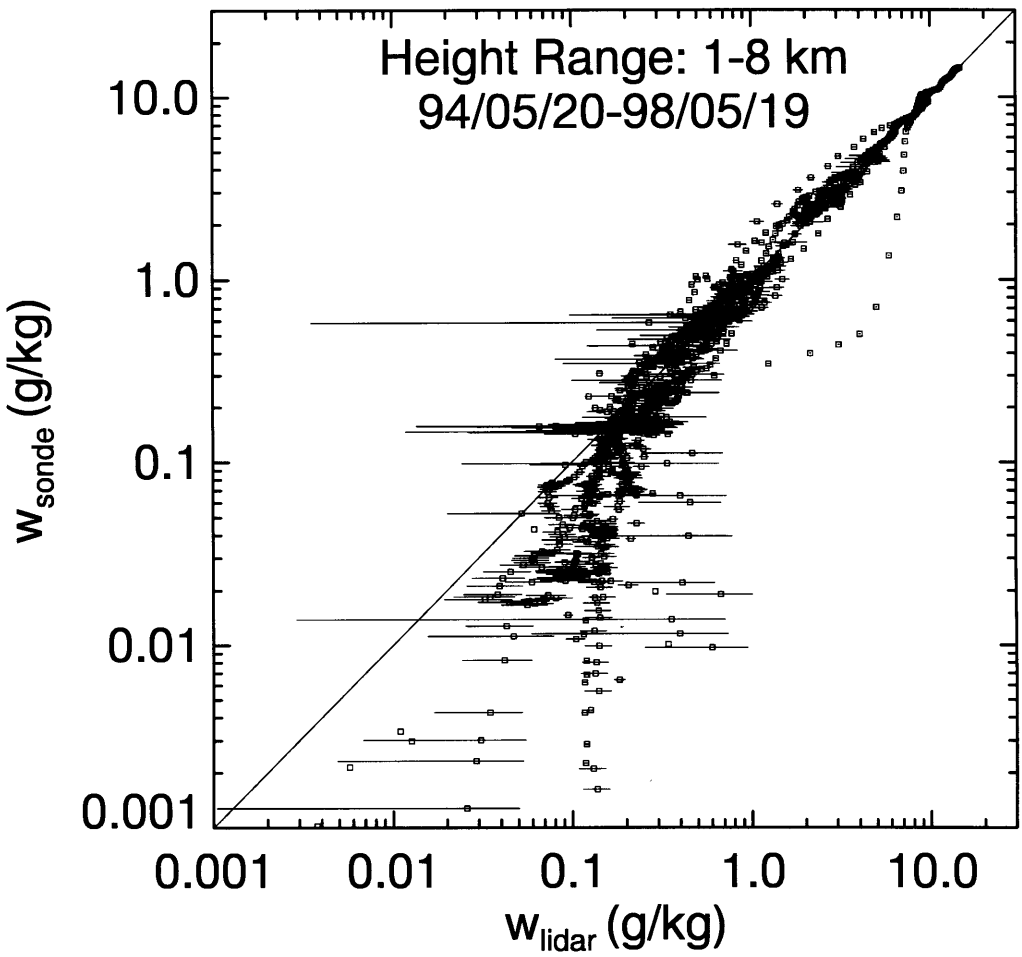

Figure 3.6 Scatter diagram of the water vapor mixing ratio between 1 and 8 km derived from the coincident radiosonde and lidar measurements in 1994-1998. The horizontal axis shows the Raman lidar value (w_{lidar}) and the vertical axis shows the Väisala radiosonde value (w_{sonde}).

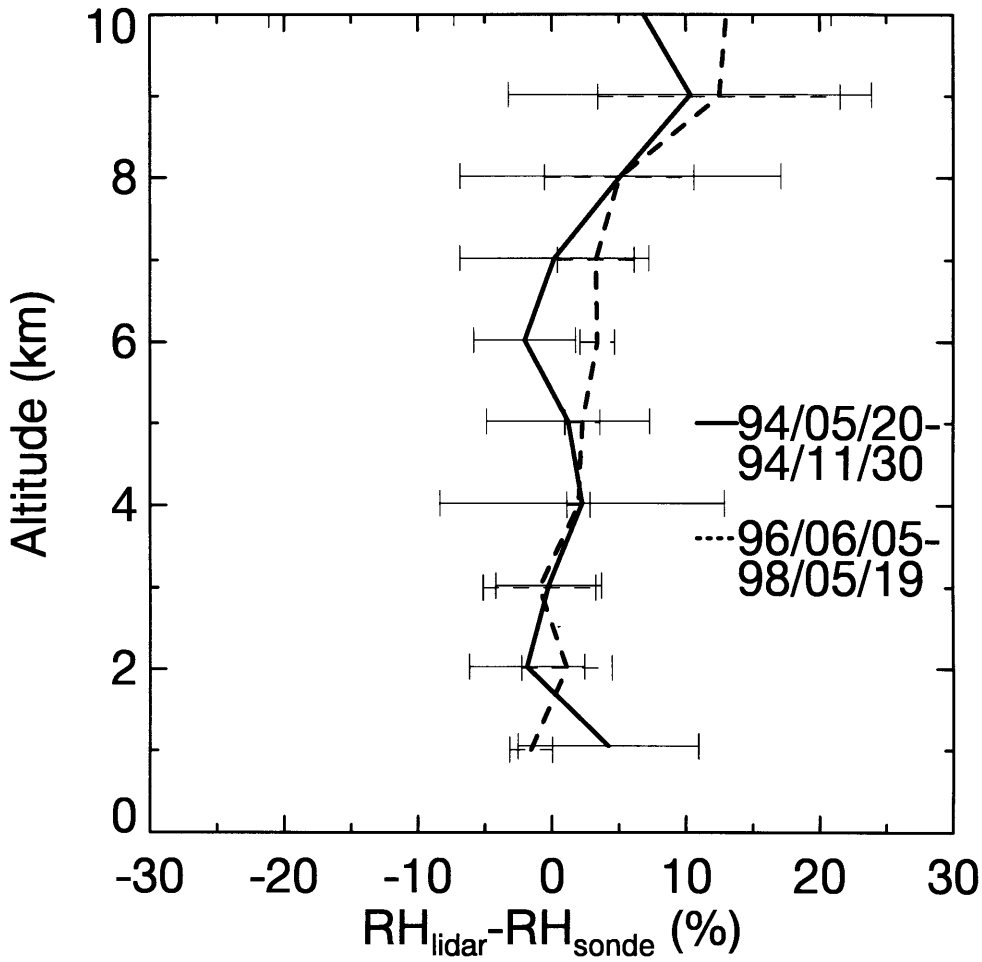

Figure 3.7 Lidar-radiosonde relative humidity difference as a function of altitude. Solid line represents the average for May 20, September 10-11, November 28 and 30, 1994 and dotted line for July 5, 1996, September 29, 1997, and May 19, 1998. The data were averaged over one kilometer bins. Horizontal bars represent the standard deviations.

Table 3.1 Summary of the comparisons between the Raman lidar and the Väisala radiosonde humidity measurements made in May 1994-May 1998

Date	Time (JST)		Calibration Coefficient K ($\times 10^{-2}$)	Coefficient of Determination r^2	RMS Difference of RH (%) between 1 and 8 km
	Radiosonde Launch-10 km	Lidar Start - End			
1994/05/20	22:16-22:45	21:36-22:40	1.40±0.04	0.996	2
1994/09/11	22:31-23:06	01:09-01:39	1.65±0.05	0.956	10
1994/11/28	21:58-22:30	20:16-21:42	2.20±0.05	0.952	10
1994/11/30	22:15-22:46	21:26-23:00	1.69±0.06	0.987	4
		(1995/12/27 Discrimination levels changed)			
1996/06/05	23:58-00:29	22:18-00:34	3.39±0.11	0.995	3
		(1996/7/18 PMTs voltages changed)			
1996/09/14	21:40-22:12	21:22-22:26	3.47±0.14	0.984	14
		(1996/12/29 PMTs voltages changed)			
1997/09/29	21:35-22:01	21:33-22:45	2.83±0.46	0.970	5
1998/02/13	22:53-23:20	22:33-23:33	3.07±1.38	0.730	23
1998/05/19	21:42-22:13	21:17-22:17	2.93±0.07	0.996	4

3.2 Aerosol extinction coefficient, backscattering ratio, aerosol backscattering coefficient, and depolarization ratio

Vertical profiles of aerosol extinction coefficient, backscattering ratio, backscattering coefficient, and depolarization ratio are calculated from the Mie/Rayleigh and Raman oxygen (nitrogen) backscatter signals. This section describes the procedure to calculate these aerosol parameters and shows some results of the calculations from the measured signals.

3.2.1 Beam overlap factor

Firstly, the beam overlap factor $O(z)$ in Eq. (3-1) must be evaluated in order to calculate the aerosol quantitative parameters in the lower altitude where the overlap factor becomes less than unity. We derived the overlap factor by two methods in this study; one is (a) to calculate the factor from the geometrical parameters of the lidar, and the other is (b) to calculate the factor from the backscatter signals measured with the lidar. The results of the calculations of the overlap factors by the two methods are presented and discussed below.

Calculation of area overlap factor from the geometrical parameter

The beam overlap factor is a function of four geometrical parameters of the lidar: (1) the area of telescope field of view overlapped with laser beam, (2) the distribution of the laser power on the target plane, (3) the area of detector's surface overlapped with the returned radiation, and (4) the distribution of detection efficiency of the detector's surface. In order to calculate the overlap factor, we need all of these parameters but the parameters (2), (3), and (4) are difficult to measure directory. Since the variation of these parameters (2)-(4) at the altitude range of our interest ($z \geq 1$ km) are expected to be small, we calculated simple area overlap factors by taking account of only the parameter of (1), i.e., the overlap factor was a function of the overlapped area of

telescope field of view with the laser beam that varied with height. In this manner, we assumed that the laser power distribution was uniform inside the beam and that the detector completely detected the backscattered radiation that came into the telescope. The former assumption might result in a steep change of the overlap factor with height because the laser power distribution is not exactly flat (the power decreases at the edge of the beam). The latter assumption might be incorrect below the height about 1 km for our system.

Figure 3.8 shows the geometry of the telescope's field of view and the laser beam of the lidar. There are three possible situations for the beam overlap (right-hand side of Fig. 3.8). The overlap factors for the three situations are respectively expressed as

$$\text{(a):}\quad O(z)=1 \text{ if } d<r-w \ \left(z>\frac{d_0-r_0+w_0}{\tan\phi_T-\tan\phi_L-\tan\theta}\right), \tag{3-13}$$

$$\text{(b):}\quad O(z)=\frac{r^2\varphi_T+w^2\varphi_L-rd\sin\varphi_T}{\pi w^2} \text{ if } r-w\le d<r+w, \tag{3-14}$$

$$\text{(c):}\quad O(z)=0 \text{ if } d\ge r+w \ \left(z\le\frac{d_0-r_0-w_0}{\tan\phi_T+\tan\phi_L-\tan\theta}\right), \tag{3-15}$$

where

$$d=d_0+z\tan\theta\,,\quad r=r_0+z\tan\phi_T\,,\quad w\cong w_0+z\tan\phi_L\,,$$

$$\varphi_T=\cos^{-1}\left(\frac{r^2+d^2-w^2}{2rd}\right), \text{ and } \varphi_L=\cos^{-1}\left(\frac{w^2+d^2-r^2}{2wd}\right).$$

Here, z is the range between the telescope and the target, d_0 is the distance between the telescope and laser axes, r_0 is the telescope radius, w_0 is the laser output aperture radius, ϕ_T is the telescope half opening angle, ϕ_L is the laser half divergence angle, and θ is the inclination angle between the telescope and laser axes. These parameters

are shown in Figs. 3.8 and 3.9. It should be noted that we consider the case for $\theta \geq 0$. The shadowing effect of the central obstruction of the telescope (secondary mirror) was neglected because this effect arises below the altitude about 0.2 km for our system.

Table 3.2 shows the geometrical scale and angular parameters of the Raman lidar system. The system emits the laser beams into the atmosphere by using two reflecting mirrors (Fig. 2.3); one reflects the beam at the wavelength of 354.7 nm and the other reflects those at 532 and 1064 nm. Thus we calculated the overlap factors for each wavelength. The unknown parameter to calculate the overlap factor is the inclination angle θ between the telescope and laser axes. Figure 3.10 shows the beam overlap factor at altitudes of 1, 2, and 5 km as a function of θ calculated for the parameters listed in Table 3.2. It is found the overlap factor significantly varies with θ. As shown in the latter subsection, we determined the values of θ by fitting the calculated overlap factor to the measured factor to minimize the difference between them.

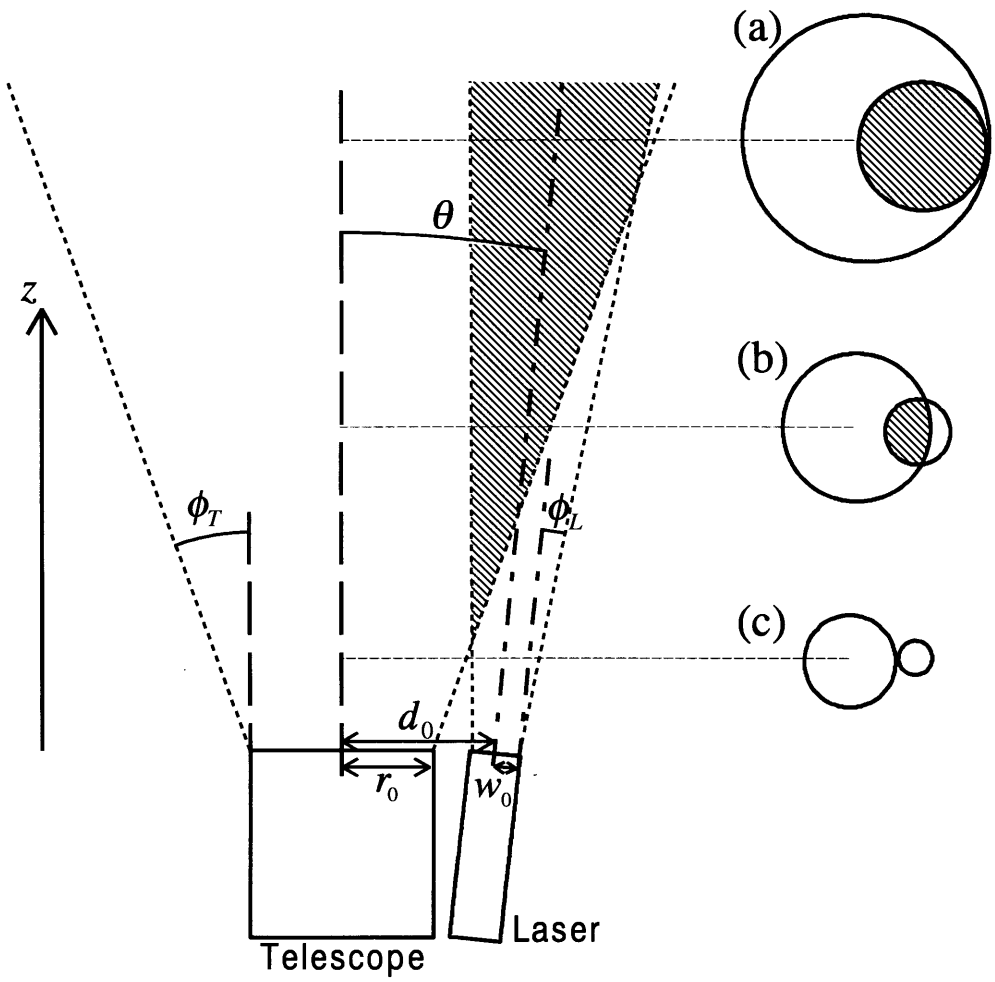

Fig. 3.8 Geometry of the telescope's field of view and the laser beam of the Raman lidar. The shaded area shows the beam overlap region. Three overlap situations (a)-(c) are shown in the right-hand side.

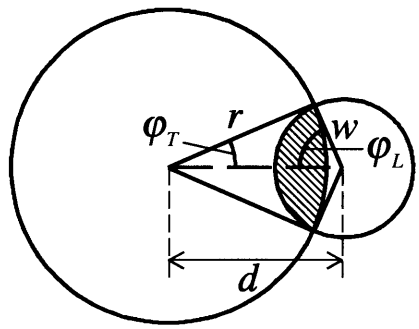

Fig. 3.9 Geometry of the target plane at height z for the situation (b) in Fig. 3.8.

Table 3.2 Geometrical scale and angular parameters of the Raman lidar

Laser				Telescope	
λ [nm]	w_0 [m]	ϕ_L [mrad]	d_0 [m]	r_0 [m]	ϕ_T [mrad]
354.7	0.018	0.1	0.752	0.502	0.75
532&1064	0.018	0.1	0.791		

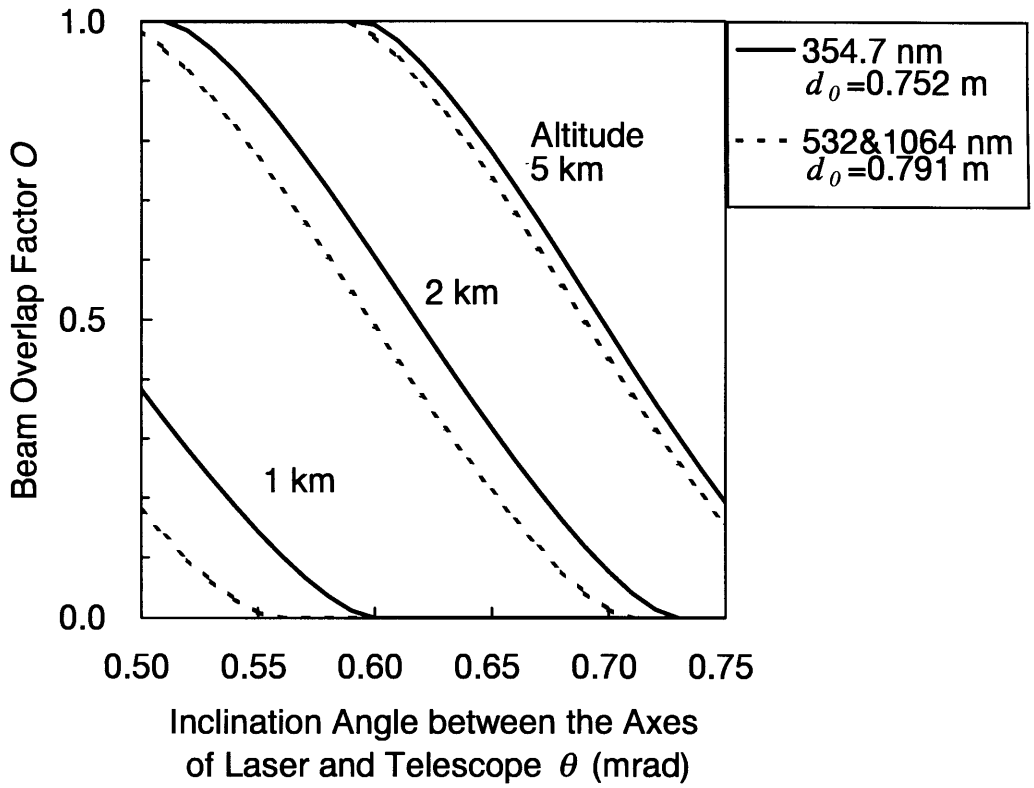

Fig. 3.10 Beam overlap factor as a function of inclination angle between the axes of laser and telescope at the altitudes of 1, 2, and 5 km calculated from the geometrical parameters.

Determination of the overlap factor from the lidar signal

The beam overlap factor can be calculated from the backscatter signal by combining with the atmospheric density data. If we assume that the laser beam completely overlaps with the telescope's field of view at an altitude z^* and all of the backscattered radiation from this altitude is detected, $O(z^*)=1$, we obtain the constant K in Eq. (3-1) as

$$K=\frac{P_\lambda(z^*)z^{*2}}{\beta(z^*)T_{\lambda_L}(z_0,z^*)T_\lambda(z_0,z^*)}. \tag{3-16}$$

Then the beam overlap factor $O(z)$ is calculated by substituting Eq. (3-16) into Eq. (3-1) and is expressed as

$$O(z)=\frac{P_\lambda(z)z^2}{P_\lambda(z^*)z^{*2}}\frac{\beta_\lambda(z^*)}{\beta_\lambda(z)}T_{\lambda_L}(z,z^*)T_\lambda(z,z^*). \tag{3-17}$$

For the Raman oxygen (nitrogen) signals, the volume backscattering coefficients $\beta_\lambda(z)$ are proportional to the number density of oxygen (nitrogen) and also to that of dry air ($n_d(z)$). Then, Eq. (3-17) becomes

$$O_{O_2}(z)=\frac{P_{O_2}(z)z^2}{P_{O_2}(z^*)z^{*2}}\frac{n_d(z^*)}{n_d(z)}e^{-\int_z^{z^*}[\sigma_{m,\lambda_L}(z')+\sigma_{a,\lambda_L}(z')]dz'}e^{-\int_z^{z^*}[\sigma_{m,\lambda_{O_2}}(z')+\sigma_{a,\lambda_{O_2}}(z')]dz'}. \tag{3-18}$$

In the calculation of the overlap factor by Eq. (3-18), we obtained the atmospheric density $n_d(z)$ and the molecular extinction coefficients $\sigma_m(z)$ from the radiosonde or GANAL (or GAPLX) data. It should be noted that we neglected the aerosol extinction coefficient, i.e., $\sigma_a(z)$=0 throughout the height in Eq. (3-18) in the

calculation because it was not available at the region where the beam overlap was incomplete.

For the Mie/Rayleigh signals, the volume backscattering coefficients $\beta_\lambda(z)$ in Eq. (3-17) are the sum of the aerosols and air molecules ($=\beta_a(z)+\beta_m(z)$). Then the equation becomes

$$O_{MR}(z)=\frac{P_{MR}(z)z^2}{P_{MR}(z^*)z^{*2}}\frac{\beta_{a,\lambda_{MR}}(z^*)+\beta_{m,\lambda_{MR}}(z^*)}{\beta_{a,\lambda_{MR}}(z)+\beta_{m,\lambda_{MR}}(z)}e^{-2\int_z^{z^*}[\sigma_{m,\lambda_{MR}}(z')+\sigma_{a,\lambda_{MR}}(z')]dz'}. \quad (3\text{-}19)$$

The molecular backscattering coefficients $\beta_m(z)$ and extinction coefficients $\sigma_m(z)$ were obtained from the radiosonde or GANAL (or GAPLX) data. Again we must notice that we neglected the coefficients of aerosol backscattering $\beta_a(z)$ and extinction $\sigma_a(z)$ to calculate the overlap factor by Eq. (3-19) because we have no data for them in the incomplete beam overlap region. Accordingly, the derived overlap factor becomes incorrect as the amount of aerosol particles increases. Thus we had to calculate the overlap factor from the data taken under the atmospheric condition of small aerosol loading as possible.

Results

Case 1: Raman oxygen measurements

Figure 3.11 shows the beam overlap factor derived from the Raman oxygen signal and that calculated from the geometrical parameters on November 30, 1994. The measurement was carried out under fairly clear condition. We used the atmospheric density data obtained with the coincident radiosonde launched approximately 30 m away from the lidar to calculate the factor by Eq. (3-18). We set the normalization height z^* at 5.0 km. The measured overlap factor was 0.72 at 2.0 km and reached unity at 3.6 km. The inclination angle θ between the laser and telescope axes was calculated to be 0.580 mrad by fitting the calculated values to the measured values between 2.0

and 5.0 km. The mean relative difference between them was 4% at the altitude range of 1.0 to 5.0 km. Below approximately 2 km the measured and calculated overlap factors showed some discrepancy; the measured overlap factor was smaller than the calculated factor at 1.2-2.0 km and larger below 1.2 km. This discrepancy was probably due to the assumptions we made. To investigate the reason for this discrepancy, we calculated the overlap factor for the Gaussian laser beam distribution (not shown). However, the goodness of fitting between the calculated value and the measured one was worse than that of the flat laser distribution. We believe that the most probable reason for this discrepancy is the backscattered radiation from the altitude below 2 km was incompletely focused onto the focal plane of the receiver's optics.

Figure 3.12 shows the beam overlap factors obtained on the days of the coincident radiosonde measurements. The overlap factor obtained on November 28 agreed well with that on November 30; the mean difference between them was 3% at the altitude range of 1.0-5.0 km. On the other hand, the overlap factor on May 20 showed unrealistic values ($O(z) \geq 1$) at 2.5-6.0 km due to the aerosol extinction we neglected; this was confirmed by the fact that the simultaneous Mie/Rayleigh measurements at 532 nm indicated significant amounts of aerosol backscattering in this region (not shown). The overlap factor on September 11 was considerably smaller than those on the other days. The reasons for this difference is not well understood. One possible reason is that we carried out the measurements on September 11 with a focal length and/or aperture setting that was different from the measurements on the other days. Another possibility is that the inclination angle between the telescope and laser axes had changed by some unexpected reasons.

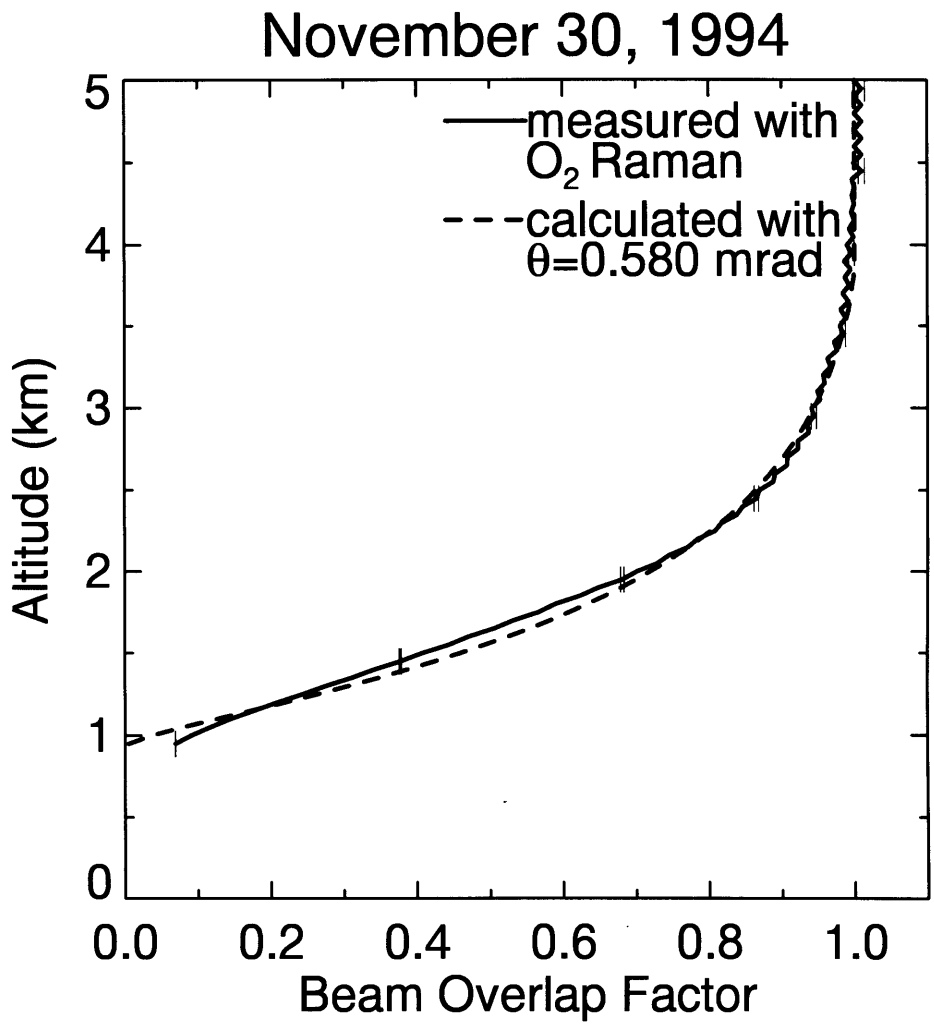

Fig. 3.11 Beam overlap factor for the 354.7/Raman channels obtained on November 30, 1994. The solid line shows the factor derived from the Raman oxygen measurement and the dashed line shows the factor calculated from the geometrical parameters with θ=0.580 mrad.

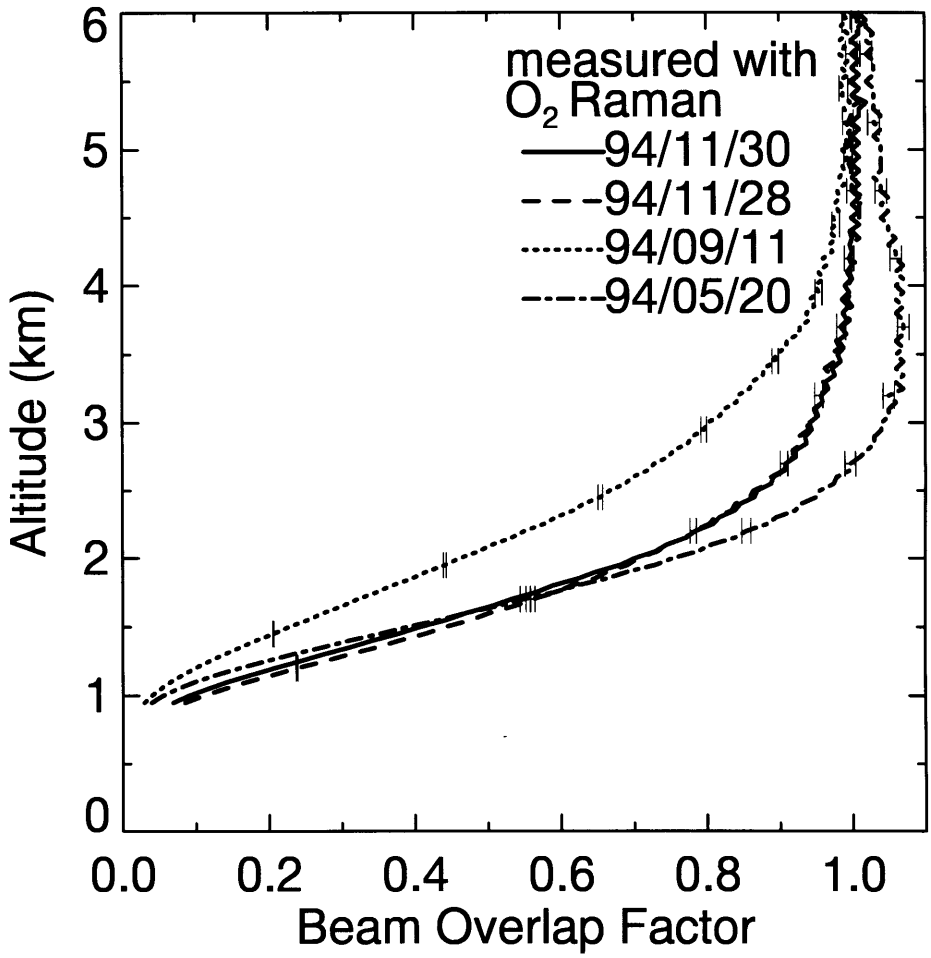

Fig. 3.12 Beam overlap factors for the 354.7/Raman channels derived from the Raman oxygen measurements on May 20, September 11, November 28, and November 30, 1994.

Case 2: Mie/Rayleigh measurements

The determination of the beam overlap factor from the Mie/Rayleigh signal by Eq. (3-19) is a hard task because we have no information about the aerosol backscattering and extinction coefficients in the incomplete overlap region as mentioned previously. We calculated the beam overlap factor from the Mie/Rayleigh signal at 532 nm without taking account of the aerosol backscattering and extinction on November 30, 1994, when the measurement was carried out under the clearest condition in all the coincident radiosonde measurements. Figure 3.13 shows the results of the measurements on November 30. We set the normalization height z^* at 3.9 km. The inclination angle θ was calculated to be 0.562 mrad by fitting the calculated values to the measured ones between 3.0 and 4.0 km. The measured and the calculated overlap factors substantially deviated below 3.0 km due to the aerosol backscattering that we neglected.

Figure 3.14 shows the vertical profiles of the backscattering ratio at 532 nm on November 30 calculated by using the overlap factor obtained from the calculation with $\theta = 0.562\,\text{mrad}$ (corrected) and that calculated with constant overlap factor over the range ($O(z) = 1$, uncorrected). The corrected values of the backscattering ratio below 3 km were reasonable in the sense that they were larger than unity, while the uncorrected values were less than unity between 1.8 and 3 km. Although the precision of the calculated overlap factor for the Mie/Rayleigh channel is uncertain, we believe that the factor is reliable above 2 km because the overlap factor calculated from the geometrical parameters on November 30 agreed well with that derived from the Raman oxygen measurement above 2 km (Fig. 3.11).

We calculated the beam overlap factors for each wavelength as a function of θ for all the data taken under the clear conditions in 1994-1997. The values of θ varied between about 0.55 and 0.60 mrad. This variation corresponds to the variation of the overlap factors between 0.87 and 0.61 for 354.7 nm and between 0.77 and 0.49 for 532 and 1064 nm at 2 km. We used the calculated overlap factors as a function of θ in the

calculation of the aerosol backscattering and extinction coefficient profiles. For the data taken under fairly turbid conditions for which calculation of θ by fitting the calculated factor to the measured one were difficult, we used the values obtained by interpolating those obtained under clear conditions on the nearest days.

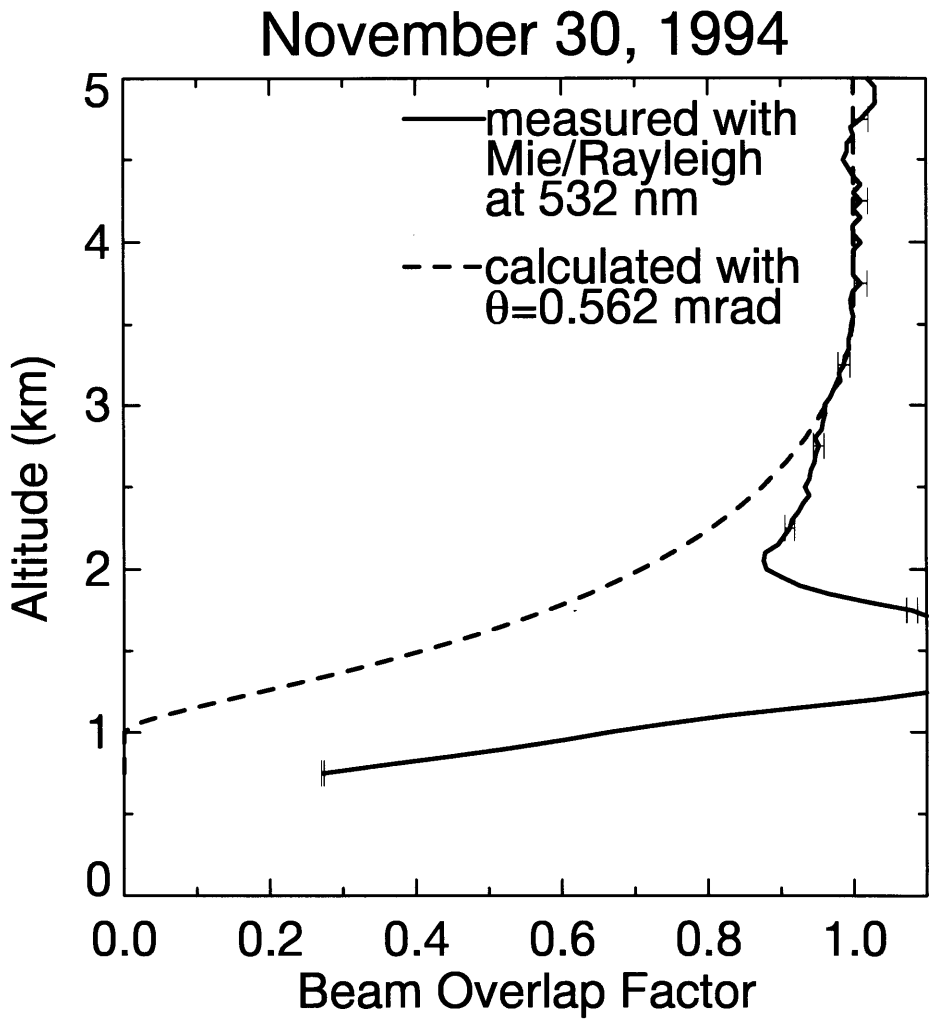

Fig. 3.13 Beam overlap factor for the 532 nm channels obtained on November 30, 1994. The solid line shows the factor derived from the Mie/Rayleigh measurement at 532 nm and the dashed line shows the calculated factor with θ =0.562 mrad.

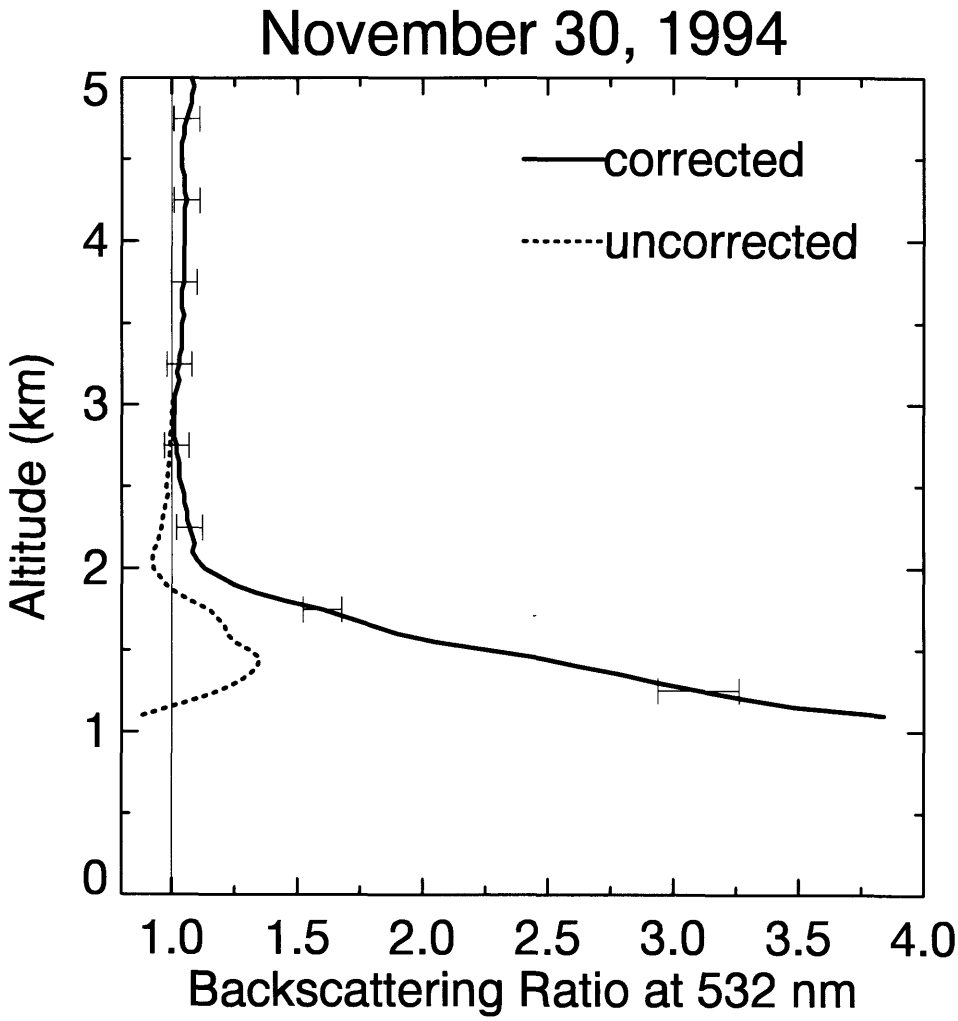

Fig. 3.14 Vertical profiles of the backscattering ratio at 532 nm on November 30, 1994. The solid line shows the profile calculated by using the overlap factor calculated with θ=0.562 mrad. The dotted line shows the profiles calculated with constant overlap factor of unity ($O(z)=1$).

3.2.2 Aerosol extinction coefficient

Aerosol extinction coefficient (σ_a) is calculated from the Raman oxygen (or nitrogen) signal (e.g., Ansmann et al., 1990). The lidar signal of the Raman oxygen backscattering is expressed by

$$P_{O_2}(z) = K_{O_2} \frac{O_{O_2}(z)}{z^2} \frac{d\sigma_{O_2}(\pi)}{d\Omega} n_{O_2}(z) e^{-\int_{z_0}^{z} [\sigma_{m,\lambda_L}(z') + \sigma_{a,\lambda_L}(z') + \sigma_{m,\lambda_{O_2}}(z') + \sigma_{a,\lambda_{O_2}}(z')] dz'}, \quad (3\text{-}20)$$

where λ_L and λ_{O_2} are the wavelengths of the laser (354.7 nm) and the Raman oxygen scattering (375.4 nm), respectively. By differentiating the logarithm of Eq. (3-20) with respect to z, we obtain

$$\frac{d}{dz}\left[ln\left(\frac{P_{O_2}(z)z^2}{O_{O_2}(z)n_d(z)}\right)\right] = -[\sigma_{m,\lambda_L}(z) + \sigma_{a,\lambda_L}(z) + \sigma_{m,\lambda_{O_2}}(z) + \sigma_{a,\lambda_{O_2}}(z)]. \quad (3\text{-}21)$$

Here we assume that the number fraction of oxygen molecule in air is constant ($n_{O_2} \propto n_d$) at the heights over which the measurements are made. The extinction coefficients at the two wavelengths have relations that are expressed by

$$\frac{\sigma_{m,\lambda_{O_2}}(z)}{\sigma_{m,\lambda_L}(z)} = \left(\frac{\lambda_{O_2}}{\lambda_L}\right)^{-4} \quad (3\text{-}22)$$

for air molecules, and

$$\frac{\sigma_{a,\lambda_{O_2}}(z)}{\sigma_{a,\lambda_L}(z)} = \left(\frac{\lambda_{O_2}}{\lambda_L}\right)^{-k(z)} \quad (3\text{-}23)$$

for aerosol particles. The exponent k in Eq. (3-23) is called Ångström exponent (Ångström, 1964) which depends on the size, shape, ant the refractive index of the particles and must be given explicitly (the method for estimating the value of k is

described in Section 3.2.5). By substitution of Eqs. (3-22) and (3-23) into Eq. (3-21), we obtain the aerosol extinction coefficient at λ_L.

$$\sigma_{a,\lambda_L}(z)=\frac{1}{1+(\lambda_{O_2}/\lambda_L)^{-k(z)}}\left\{\frac{d}{dz}\left[ln\left(\frac{O_{O_2}(z)n_d(z)}{P_{O_2}(z)z^2}\right)\right]-\left[1+\left(\frac{\lambda_{O_2}}{\lambda_L}\right)^{-4}\right]\sigma_{m,\lambda_L}(z)\right\} \quad [m^{-1}]. \tag{3-24}$$

In order to compute the extinction profile from the actual lidar data, we used the finite differential form of Eq. (3-24) that is expressed by

$$\sigma_{a,\lambda_L}(z)=\frac{1}{1+(\lambda_{O_2}/\lambda_L)^{-k(z)}}\left\{\frac{1}{\Delta z}\left[ln\left(\frac{P_{O_2}(z-\frac{\Delta z}{2})(z-\frac{\Delta z}{2})^2O_{O_2}(z+\frac{\Delta z}{2})n_d(z+\frac{\Delta z}{2})}{P_{O_2}(z+\frac{\Delta z}{2})(z+\frac{\Delta z}{2})^2O_{O_2}(z-\frac{\Delta z}{2})n_d(z-\frac{\Delta z}{2})}\right)\right]-\left[1+\left(\frac{\lambda_{O_2}}{\lambda_L}\right)^{-4}\right]\sigma_{m,\lambda_L}(z)\right\} \quad [m^{-1}]. \tag{3-25}$$

Measurement uncertainty in the aerosol extinction coefficient

The measurement uncertainty in the aerosol extinction coefficient is calculated by

$$\delta\sigma_{a\lambda_L}(z)=\frac{1}{\Delta z[1+(\lambda_{O_2}/\lambda_L)^{-k(z)}]}\left\{\left(\frac{\delta P_{O_2}(z+\frac{\Delta z}{2})}{P_{O_2}(z+\frac{\Delta z}{2})}\right)^2+\left(\frac{\delta P_{O_2}(z-\frac{\Delta z}{2})}{P_{O_2}(z-\frac{\Delta z}{2})}\right)^2+\left(\frac{\delta n_d(z+\frac{\Delta z}{2})}{n_d(z+\frac{\Delta z}{2})}\right)^2+\left(\frac{\delta n_d(z-\frac{\Delta z}{2})}{n_d(z-\frac{\Delta z}{2})}\right)^2+\left(\left[1+\left(\frac{\lambda_{O_2}}{\lambda_L}\right)^{-4}\right]\delta\sigma_{m\lambda_L}\right)^2\right\}^{\frac{1}{2}}$$
$$+\frac{(\lambda_{O_2}/\lambda)^{-k(z)}\left|ln(\lambda_{O_2}/\lambda_L)\right|}{1+(\lambda_{O_2}/\lambda_L)^{-k(z)}}\sigma_{a\lambda_L}(z)\delta k(z). \tag{3-26}$$

3.2.3 Backscattering ratio and aerosol backscattering coefficient

The signal of Mie/Rayleigh backscattering is expressed by

$$P_{MR}(z) = K_{MR}\frac{O_{MR}(z)}{z^2}[\beta_{m,\lambda_{MR}}(z)+\beta_{a,\lambda_{MR}}(z)]e^{-2\int_{z_0}^{z}[\sigma_{m,\lambda_{MR}}(z')+\sigma_{a,\lambda_{MR}}(z')]dz'}, \quad (3\text{-}27)$$

where $\beta_{m,\lambda_{MR}}$ and $\beta_{a,\lambda_{MR}}$ are the volume backscattering coefficients of air molecules and aerosol particles at the wavelength $\lambda_{MR}(=\lambda_L=$ 532 or 1064 nm in this study), respectively.

The backscattering ratio (R) is calculated by employing the normalization procedure (e.g., Russell et al., 1979) that is expressed as

$$R_{\lambda_{MR}}(z) = \frac{\beta_{m,\lambda_{MR}}(z)+\beta_{a,\lambda_{MR}}(z)}{\beta_{m,\lambda_{MR}}(z)} = R_{\lambda_L}(z^*)\frac{O_{\lambda_{MR}}(z^*)P_{\lambda_{MR}}(z)z^2 n_d(z^*)}{O_{\lambda_{MR}}(z)P_{\lambda_{MR}}(z^*)z^{*2} n_d(z)}e^{-2\int_{z}^{z^*}[\sigma_{m,\lambda_{MR}}(z')+\sigma_{a,\lambda_{MR}}(z')]dz'}, \quad (3\text{-}28)$$

where z^* is the normalization height for the backscattering ratio. The normalization was carried out for $R=1$ at an altitude between about 28 and 30 km where backscattering by particles is considered to be negligible. The volume backscattering coefficient of aerosol particles (β_a) is obtained from Eq. (3-28) as

$$\beta_{a,\lambda_{MR}}(z) = \beta_{m,\lambda_{MR}}(z)[R_{\lambda_{MR}}(z)-1] \quad [\mathrm{m^{-1}sr^{-1}}]. \quad (3\text{-}29)$$

The volume backscattering coefficient of air molecules (β_m) is calculated by

$$\beta_{m,\lambda}(z) = \frac{27\pi^2(n_s^2-1)^2 n_d(z)}{\lambda^4 N_s^2(n_s^2+2)^2}\left(\frac{\rho_v^{\Delta\lambda}+1}{3-4\rho_v^{\Delta\lambda}}\right) \quad [\mathrm{m^{-1}sr^{-1}}], \quad (3\text{-}30)$$

where n_s and N_s are the same as Eq. (3-5), $\rho_v^{\Delta\lambda}$ is the depolarization factor that depends on the wavelength and the bandwidth of the measurement. The vales are calculated to be $\rho_v^{\Delta\lambda} = 4.9\times10^{-3}$ at 532 nm (FWHM=1.17 nm) and $\rho_v^{\Delta\lambda} = 3.4\times10^{-3}$ at 1064 nm (FWHM=1.10 nm) for our system at the tropospheric temperature range (Adachi, private communication).

In order to calculate the value of $R_{\lambda_{MR}}$ by Eq. (3-28), the aerosol extinction coefficient $\sigma_{a,\lambda_{MR}}(z)$ is needed. This parameter is crucial for the calculation of R in the turbid atmosphere. The value of $\sigma_{a,\lambda_{MR}}$ can be calculated by two methods from our observational data. One is to calculate $\sigma_{a,\lambda_{MR}}$ from the Raman oxygen signal by Eq. (3-25) and assuming the same relation as Eq. (3-23):

$$\sigma_{a,\lambda_{MR}}(z) = \left(\frac{\lambda_{MR}}{\lambda_L}\right)^{-k(z)} \sigma_{a,\lambda_L}(z), \tag{3-31}$$

where λ_L is 354.7 nm in this study. The other is to calculate $\sigma_{a,\lambda_{MR}}$ from the aerosol backscattering coefficient $\beta_{a,\lambda_{MR}}$ by assuming the conventional relation (e.g., Fernald, 1984; Klett, 1981)

$$\sigma_{a,\lambda_{MR}}(z) = S_{a,\lambda_{MR}}(z)\beta_{a,\lambda_{MR}}(z), \tag{3-32}$$

where $S_{a,\lambda_{MR}}$ is the extinction-to-backscatter ratio of aerosol particles which depend on the size, shape and the refractive index of the particles (discussed in the following section). The data analyzing procedure used in this study to calculate R, β_a, and σ_a simultaneously by combining the Raman oxygen and Mie/Rayleigh signals is described in Section 3.2.5.

Measurement uncertainty in the backscattering ratio and the aerosol backscattering coefficient

The measurement uncertainty in the backscattering ratio is given by

$$\delta R_{\lambda_{MR}}(z) = R_{\lambda_{MR}}(z)\left\{\left(\frac{\delta R_{\lambda_{MR}}(z^*)}{R_{\lambda_{MR}}(z^*)}\right)^2+\left(\frac{\delta P_{\lambda_{MR}}(z^*)}{P_{\lambda_{MR}}(z^*)}\right)^2+\left(\frac{\delta P_{\lambda_{MR}}(z)}{P_{\lambda_{MR}}(z)}\right)^2+\left(\frac{\delta n_d(z^*)}{n_d(z^*)}\right)^2+\left(\frac{\delta n_d(z)}{n_d(z)}\right)^2+4\delta\tau_{m,\lambda_{MR}}(z,z^*)^2+4\delta\tau_{a,\lambda_{MR}}(z,z^*)^2\right\}^{\frac{1}{2}}, \tag{3-33}$$

where

$$[\delta\tau_{m,\lambda_{MR}}(z,z^*)]^2 = \Delta z^2\sum_{z'=z^*}^{z}[\delta\sigma_{m,\lambda_{MR}}(z')]^2 \tag{3-34}$$

and

$$[\delta\tau_{a,\lambda_{MR}}(z,z^*)]^2 = \Delta z^2\sum_{z'=z^*}^{z}[\delta\sigma_{a,\lambda_{MR}}(z')]^2 . \tag{3-35}$$

It should be noted we omitted the covariance term for the molecular backscattering in Eq. (3-33) so that the calculated uncertainty in R might be overestimated at the altitude region $|z-z^*| \le \Delta z_d$ where Δz_d is the resolution of the atmospheric density data (Russell et al., 1979).

The measurement uncertainty in the aerosol extinction coefficient at the Mie/Rayleigh wavelength ($\delta\sigma_{a,\lambda_{MR}}$) in Eq. (3-35) is calculated by following manner: If the aerosol extinction coefficients are derived from the Raman oxygen backscatter signal by Eqs. (3-25) and (3-31), the uncertainty is given by

$$[\delta\sigma_{a,\lambda_{MR}}(z)]^2 = \sigma_{a,\lambda_{MR}}(z)^2\left[\left(\frac{\delta\sigma_{a,\lambda_L}(z)}{\sigma_{a,\lambda_L}(z)}\right)^2 + ln^2\left(\frac{\lambda_{MR}}{\lambda_L}\right)[\delta k(z)]^2\right] \tag{3-36}$$

where λ_L is the wavelength of the aerosol extinction measurement (=354.7 nm in this study). If the aerosol extinction coefficients are derived from the backscattering coefficients by Eq. (3-32), the uncertainty is given by

$$[\delta\sigma_{a,\lambda_{MR}}(z)]^2 = [S_{a,\lambda_{MR}}(z)\beta_{a,\lambda_{MR}}(z)]^2\left[\left(\frac{\delta S_{a,\lambda_{MR}}(z)}{S_{a,\lambda_{MR}}(z)}\right)^2+\left(\frac{\delta n_d(z)}{n_d(z)}\right)^2+\left(\frac{\delta R_{\lambda_{MR}}(z)}{R_{\lambda_{MR}}(z)-1}\right)^2\right]. \quad (3\text{-}37)$$

The measurement uncertainty in the aerosol backscattering coefficient is given by

$$\delta\beta_{a,\lambda_{MR}}(z) = \beta_{a,\lambda_{MR}}(z)\left[\left(\frac{\delta n_d(z)}{n_d(z)}\right)^2+\left(\frac{\delta R_{\lambda_{MR}}(z)}{R_{\lambda_{MR}}(z)-1}\right)^2\right]^{\frac{1}{2}}. \quad (3\text{-}38)$$

The calculations of $\delta\beta_a$ and δR are made by an iterative manner if we use Eq. (3-37) (Russell et al., 1979).

3.2.4 Results of aerosol extinction and backscattering measurements

Figure 3.15 shows the vertical profiles of the aerosol extinction coefficient at 354.7 nm ($\sigma_{a,355}$) and the backscattering coefficient at 532 nm ($\beta_{a,532}$) observed on April 21 and November 30, 1994. The data were accumulated for 30 minutes on April 21 and for 90 minutes on November 30. The vertical resolution was reduced to 750 m by taking running mean. The values of $\sigma_{a,355}$ and $\beta_{a,532}$ were calculated by Eq. (3-25) and Eqs. (3-29)–(3-31), respectively. We calculated two profiles for each aerosol parameters assuming the wavelength exponent of the aerosol extinction coefficient as k=0 and k=1.5 because the values of k for tropospheric aerosols generally take between these values (Tanaka et al., 1989); thus the appropriate values of $\sigma_{a,355}$ and $\beta_{a,532}$ were expected to be between the values calculated with the two k values.

The profiles on April 21 (Fig. 3.15a) were taken under rather turbid condition. Large amount of nonspherical particles that had been transported from over the Asian Continent (described in Section 4.2) were present in the free troposphere. The peak value of $\sigma_{a,355}$ at 5 km was 6.5×10^{-5} m^{-1} for $k=0$ and 6.8×10^{-5} m^{-1} for $k=1.5$. The values of $\sigma_{a,355}$ calculated for the two k values differ by 4% independent of the height. The measurement uncertainty in $\sigma_{a,355}$ was about 15% at 5 km and increased with height and exceeded 100% above 8 km. The aerosol optical thickness between 3 and 8 km was 0.18 for $k=0$ and 0.19 for $k=1.5$.

The aerosol backscattering coefficient $\beta_{a,532}$ on April 21 showed a peak at 4.6 km whose value was 1.3×10^{-6} $m^{-1}sr^{-1}$ ($k=0$) and 1.5×10^{-6} $m^{-1}sr^{-1}$ ($k=1.5$). The values of the $\beta_{a,532}$ calculated for the two k values deviated as the height decreases; the differences of the values of $\beta_{a,532}$ for the two k values were 13% at 5 km and 27% at 3 km. This is because the difference in the calculated aerosol optical thickness between the normalization height (z^* =9.3 km) and the target height for the two k values becomes

large as the height decreases. The measurement uncertainties in $\beta_{a,532}$ were about 9% at 5 km and 34% at 8 km for the both profiles calculated with the two k values.

The profiles on November 30 (Fig. 3.15b) were taken under fairly clear condition. The values of $\beta_{a,532}$ indicated fairly low values ($\leq 1.3\times10^{-7}$) which were less than 10^{-1} of those observed on April 21. The data of $\sigma_{a,355}$ were almost out of the detection limit (measurement uncertainty exceeded 100%) over a height range of the measurement.

For the data taken during the period 1994 to 1997, the minimum detection level (relative uncertainty < 100%) of the $\sigma_{a,355}$ was about 1.2×10^{-5} m^{-1} with time resolutions of 30-90 minutes and the vertical resolution of 750 m. Accurate aerosol extinction data (relative uncertainty < 30%) have been obtained under fairly turbid conditions ($\sigma_{a,355} \geq 4\times10^{-5}$ m^{-1}) such like substantial amount of dust particles or thin cirrus clouds were present.

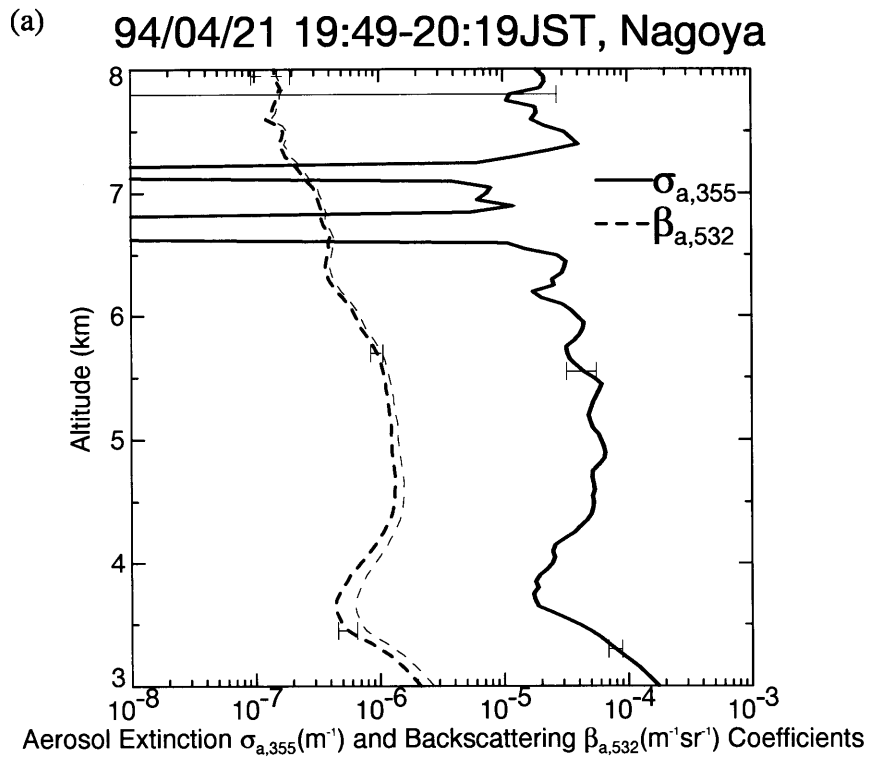

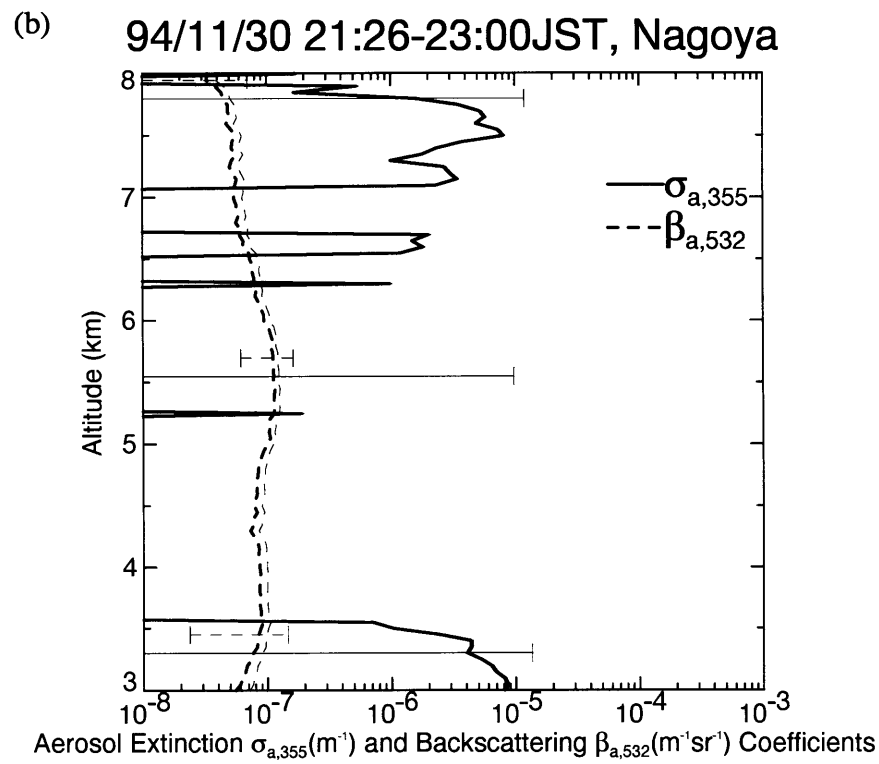

Figure 3.15 Vertical profiles of aerosol extinction coefficient at 354.7 nm (solid lines) and backscattering coefficient at 532 nm (dashed lines) observed on (a) April 21 and (b) November 30, 1994. The thick lines show the data calculated with the wavelength exponent of aerosol extinction coefficient $k = 0$ and the thin lines show the data calculated with $k = 1.5$.

Extinction-to-backscatter ratio of mineral dusts and ice crystals

The aerosol extinction-to-backscatter ratio depends of the size, shape and the refractive index of the particles and is an important input parameter to deduce the aerosol extinction and/or backscattering coefficient from the Mie/Rayleigh lidar signal alone (e.g., Klett, 1981; Fernald, 1984; Sasano et al., 1985). The aerosol extinction-to-backscatter ratio can be obtained by taking the ratio of the extinction coefficient and the backscattering coefficient that are both available from the Raman lidar signals. Figure 3.16 shows the vertical profiles of backscattering ratio at 532 nm, relative humidity, aerosol extinction-to-backscatter ratio at 532 nm ($S_{a,532}$), aerosol depolarization ratio at 532 nm, wavelength exponent of the aerosol backscattering coefficient (α) observed on April 21, 1994. We calculated the $S_{a,532}$ from the values of $\sigma_{a,355}$ and $\beta_{a,532}$ shown in Fig. 3.15 assuming $k = 0$ and $k = 1.5$. At the altitude range of 3 to 6 km, where relatively large backscattering ratios ($R \geq 1.5$) were observed, the values of $S_{a,532}$ were between 13 and 37 sr for $k = 1.5$ and between 28 and 89 sr for $k = 0$.

Figure 3.17 shows the profiles observed on January 10, 1997. A sharp peak of the backscattering ratio were observed at around 6.8 km with a height thickness about 1 km, in which the $S_{a,532}$ indicated small values about 6 sr ($k = 1.5$) and 12 sr ($k = 0$). It should be noted that the relative humidities in this region were near saturated with respect to ice.

Takamura et al. (1994) measured the $S_{a,532}$ values of the tropospheric aerosols by using the Mie/Rayleigh lidar and sun photometer at Tsukuba. They reported the values of $S_{a,532}$ ranged between 20 and 70. This range of the values was close to those observed at 3-6 km on April 21 but significantly larger than those at around 6.8 km on January 10.

The values of $S_{a,532}$ for the two k values obtained from our data differs by about a factor of two because of relatively large difference in the measurement wavelengths of the extinction (354.7 nm) and backscattering (532 nm). More accurate value of $S_{a,532}$

could be obtained if we measured the extinction at 532 nm by detecting the Raman oxygen scattering excited by 532 nm (λ_{O_2} = 580.2 nm).

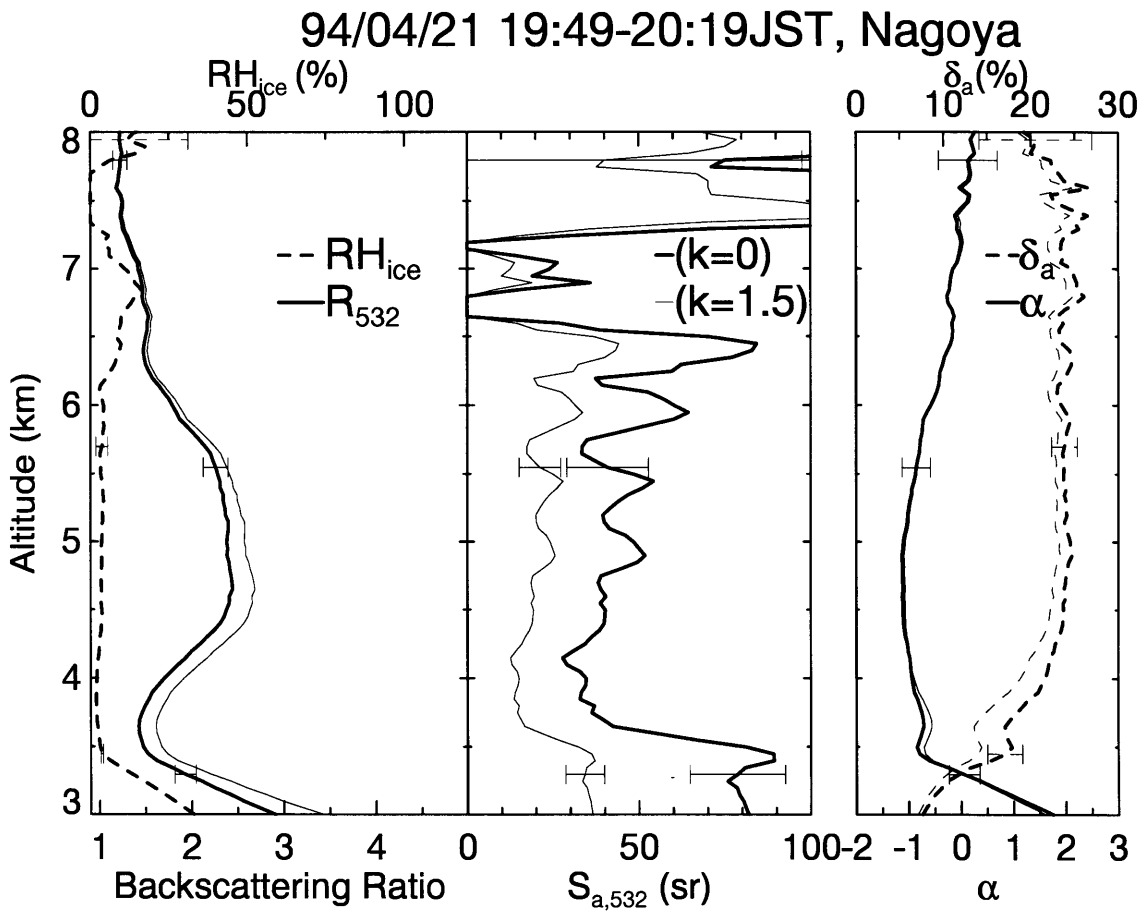

Figure 3.16 Vertical profiles observed with the Raman lidar on April 21, 1994. Left panel shows the backscattering ratio at 532 nm (solid lines) and relative humidity over ice (dashed line). Middle panel shows the aerosol extinction-to-backscatter ratio at 532 nm. Right panel shows the wavelength exponents of the backscattering coefficients between 532 and 1064 nm (solid lines) and the aerosol depolarization ratio (dashed lines). Thick lines correspond to the profiles calculated with $k = 0$ and thin lines correspond to the profiles calculated with $k = 1.5$.

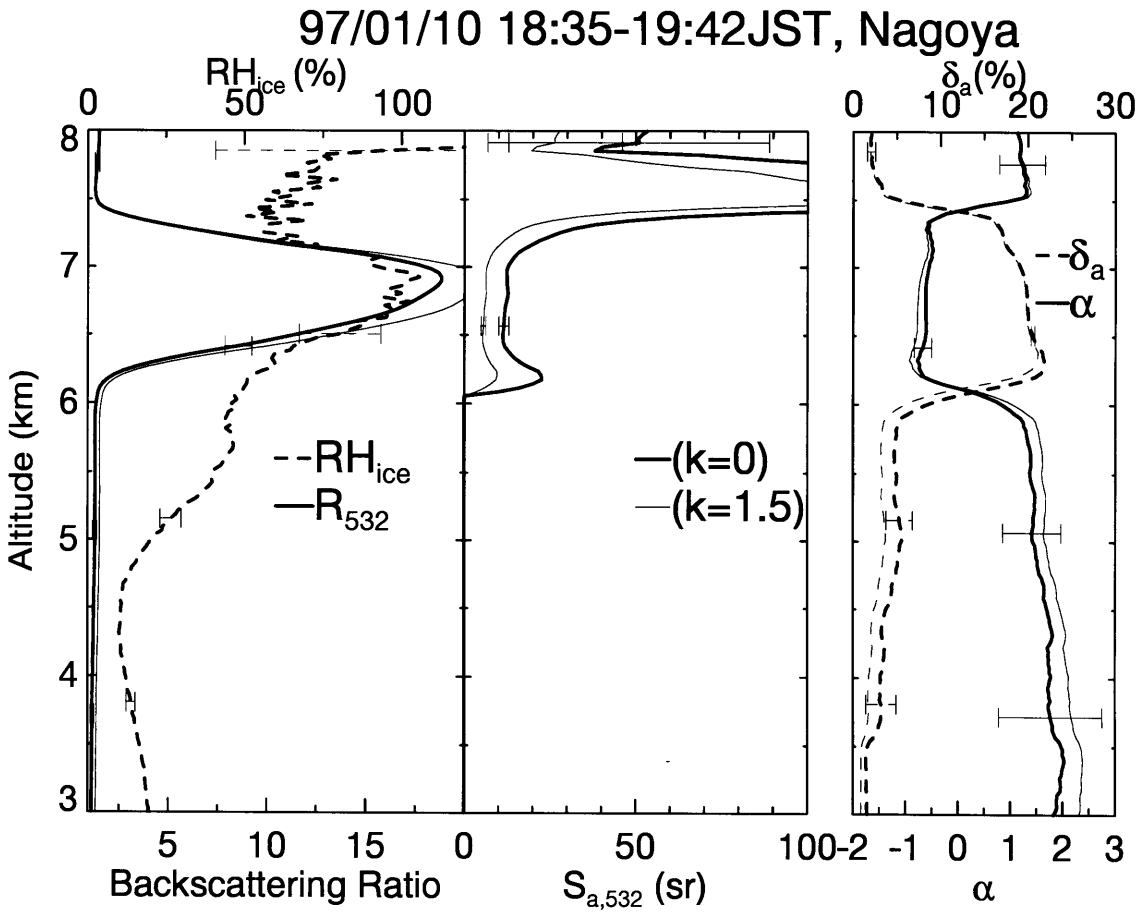

Figure 3.17 Same as Fig. 3.16 but for the profiles observed on January 10, 1997.

Although the uncertainty in $S_{a,532}(=\sigma_{a,532}/\beta_{a,532})$ derived from our measured signals is relatively large because of the difference in the measurement wavelengths of the aerosol extinction (354.7 nm) and backscattering (532 nm), the value $\sigma_{a,355}/\beta_{a,532}$ could be used to study the aerosol microphysical properties since it also depends on the size, shape and the refractive index of the particles. The uncertainty in $\sigma_{a,355}/\beta_{a,532}$ derived from our measured signals is smaller than that in $S_{a,532}$ because we essentially measured $\sigma_{a,355}$ and $\beta_{a,532}$. The values of $\sigma_{a,355}/\beta_{a,532}$ at the altitude range of 4-6 km on April 21 (Fig. 3.16) were between 28 and 64, whereas those at around 6.8 km on January 10 were about 12 sr (Fig. 3.17). It should be noted the value of $\sigma_{a,355}/\beta_{a,532}$ for $k=0$ is equal to $S_{a,532}$ for $k=0$.

In both the altitude regions (4-6 km on April 21 and around 6.8 km on January 10), high depolarization ratios ($\delta_a >$ 20%) and low wavelength exponent values of the aerosol backscattering coefficients ($\alpha < 0$) were observed, suggesting that large-nonspherical particles were present in both the regions. One difference between the two regions was that the relative humidities at around 6.8 km on January 10 were near saturated with respect to ice, whereas those at 4-6 km on April 21 were very low about 5%. These results suggested that ice crystals were present at around 6.8 km on January 10 and they were unlikely to be present at 4-6 km on April 21.

Table 3.3 shows the main physicochemical and optical characteristics of mineral dust (Kosa) particles and ice crystals (cirrus clouds). Both particles are generally nonspherical and larger than the laser wavelength so that high δ_a and small α values are to be expected. Nakajima et al. (1989) measured the optical properties of the yellow sand (Kosa) particles at Nagasaki (33°N, 130°E) with a polar nephelometer and calculated the scattering phase function of the particles by using the semi-empirical theory of Pollack and Cuzzi (1980). From their results shown in the figures and tables, the values of $\sigma_{a,355}/\beta_{a,532}$ for the Kosa particles were calculated to be 51-102. Takano and Liou (1989) calculated the scattering matrices of randomly oriented hexagonal ice

crystals by using a ray-tracing technique and indicated $\sigma_{a,355}/\beta_{a,532}$ ~11 sr for the cirrus clouds having a size distribution of cirrostratus model.

Our observed values at around 6.8 km on January 10, where the air was near saturated with respect to ice, were close to that of cirrus clouds calculated by Takano and Liou (1989). Ansmann et al. (1992b) measured the extinction-to-backscatter ratios of cirrus clouds with the Raman lidar and obtained the values between 5 and 15 sr at the wavelength of 308 nm. Although our measured wavelength was different from them, the data at 6.8 km on January 10 were close to their results.

The values obtained at 4-6 km on April 21 were larger than that of the cirrus clouds and partly overlapped with those of the Kosa particles. Therefore, certain kinds of mineral dust particles that have larger $\sigma_{a,355}/\beta_{a,532}$ values than that of the cirrus clouds could be discriminated by the value of $\sigma_{a,355}/\beta_{a,532}$ even if both of them would indicate high δ_a and low α values. To validate this results more precisely, it might be necessary to take account the effects of multiple scattering (e.g., Wandinger, 1998).

Fig. 3.18 shows the values of $\sigma_{a,355}/\beta_{a,532}$ as a function of the relative humidity with respect to ice (RH_{ice}) at the altitude range of 3 to 10 km observed for the period 1994 to 1997 (total 14 profiles). We excluded the data whose measurement uncertainty exceeded 50% in RH_{ice} or 20% in $\sigma_{a,355}/\beta_{a,532}$. It is found most data near ice saturation point (> 90%RH_{ice}) indicated small $\sigma_{a,355}/\beta_{a,532}$ values between 3 and 17 sr. This feature is roughly consistent with the values of the ice cirrus clouds in Table 3.3 assuming that ice crystals were predominant in the air of near ice saturation point. On the other hands, the data in unsaturated air (≤ 90%RH_{ice}) had a wide range of values between 3 and 91 sr. The fact that small $\sigma_{a,355}/\beta_{a,532}$ values that were comparable to that of the cirrus clouds were observed in unsaturated air suggests that it is impossible to discriminate the cirrus clouds and the other aerosol particles based on the $\sigma_{a,355}/\beta_{a,532}$ value alone. More detailed analysis is necessary to asses the capability of the discrimination of clouds and the other aerosols based on the Raman lidar data; one

candidate for this study is the discriminant analysis of the aerosol optical parameters (R, δ_a, α, and $\sigma_{a,355}/\beta_{a,532}$) and the relative humidity (e.g., Kwon et al., 1997).

Table 3.3 Physical and chemical characteristics and the optical properties of the dust particles and cirrus clouds particles

Species	Main Substance	Size (μm)	Shape	Refractive index (532 nm)	δ_a(%)	α	$\sigma_{a,355}/\beta_{a,532}$ (sr)	Ref.
Dust (Kosa)	Mineral	0.1~10	Nonspherical (aspect ratio~0.6)	1.55 +0~0.01i	~24*	-0.6~ -0.1	51~102	a
Cirrus (Cs)	Ice	>10	Nonspherical (hexagonal column)	1.31 $+1\times10^{-9}$i[c]	~33**	—	~11	b

[a]Nakajima et al. (1989) [b]Takano and Liou (1989) [c]Warren (1984)
*Scattering angle at 170° at λ=632.8 nm
**For particle L/2a=32 μm/80 μm with scattering angle of 180° at λ=550 nm

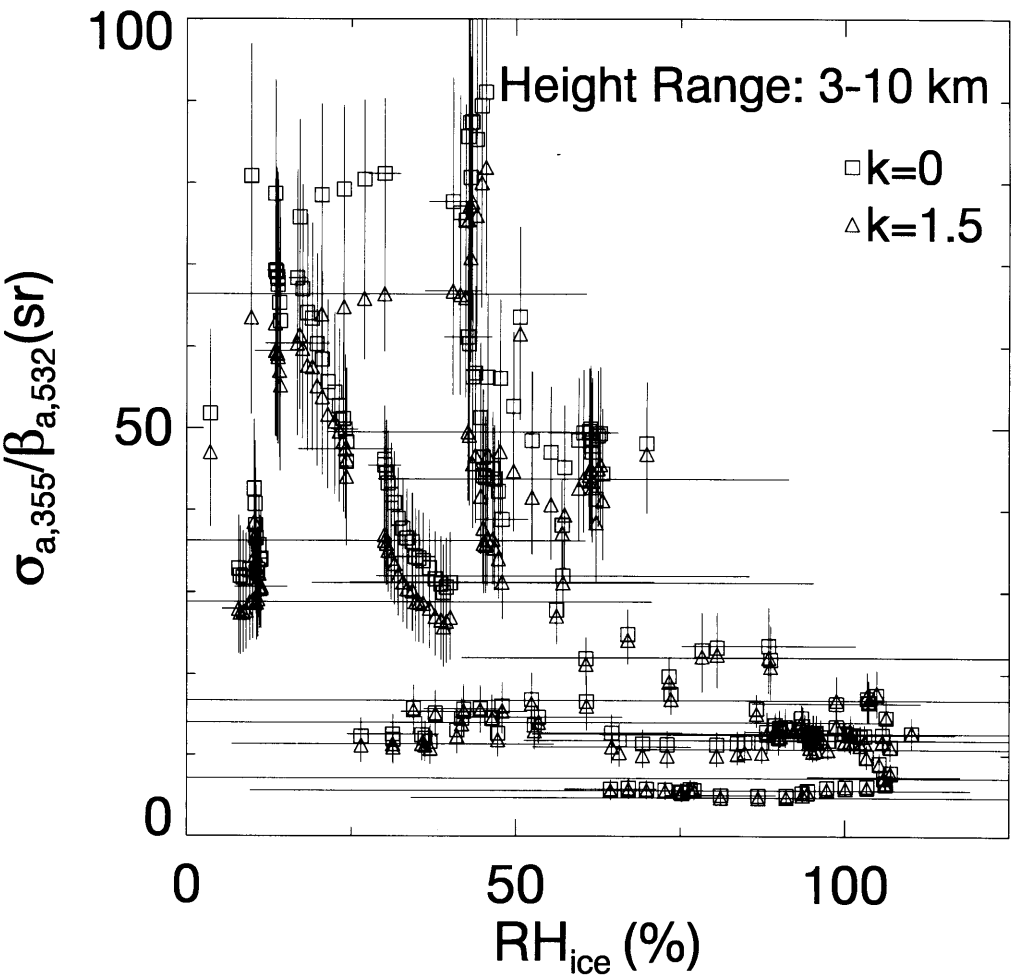

Figure 3.18 Scatter diagram of relative humidity with respect to ice (RH_{ice}) versus extinction-to-backscatter ratio ($\sigma_{a,355}/\beta_{a,532}$) between altitudes of 3 and 10 km observed for the period March 1994 to February 1997 (total 14 profiles). Open squares indicate the values calculated with k=0 and triangles indicate the values calculated with k=1.5.

3.2.5 Combined analyzing procedure for the Raman and Mie/Rayleigh signals

Data analyzing procedure for the Raman and Mie/Rayleigh backscatter signals to calculate aerosol extinction and backscattering coefficients has been developed by several authors (Ansmann et al., 1992a,b; Whiteman et al., 1992). One problem in their calculations was that the wavelength exponent of aerosol extinction coefficient (k) was assumed to remian constant (e.g., $k=1$) over a height range of the measurement. This assumption sometimes makes erroneous results because the value k varies depending on the aerosol properties such as shape, refractive index, and size distribution (e.g., Ångström, 1964; Tanaka et al., 1989). This assumption is particularly serious for our lidar data because of the relatively large difference in the measurement wavelength of Raman oxygen and Mie/Rayleigh signals. Thus we have developed the analyzing procedure for the lidar signals in which the values of k are altitude-dependent; the values are determined from the wavelength dependence of the aerosol backscattering coefficient (α) that is given by

$$\alpha(z) = -ln\left(\frac{\beta_{a,1064}(z)}{\beta_{a,532}(z)}\right) \Big/ ln\left(\frac{1064}{532}\right). \tag{3-39}$$

This parameter is simultaneously obtained from our lidar data. The value of α also depends on the shape, refractive index, and size distribution of the aerosol particles. We calculated the relationship between α and k for the tropospheric aerosol models assuming the aerosol properties as follows:

(1) Spherical particles that have unimodal lognormal size distributions. The geometric mean radius (r_g) ranges from 0.05 to 5 μm and the geometric standard deviation (σ_g) ranges from 1.5 to 2.5.

(2) Prolate and oblate spheroids (aspect ratio 1.7) particles that have the modified power law distribution. The effective radius (r_{eff}) is 1.163 μm and the effective

variance (v_{eff}) is 0.168 for equal-surface-area sphere, which are typical values for the accumulation mode of dustlike aerosols (Mischenko et al., 1997).

The refractive index of the particles was assumed to be 1.53+0.008i and 1.53+0i that are considered to be typical values for the tropospheric aerosol particles (Kent et al., 1983). We calculated the values of α and k by using the Mie theory (Bohren and Huffman, 1983) for the model (1) and by using the T-matrix method (Mischenko et al., 1996) for the model (2). The results of the calculations are shown in Fig 3.19. It is found that the values of k for the model (1) approach zero as r_g increases and α becomes less than unity for each three wavelengths (375.4, 532, and 1064 nm). The condition of $\alpha \leq 1$ corresponds to the size distributions of $r_g \geq 0.3$ μm at $\sigma_g = 1.8$ for the refractive index n=1.53+0.008i. The feature $k \sim 0$ for the large particle size distributions is due to the fact that the extinction efficiency approaches the limiting value (~2 for the weak- or non-absorbing particles) as the particle size becomes larger than the incident wavelength and consequently the extinction coefficient becomes independent of the wavelength. This feature of the relation between α and k is also satisfied for the prolate and oblate particles as shown in Fig. 3.19. When the value of α is greater than unity, the values of k vary between the range of -0.3–2.4, -0.4–2.8, and -0.27–3.2 for the wavelengths of 375.4, 532 and 1064 nm, respectively.

Based on these calculations for the tropospheric aerosol models, we assumed the value of $k(z)$ as a function of $\alpha(z)$ as follows.

$$k(z) = \begin{cases} 0 & \text{if } \alpha(z) \leq 1 \\ 1 & \text{if } \alpha(z) > 1 \end{cases} \tag{3-40}$$

The random uncertainty in $k(z)$ was assumed to be ± 0.5 for $k(z)=0$ and ± 1 for $k(z)=1$. By using the values $k(z)$ obtained from Eq. (3-40), we calculated the aerosol extinction coefficient by Eq. (3-25) and the backscattering ratio by Eqs. (3-28) and (3-

31). It should be noted these two parameters (α and k) must be calculated by an iterative manner as described below.

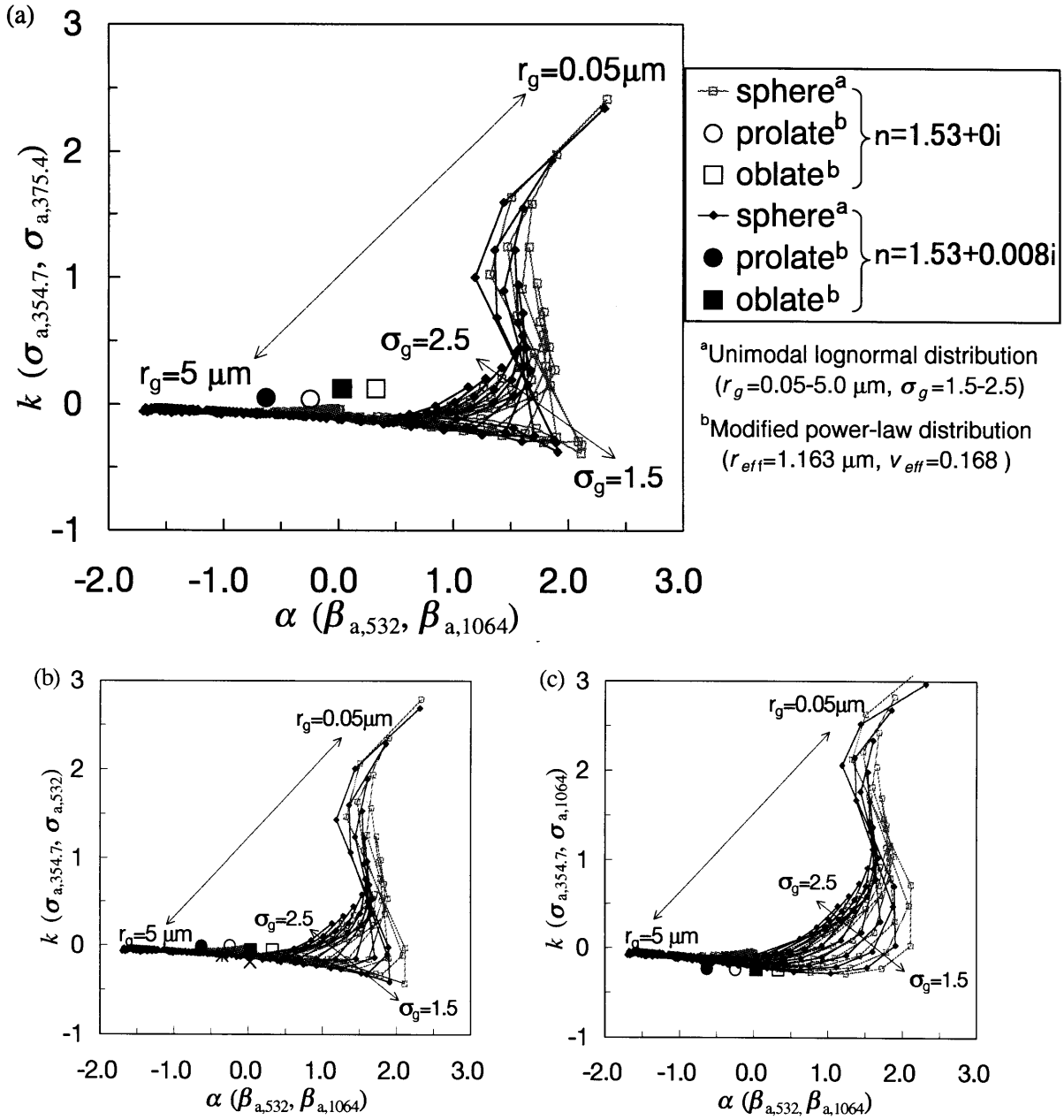

Figure 3.19 Relationship between the wavelength exponent of aerosol backscattering coefficient (α) between 532 and 1064 nm and the wavelength exponent of the extinction coefficient (k) between 354.7 nm and (a) 375.4 nm, (b) 532 nm, and (c) 1064 nm for the aerosol models. Solid and thin lines with squares show the values for the spherical particles with unimodal lognormal size distributions. Large circles and squares show the values for the prolate and oblate (aspect ratio is 1.7) particles with modified power-law distribution, respectively. The refractive index is 1.53+0i for the open symbols and 1.53+0.008i for the filled symbols. Details are described in the text.

The procedure for calculating the backscattering ratio, aerosol backscattering coefficient, and the aerosol extinction coefficient used in this study is shown schematically in Fig. 3.20. We calculated these parameters by following manner.

(1) At first, the backscattering ratios $R(z)$ and the aerosol backscattering coefficients $\beta_a(z)$ at 532 and 1064 nm are calculated from the Mie/Rayleigh signals by Eqs. (3-28) and (3-29) without taking account of the aerosol extinction.

(2) $\alpha(z)$ is calculated from $\beta_{a,532}(z)$ and $\beta_{a,1064}(z)$ by Eq. (3-39).

(3) $k(z)$ is determined from $\alpha(z)$ by Eq. (3-40).

(4) The aerosol extinction coefficient $\sigma_{a,355}(z)$ is calculated from the Raman oxygen signal by Eq. (3-25) using the $k(z)$ that is determined in (3).

(5) $\sigma_a(z)$ at 532 and 1064 nm are calculated from $\sigma_{a,355}(z)$ by Eq. (3-31). If the measurement uncertainty in $\sigma_{a,355}(z)$ exceeds 100%, they are calculated from $\beta_{a,532}(z)$ and $\beta_{a,1064}(z)$ by Eq. (3-32) assuming that $S_{a,532}$=50 with random uncertainty of ±40 and $S_{a,1064}$ = 40 with random uncertainty of ±32.

(6) $R(z)$ and $\beta_a(z)$ at 532 and 1064 nm are calculated by Eqs. (3-28) and (3-29) by using the aerosol extinction coefficient $\sigma_a(z)$ obtained in (5).

(7) (2)-(6) are calculated in an iterative manner (ten times of iteration are sufficient for the convergence of values).

The values of S_a and the uncertainty δS_a in (5) are determined based on the results shown in Figs. 3.15 and 3.16 and the measurements by Takamura et al. (1994). For the derivation of the water vapor mixing ratio (Eq. 3-4), the aerosol extinction coefficients at the Raman water vapor and oxygen wavelengths are calculated from $\sigma_{a,532}(z)$ and $k(z)$ using the relation same as Eq. (3-23).

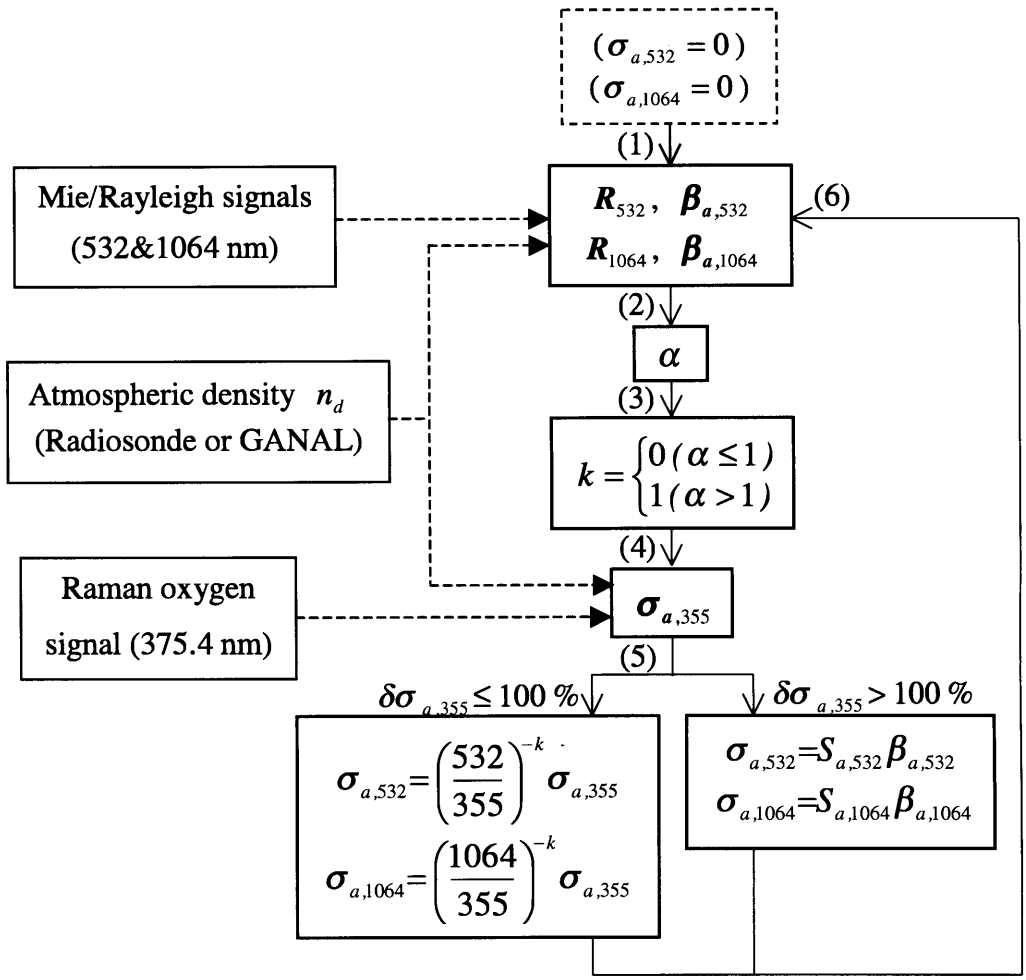

Fig. 3.20 Data analyzing procedure for calculating the backscattering ratios (R), aerosol backscattering coefficients (β_a), and the aerosol extinction coefficients (σ_a) from the Raman lidar signals used in this study.

There is three different points in this analyzing procedure from those of Ansmann et al. (1992a,b) and Whiteman et al. (1992): (a) we used the altitude dependent value of $k(z)$ as a function of $\alpha(z)$ (Eq. 3-40) while they used a fixed value (e.g., $k = 1$), (b) we employed two methods (Eqs. 3-31 or 3-32) to estimate the aerosol extinction at the Mie/Rayleigh wavelengths depending on the measurement uncertainties in $\sigma_{a,355}(z)$ while they used Eq. 3-31, and (c) we used the atmospheric density data obtained with the radiosonde or GANAL (or GAPLX) to account for the molecular backscattering in the calculation of $R(z)$ (Eq. 3-28) while they used Raman nitrogen signal to account for it. All of these refinements were made to improve the accuracy of the analyzed data.

To check the validity of this analyzing procedure, Fig. 3.21 shows the vertical profile of the backscattering ratio at 532 nm on November 28, 1994 calculated by employing this procedure. Also shown is the profile calculated from the Mie/Rayleigh signal at 532 nm alone using a constant $S_{a,532}$ value of 50. The backscattering ratios for both the profiles were normalized at 9.9 km by fitting to the stratospheric profiles observed 3 hours later. Large backscattering ratios (~10) were observed at 6.5-8.0 km, where cirrus clouds were probably present since δ_a~20% and RH was near saturated with respect to ice in the region (not shown). The backscattering ratios calculated by the procedure described above showed realistic values ($R > 1$) below the clouds at 6.5-8.0 km, whereas those calculated by assuming constant $S_{a,532}$ value showed unrealistic values ($R < 1$) below 6.5 km. This is due to the fact that the cirrus clouds at 6.5-8.0 km had smaller $S_{a,532}$ values than 50. This result is consistent with the model calculations for the cirrus clouds (Table 3.3) and the observations (e.g., Fig. 3.18).

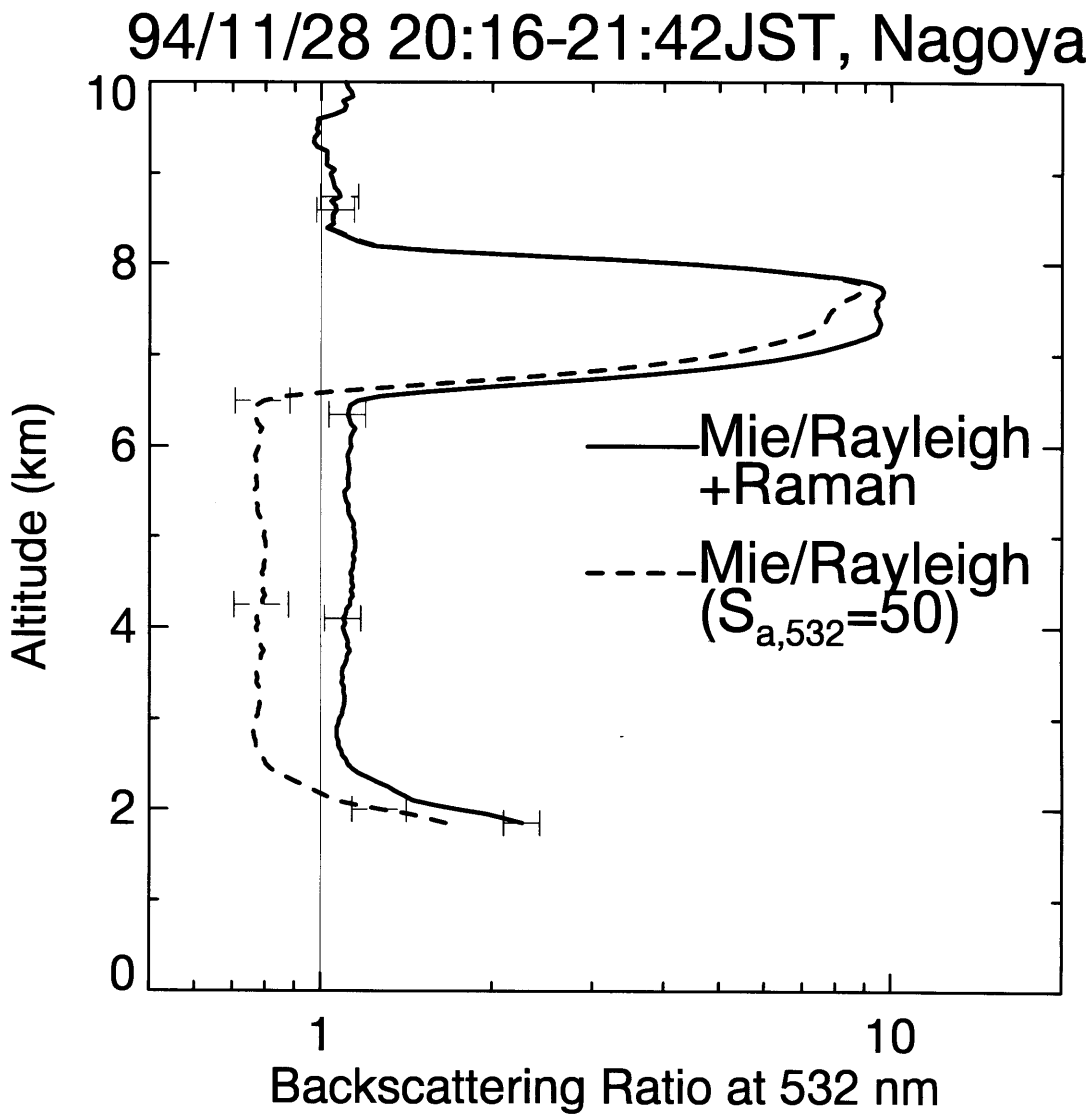

Figure 3.21 Vertical profiles of backscattering ratio at 532 nm observed on November 28, 1994. The solid line shows the profile calculated by combining the Raman oxygen and Mie/Rayleigh signals and the dashed line shows the profile calculated assuming constant extinction-to-backscatter ratio $S_{a,532}$ of 50. The data analyzing procedure is described in the text.

3.2.6 Depolarization ratio

The total (aerosol + molecule) depolarization ratio (δ) is obtained from the linear polarization components of the backscatter signals with respect to the polarization plane of the emitted laser, which is defined as

$$\delta(z) \equiv \frac{\beta_{a,\perp}(z)+\beta_{m,\perp}(z)}{\beta_{a,//}(z)+\beta_{m,//}(z)+\beta_{a,\perp}(z)+\beta_{m,\perp}(z)} \times 100 = \frac{gP_{\perp}(z)}{P_{//}(z)+gP_{\perp}(z)} \times 100 \ [\%] \quad (3\text{-}41)$$

where the subscripts // and $\perp$ refer to the parallel and perpendicular components with respect to the polarization plane of the emitted laser, g is the signal gain ratio between the two polarization channels ($=K_{//}/K_{\perp}$), and the subscripts a and m refer to the components of aerosol particles and air molecules, respectively. The measurement wavelength was 532 nm in this study.

The aerosol depolarization ratio (δ_a) is calculated from the total depolarization ratio δ and the backscattering ratio R, which is expressed by

$$\delta_a(z) \equiv \frac{\beta_{a,\perp}(z)}{\beta_{a,//}(z)+\beta_{a,\perp}(z)} = \frac{\delta(z)R(z)-\delta_m}{R(z)-1} \ [\%], \quad (3\text{-}42)$$

where δ_m is the depolarization ratio of air molecules at the wavelength and bandwidth of the measurement. The value of δ_m is calculated to be 0.49% (private communication, Adachi) for the interference filter utilized in this study (center wavelength=532 nm with FWHM=1.17 nm) for the tropospheric temperature and pressure ranges. Additionally, we employed the correction procedure developed by Adachi et al. (1998) to subtract the depolarization components produced by the system ($\delta(z) \cong \delta_{observed}(z)-\delta_{system}$). The depolarization component produced by the system δ_{system} can be obtained from the observed data at an altitude where $R(z)=1$ or where $\delta_a(z)=0$ by

$\delta_{system} = \delta_{observed}(z) - \delta_m / R(z)$. The former condition can be satisfied at the height above the stratospheric aerosol layer ($z \geq 28$ km) or at around the tropopause (10-15 km). The latter condition can be satisfied in the height region of the stratospheric aerosol layer (approximately 15-28 km) where the aerosol particles are considered to primarily consist of spherical particles (sulfuric acid solution droplets) in the midlatitude region.

The value of δ_a can be considered an indicator of the particle nonsphericity (e.g., Bohren and Huffman, 1983): for homogeneous spherical particles δ_a is zero according to the Mie theory; for nonspherical particles δ_a substantially deviates from zero.

Measurement uncertainty in depolarization ratios

The measurement uncertainty in δ can be calculated by

$$\delta\delta(z) = \frac{1}{(P_{//}(z) + gP_{\perp}(z))^2}[(gP_{\perp}(z))^2(\delta P_{//}(z))^2 + (gP_{//}(z))^2(\delta P_{\perp}(z))^2 + (P_{//}(z)P_{\perp}(z))^2(\delta g/g)^2]^{\frac{1}{2}}, \quad (3\text{-}43)$$

and the uncertainty in δ_a is given by

$$\delta\delta_a(z) = \left[\frac{(\delta_m - \delta(z))^2}{(R(z)-1)^4}(\delta R(z))^2 + \left(\frac{R(z)}{R(z)-1}\right)^2(\delta\delta(z))^2\right]^{\frac{1}{2}}. \quad (3\text{-}44)$$

4 Results and Discussions

This section presents the results of the observations carried out for the period March 1994 to February 1997. We show the temporal and vertical variations of the aerosol optical properties in the free troposphere between the altitude range of 1-8 km. We analyzed the relation of these aerosol properties to the ambient relative humidity and the transport pathways of the air parcels from the source areas in order to estimate the aerosol constituents observed with the lidar. The first subsection (Section 4.1) presents a typical case of the observation on April 17, 1994, in which significant temporal variations of the aerosol parameters (the backscattering ratio and the depolarization ratio) and the humidity were found during 30 minutes. The following subsection (Section 4.2) presents the seasonal characteristics of the aerosol properties, i.e., vertical distributions of the backscattering ratio and the depolarization ratio, vertically integrated aerosol backscattering coefficient, and the depolarization ratio as a function of the relative humidity. The contribution of the aerosol sources (the Asian Continent and the Pacific Ocean) on the lidar data was evaluated on the basis of a simple transport model by using a global meteorological analysis data.

4.1 Temporal and vertical variation in backscattering ratio, depolarization ratio, and humidity during 30 minutes

4.1.1 Results on April 17, 1994

Figure 4.1 shows the vertical profiles of water vapor mixing ratio (w), backscattering ratio at 532 nm (R), total depolarization ratio at 532 nm (δ), and relative humidity over water (RH) observed on April 17, 1994. Six successive profiles were obtained by accumulating the data for every 5 minutes during the 30 minutes of the observation (19:18-19:48 JST). The vertical resolutions of w, RH, and δ were 150 m and that of R was 450 m. Relative humidity was calculated by combining the water vapor mixing ratio obtained with the Raman lidar and atmospheric temperature

and pressure obtained with the radiosonde launched at Hamamatsu meteorological observatory (90 km southeast of lidar site) at 21:00 JST on the same night. The relative humidity measured with the radiosonde at Hamamatsu is also shown in Fig. 4.1c. In the calculation of the backscattering ratio, data normalization was performed at about 10 km in connection with the stratospheric profile observed about 10 minutes later. During the observation period, the lidar site was under a high pressure zone after a weak cold front passed its north side.

Temporal variations of aerosol properties and humidity and their relation

Temporal changes of the humidity and aerosol parameters were observed at the altitude range of 1.0-2.2 km (Region A in Fig. 4.1), where w (also RH) and R were increasing and δ was decreasing for the 30 min. The temporal relationships between RH and the values of R and δ in this region are shown in Figure 4.2. It is found that the values of R were positively correlated with RH (Fig. 4.2a) and those of δ were negatively correlated with RH (Fig.4.2b) at each altitude inn Region A, indicating that the total volume aerosol backscattering cross section was larger and the particles were more spherical in the moist air than in the dry air in this region. The RH values in this region varied between 13 and 38%.

While the aerosol parameters and the humidity in Region A showed significant temporal variations, the parameters above this region showed little temporal variations. At the altitude range of 2.2-3.5 km (Region B in Fig. 4.1), the depolarization ratios were almost constant and indicated relatively high values about 11% (Fig. 4.1c). The RH values in this region indicated relatively high values about 35% (Fig. 4.1d), which were close to the maximum value in Region A. The relation between the depolarization ratio and the RH values in terms of hygroscopic properties of aerosol particles is discussed in Section 4.1.2.

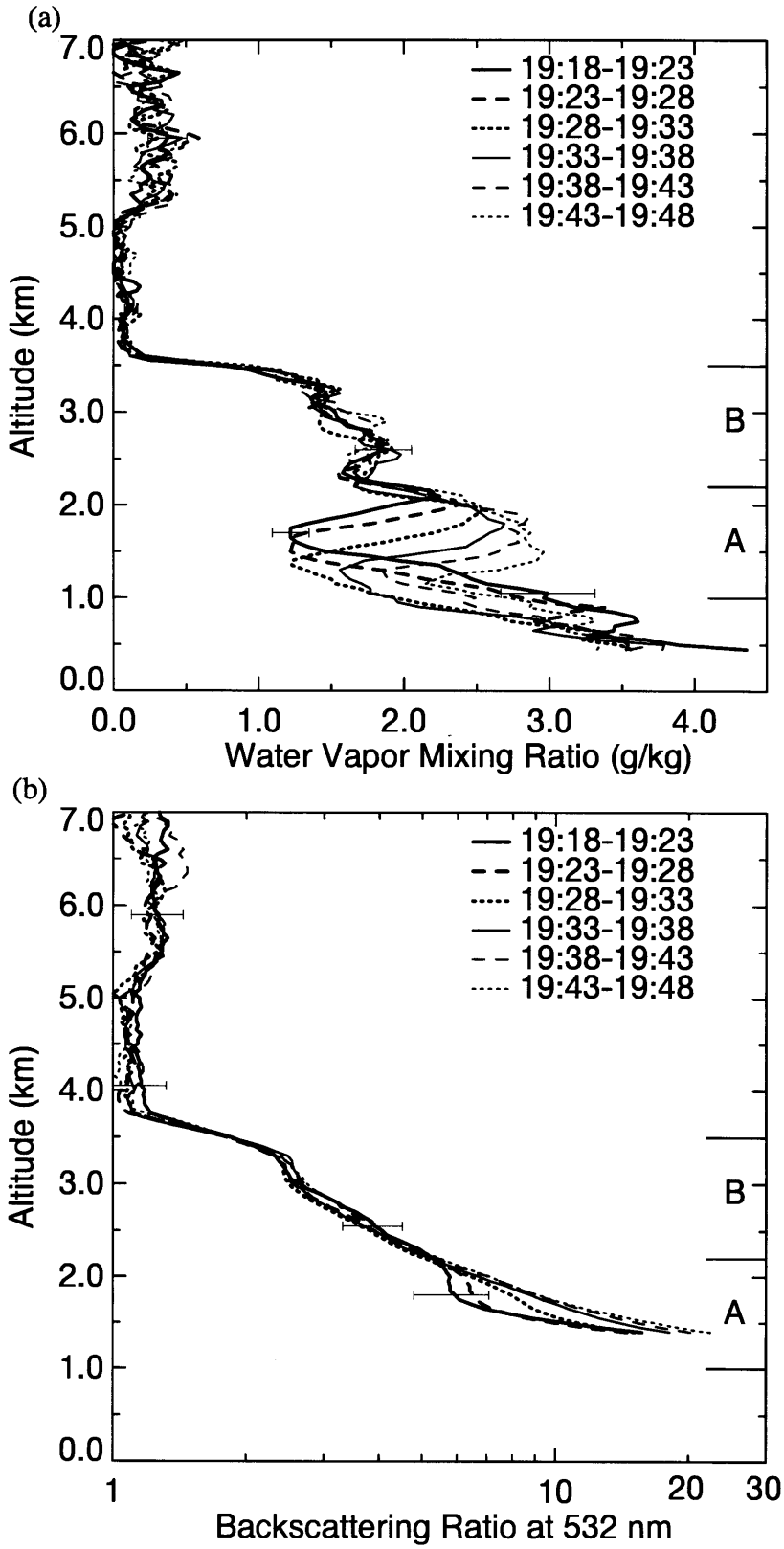

Fig. 4.1 Vertical profiles of (a) water vapor mixing ratio, (b) backscattering ratio at 532 nm, (c) total depolarization ratio at 532 nm and (d) relative humidity over water observed with the Raman lidar from 19:18 to 19:48 JST on April 17, 1994.

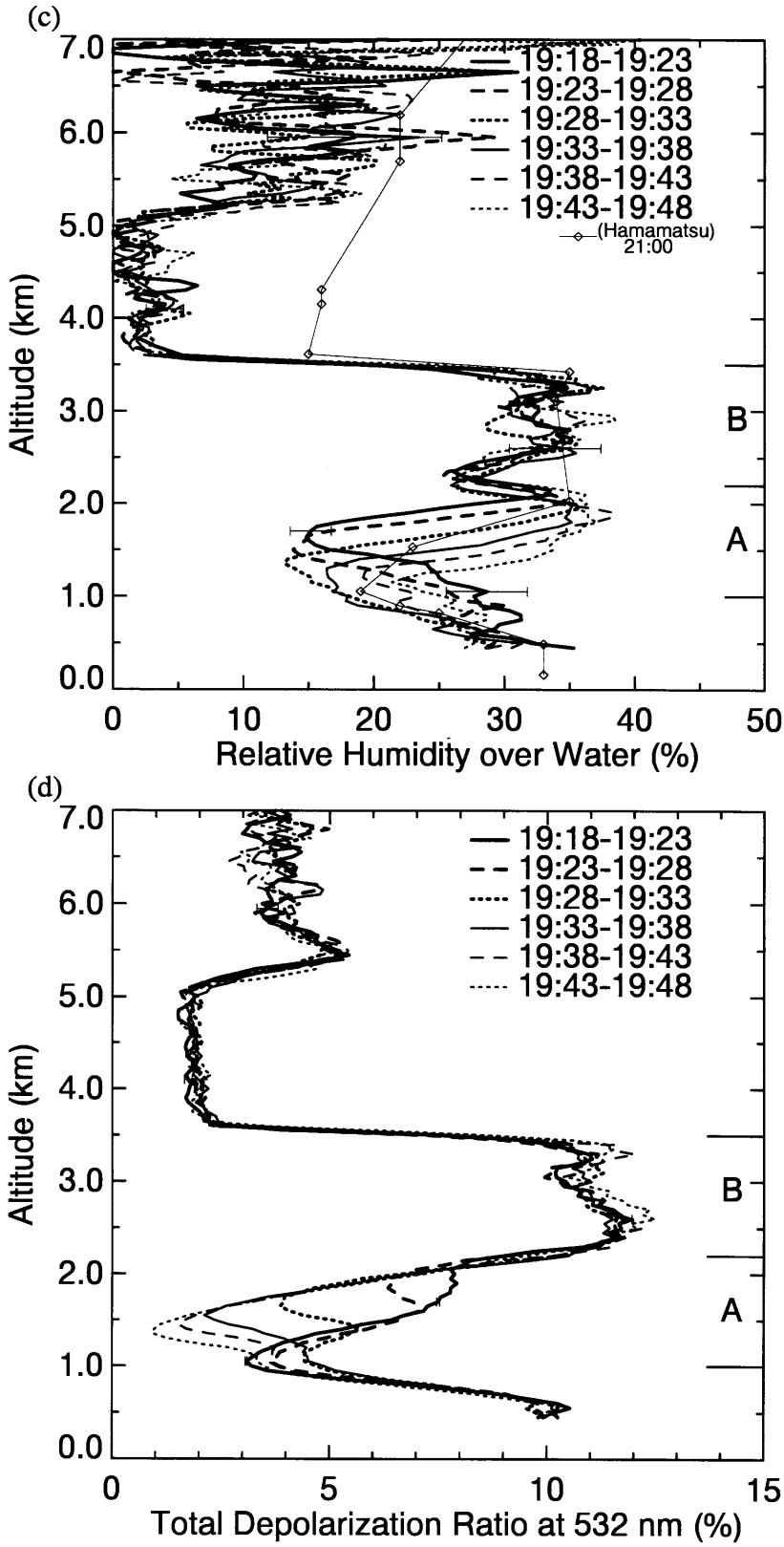

Fig. 4.1 Continued.

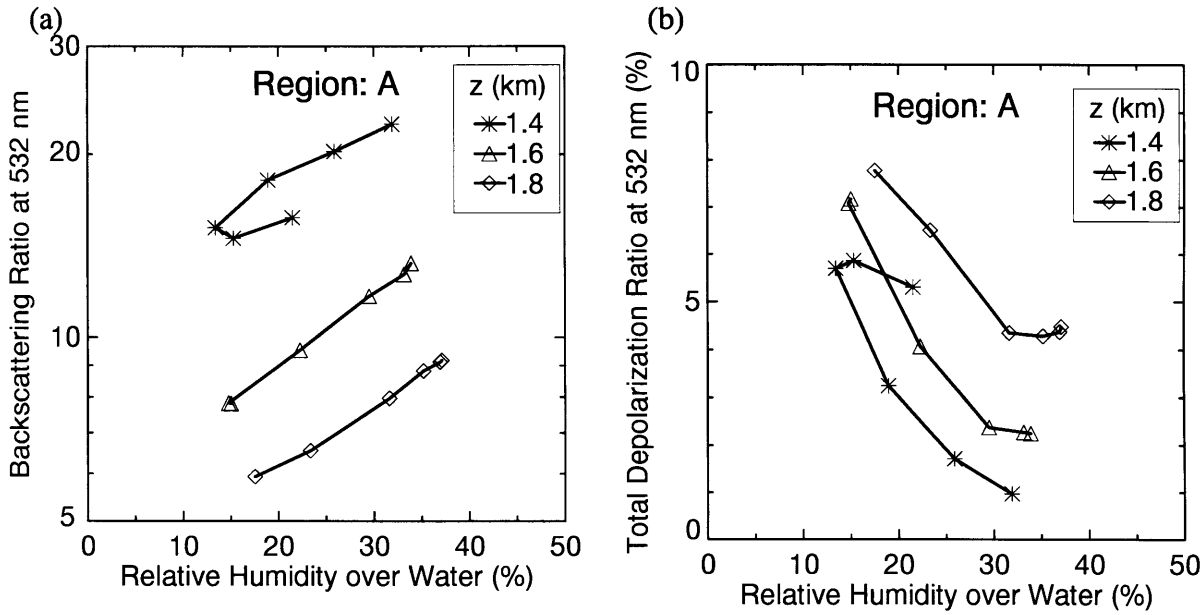

Fig. 4.2 Temporal variations of (a) backscattering ratio and (b) total depolarization ratio as a function of the relative humidity at the altitudes of 1.4, 1.6, and 1.8 km (Region A in Fig. 4.1).

Vertical relationship of aerosol properties and humidity

Figure. 4.3 shows the vertical relationship of w and the quantities R and δ at the altitude range of 1-7 km. The values of R were positively correlated with w vertically over the height range (Fig. 4.3a). On the other hand, the values of δ were positively correlated with w above 2.2 km and negatively correlated below this height level (Fig. 4.3b). This height of boundary corresponded to the boundary of Regions A and B. Different atmospheric processes would be responsible for these vertical relationships between the humidity and the aerosol parameters observed by the lidar.

Temperature and wind profiles at Hamamatsu are shown in Fig. 4.4. The wind direction changed for about 15 degrees at boundary of Regions A and B (2.2 km). The altitudes of the wind shears at 1.0 km and 5.0 km and the temperature inversion at 3.5 km corresponded to the vertical discontinuities of the water vapor and aerosol profiles found in Figs. 4.1. These correspondences suggested that the vertical distributions of both water vapor and aerosols would be greatly affected by the horizontal transport process in this case.

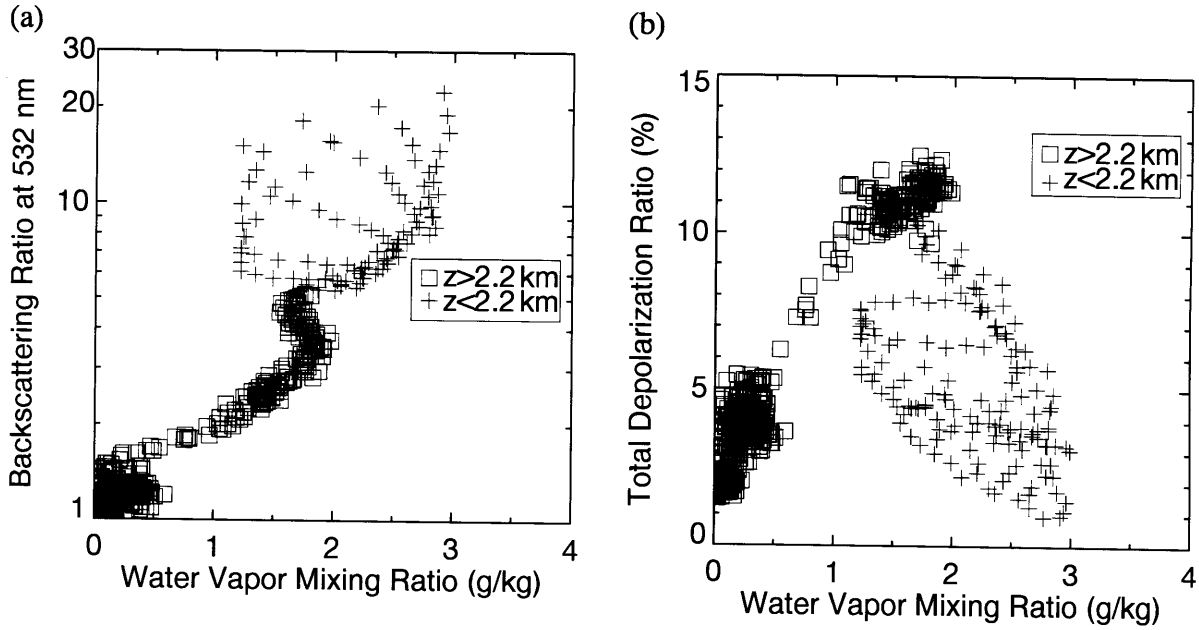

Fig. 4.3 Vertical relationship of the water vapor mixing ratio and the quantities (a) backscattering ratio, and (b) total depolarization ratio between 1 and 7 km (+: $z < 2.2$ km, □: $z > 2.2$ km).

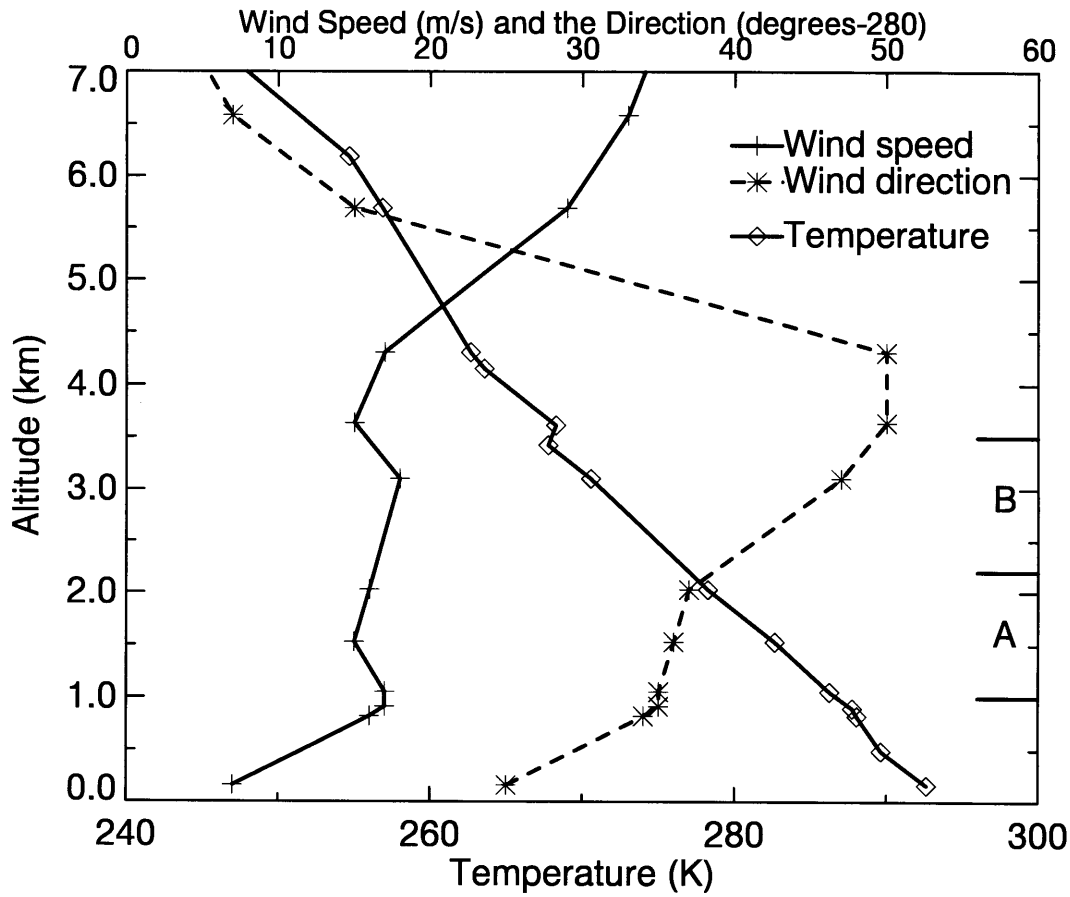

Fig. 4.4 Vertical profiles of temperature, wind speed and wind direction at Hamamatsu (35°N, 138°E) at 21:00 JST on April 17, 1994.

4.1.2 Discussion

Since the depolarization ratio of aerosol particles can be considered as a measure of particle nonsphericity, the value depends on the phase of the particles: liquid particles are almost spherical by existing as droplets and indicate near-zero depolarization ratio, whereas solid particles are generally nonspherical by existing as crystals and indicate the ratio substantially grater than zero. If air contained hygroscopic particles that have properties of deliquescence and/or efflorescence, the value of δ changes depending on the ambient RH because the phase of hygroscopic particles depends on the RH as well as its history (Orr et al., 1958; Hänel, 1976; Tang, 1996). For example, relative humidities at the phase transition points of major hygroscopic particles are as follows: 75.3%RH for deliquescence (DRH) and 46-48%RH for crystallization (CRH) of NaCl particle; 80% and 37-40% for those of $(NH_4)_2SO_4$, and 40% and 22-0.05% for those of NH_4HSO_4 at 298 K (Tang, 1996). The values of DRH and CRH for the other chemical composition are shown in Table 4.1 (The relation between the aerosol chemical composition and the depolarization ratio as a function of the RH is further discussed in Section 4.2.5).

The values of RH in Region A, where the δ were negatively correlated with RH, ranged between 13 and 38%. These RH values are close to the crystallization point of NaCl and $(NH_4)_2SO_4$, and both the deliquescence and crystallization humidities of NH_4HSO_4. Thus, the observed negative correlation between δ and RH at Region A might be due to the phase transformation of these hygroscopic particles.

A similar negative correlation between RH and δ was observed by Murayama et al. (1996) in the atmospheric boundary layer in Tokyo. They made hourly observations during both day and night in February 1994, and showed the value of δ at around the altitude of 100 m was negatively correlated with the RH at 30 m. The value of δ changed between 2% and 7% when RH changed between 65% and 20% during their measurements. They reported this negative correlation was generally found independent of season. Our results in Region A showed that the negative correlation between δ and

RH extended vertically for about one kilometer in the lower troposphere (Fig. 4.1), and the values of R were also correlated with RH in this region. A similar measurement location (urban area near the bay) and the aerosol constituents in the lower troposphere might result in a similar negative correlation between δ and RH.

The fact that Region B indicated high δ values (~11%) where the RH values were close to the maximum value in Region A (~35%RH) suggested that Region B contained the aerosol particles consisting of different chemical composition and/or phase from Region A. As shown in Fig. 4.3, the wind direction at Region B (3.0 km) differed by about 15 degrees from those at Region A (1.0-2.0 km), suggesting that the two altitude regions had been controlled by different transport regime from the source areas.

To examine the transport pathways of the air parcels at the two altitude regions, we calculated the 5-day isentropic backward trajectories arrived over the lidar site at the observation period (Figure 4.4). We calculated twenty-five trajectories from the altitudes 1.5 km for Region A and 3.0 km for Region B whose initial position was located at around the lidar site (35.1°N, 137.0° E) with horizontal interval of 0.5° on the same isentropic surface. Detail of the calculation procedure is described in Appendix B. It is found that both the air parcels arrived at Regions A and B were transported from over the Asian Continent driven by westerly (upper panel in Fig 4.4). They had passed in the lower troposphere and most of them had passed near the boundary atmosphere at around 110°E before the 3 days of the measurement (middle panel in Fig. 4.4). It is also found that the air parcels at Region A had passed over the ocean more frequently than those arrived at Region B, suggesting that the air parcels at Region A had been affected by the maritime source which emits water-soluble substances (e.g., sea-salt and non-sea-salt sulfate) and relatively large amount of water vapor.

Based on the trajectories, two processes can be proposed to account for the observed difference in the relation between the aerosol parameters and RH at Regions A and B. One process is that the major chemical composition of aerosol particles was

different between the two regions; the aerosol particles in Region A predominantly consisted of water-soluble particles originated from the ocean whose deliquescence (or efflorescence) point was between 13 and 38%RH, whereas those in Region B mainly consisted of water-insoluble particles or water-soluble particles originated from the continent whose phase transformation point was higher than 35%. The other process is that the RH history of air parcels caused hysteresis of the phase of deliquescent particles depending on the height region even though both regions contained the same aerosol constituents; the air parcels arrived at Region A had experienced high humidity (> DRH) over the ocean and the particles in it had deliquesced into solution droplets and some fraction of them crystallized at CRH, whereas those at Region B had once experienced low RH (< CRH) and the particles had crystallized, and after then the RH never exceeded DRH. To examine the latter process, we investigated the RH history of the air parcels during the transportation by using humidity data of GANAL (lower panel in Fig. 4.4). However, any significant relation between the RH history and the observed feature was found. This might be due to the coarse temporal and spatial resolution of the GANAL data. For this reason, it is difficult to distinguish which process is plausible to account for the observed characteristics based on our limited data. Moreover, a local motion of air (e.g., sea breeze circulation) whose temporal and spatial scale was smaller than the grid of GANAL data might caused the temporal variations of the aerosol constituents and the humidity in Region A; dry air with nonspherical particles were partially mixed with moist air with low depolarizing particles in this region.

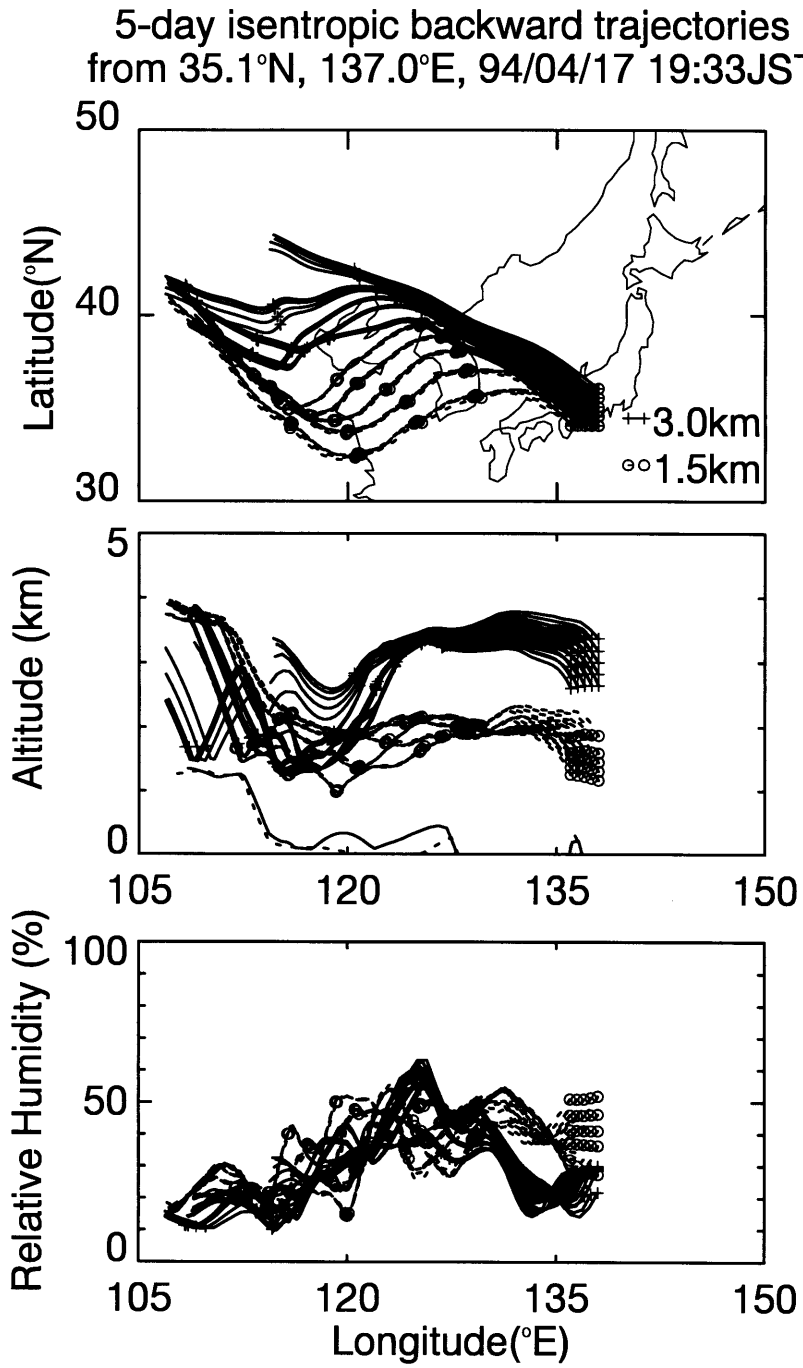

Fig. 4.4 Horizontal (upper panel) and vertical (middle panel) cross sections of 5-day isentropic backward trajectories arriving at the altitude of 1.5 km (dotted line with circles) and 3.0 km (solid line with pluses) over the lidar site on April 17, 1994. The symbols are plotted with 24-hour interval. The lowermost lines in the vertical cross section (middle panel) show the land elevation. The lower panel shows the relative humidity history of the air parcels during the transportation.

4.2 Seasonal variation in aerosol backscattering, depolarization ratio, and humidity

In this section we present the seasonal and altitude characteristics of the aerosol optical properties between altitudes of 2 and 8 km on the basis of the measurements for the period March 1994 to February 1997. For this purpose, we calculated the aerosol parameters and the humidity from the lidar signals accumulated for 30-60 minutes in each profile to improve the signal-to-noise ratio. The signals were smoothed to a vertical resolution of 350 m (330 m after April 1996) by taking running mean. Thus, the derived parameters indicate the average for this period and height range. The influence of taking average for time (30-60 minutes) on the derived parameters is expected to be small because most of the data taken for this period showed little temporal variations; the occurrence of relatively large temporal variations of the parameter during the observation as found at 1.0-2.2 km in April 17, 1994 (Fig. 4.1) was less than ten per year in our observations except for case of the presence of clouds (we excluded the data of which the relative humidity was saturated with respect to water or ice). We analyzed the relation of the observed aerosol properties to the relative humidity and the transport pathways of the air parcels from the source areas to estimate the aerosol constituents. We also attempt to estimate the contribution of aerosol sources (the Asian Continent and the Pacific Ocean) on the lidar data based on a simplified transport model.

4.2.1 Vertical profiles of backscattering ratio, aerosol depolarization ratio, and humidity

The four vertical profiles shown in Fig. 4.5 represent the seasonal characteristics of the aerosol optical properties and the humidity measured with the Raman lidar on April 21, July 23, September 11, and December 23 in 1994. The relative humidity and temperature profiles obtained with the coincident radiosonde (launched 30 m away from the lidar at 22:31 JST on September 10) are also shown in Fig. 4.5c. The 5-day isentropic backward trajectories corresponding to these vertical profiles at the altitudes of 3 and 6 km are shown in Fig. 4.6.

Large aerosol backscattering ratios, R, were found in the spring season (Fig. 4.5a) with peaks at 2.3 km, where R was 5.2, and between 4 and 6 km, where R was about 2.4. The aerosol depolarization ratios δ_a between 4 and 8 km were high, about 25%, indicating a substantial amount of nonspherical particles in this region. The presence of ice crystals was improbable since the relative humidities were less than 20% with respect to ice in this region. The backward trajectories (Fig. 4.6a) indicated that the air parcels had carried over the Asian Continent by a westerly flow. Some air parcels arrived at 6 km showed cyclonic motion at around 45°N, 75°E, which is associated with front activity. In this area, from eight to 32 occurrences of dust rises were reported in the spring of 1994 (Chun, 1996).

Figure 4.5b shows the profiles observed in the summer when Pacific high-pressure covered the northwestern Pacific region. The values of R were small (average was 1.06) and nearly constant between 2 and 10 km. The aerosol depolarization ratio indicated low values about 4%, indicating the predominance of spherical, near spherical, or small ($r < \lambda$) particles. A relatively large amount of water vapor was observed between 0.5 and 10 km and the mixing ratios approximately linearly decreased with height up to 6.5 km. The air parcels arrived at both altitudes (3 and 6 km) had passed slowly (about 7 m s^{-1}) over the Pacific Ocean (Fig. 4.6b).

The autumn profiles (Fig. 4.5c) showed steep vertical gradients of the humidity (w and RH) and aerosol depolarization ratios at 4.0 km. We measured values of δ_a less than 2% with high RH values between 70 and 90% below 4.0 km. The aerosol depolarization ratio sharply increased to 17% and the RH decreased to as low as 2% at an altitude between 3.6 and 4.0 km, where the temperature inversion was present (right-hand side of Fig. 4.5c). The backward trajectories for the two altitudes showed different pathways (Fig. 4.6c). The air parcels present at 3km had been carried over the Pacific Ocean while those arrived at 6 km had passed over the Asian Continent.

This vertical structure (sharp increase in δ_a and decrease in w (RH) with height) has been frequently observed between 2 and 4 km throughout the year except for

the summer. This structure can been seen in Fig. 4.6a at around 3.0 km, where the δ_a sharply increased from 5% to 20% and the RH decreased from 50% to 5% with height (See also Figs. 4.7c and 4.7d).

Figure 4.5d shows the profiles observed in the winter, when a strong cold front had just passed the lidar site. The average value of R was 1.1 and that of δ_a was 2% between 2 and 10 km. The relative humidity was low (< 20%RH) above 2 km. The air parcels at 3 km had been carried over the Asian Continent in the middle-upper troposphere and diverged at around 45°N, 115°E and those at 6 km had moved over the upper troposphere (6-10 km) at a mean speed of 30 $m s^{-1}$, driven by jet streams (Fig. 4.6d).

Figures 4.7-4.9 show the temporal-vertical cross sections of water vapor mixing ratio, backscattering ratio, aerosol depolarization ratio, and relative humidity over water obtained with the Raman lidar for the period March 1994 to February 1997.

The vertical distribution of water vapor mixing ratio (Figs. 4.7a, 4.8a, and 4.9a) showed strong seasonal variation; the height of lower atmospheric regions containing relatively large amount of water vapor ($\geq$ 5 g kg^{-1}), which were present below 2 km in the spring, ascended to approximately 4 km in the summer, gradually descended below 1 km in the autumn, and disappeared in the winter. Corresponding to this variation, the RH values showed similar seasonal variation (Figs 4.7d, 4.8d, and 4.9d); A humid (RH $\geq$ 70%) region was usually present up to height of ~4 km in the summer and autumn.

The backscattering ratios showed steep vertical gradients at around 2-4 km throughout the year (Figs. 4.7b, 4.8b, and 4.9b), where the R values decreased from >2 to less than 1.2 with height. Above this level, the values of R were generally less than 1.2 up to 10 km except for the spring, when they were mostly lager than 1.2. The aerosol depolarization ratios in the spring mostly showed high values (>10%) above about 2km (Figs. 4.7c, 4.8c, and 4.9c), indicating the predominant existence of nonspherical particles in this region. These high δ_a values were occasionally found in the autumn above 4 km but the occurrence varied from year to year; the occurrence was

common in 1994 and 1996 and rare in 1995. In the summer and winter the δ_a values were generally less than 5% throughout the troposphere, indicating the predominance of spherical or small particles in these regions. The values of δ_a in the moist regions in the lower altitudes (below 2 km) generally indicated low values throughout the year.

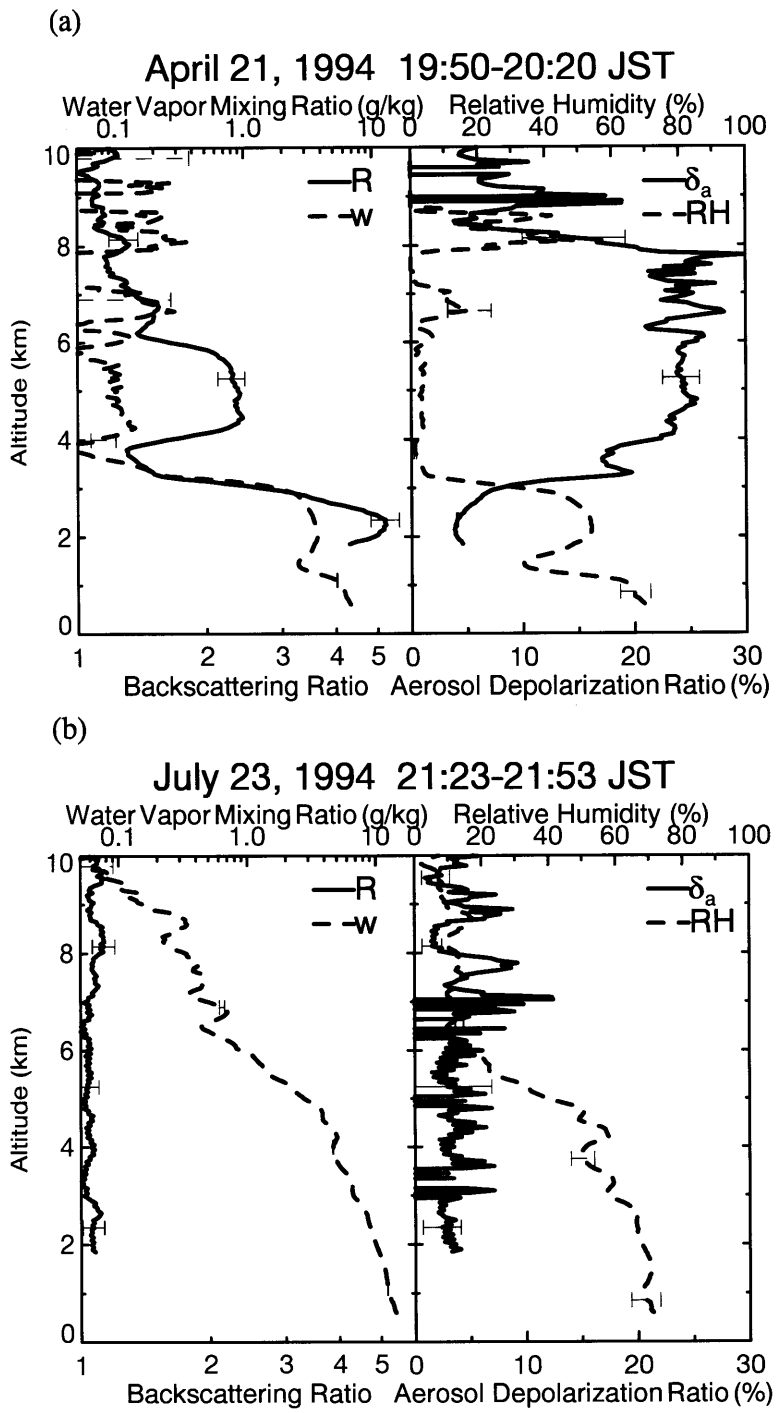

Fig. 4.5 Vertical profiles of backscattering ratio (R) and aerosol depolarization ratio (δ_a) at 532 nm, water vapor mixing ratio (w) and relative humidity (RH) obtained with the Raman lidar at Nagoya (35.1°N, 137.0°E) on (a) April 21, (b) July 23, (c) September 11, and (d) December 23 in 1994. Thin lines in Fig. 4.6c shows the temperature and humidity profiles obtained with the coincident radiosonde. Temperature scale is 200-300 K.

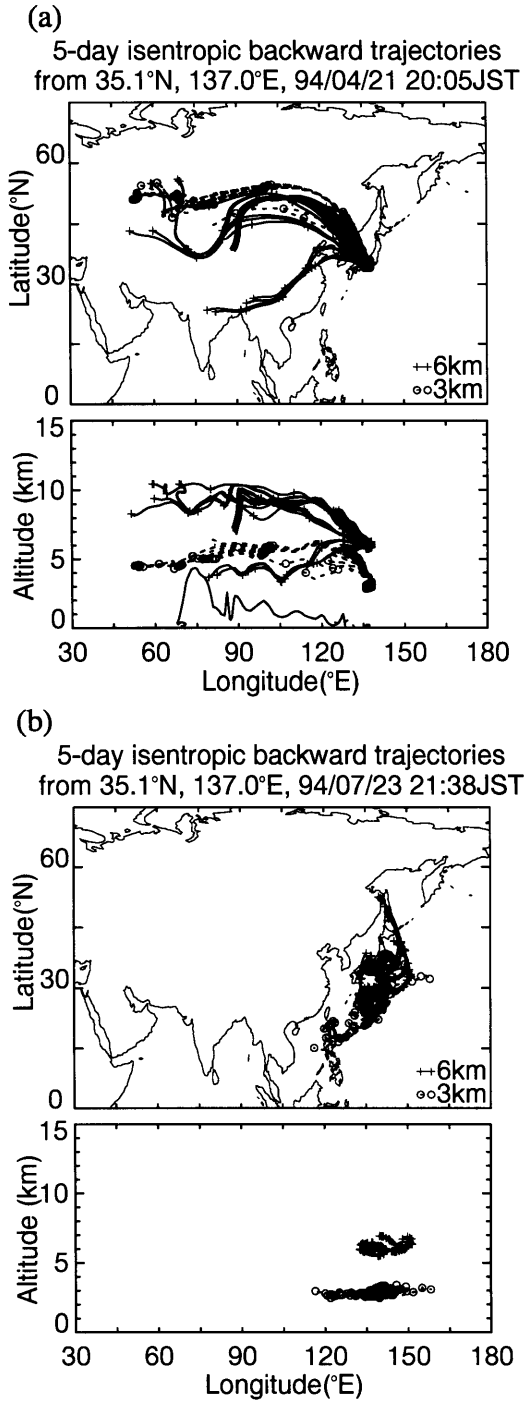

Fig. 4.6 Horizontal and vertical cross sections of isentropic backward trajectories arriving at the lidar site on (a) April 21, (b) July 23, (c) September 11, and (d) December 23 in 1994. The dashed lines with circles indicate the trajectories arrived at 3 km and solid lines with pluses indicate those arrived at 6 km. Symbols are plotted at 24-hour intervals. The lowermost lines in the vertical cross section show the land elevations.

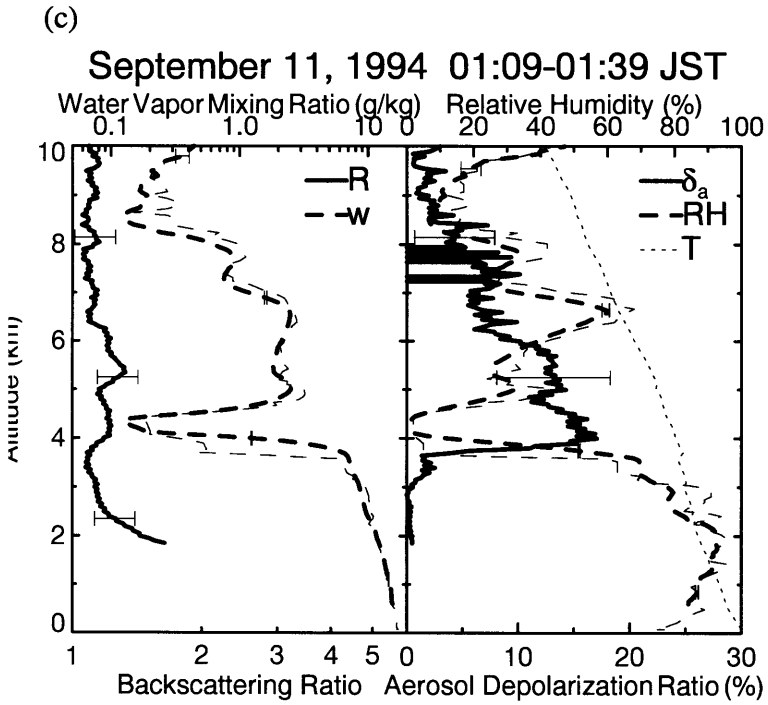

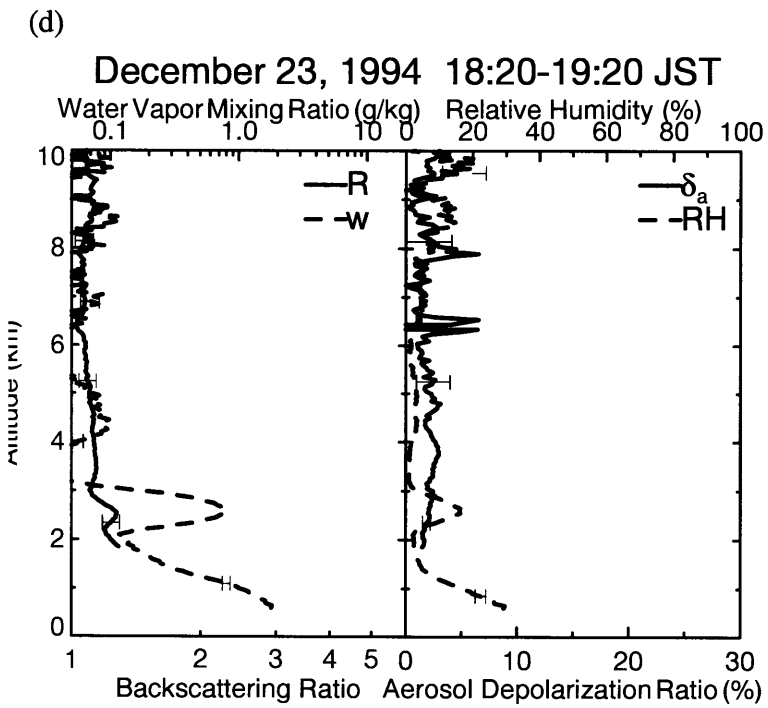

Fig. 4.5 Continued.

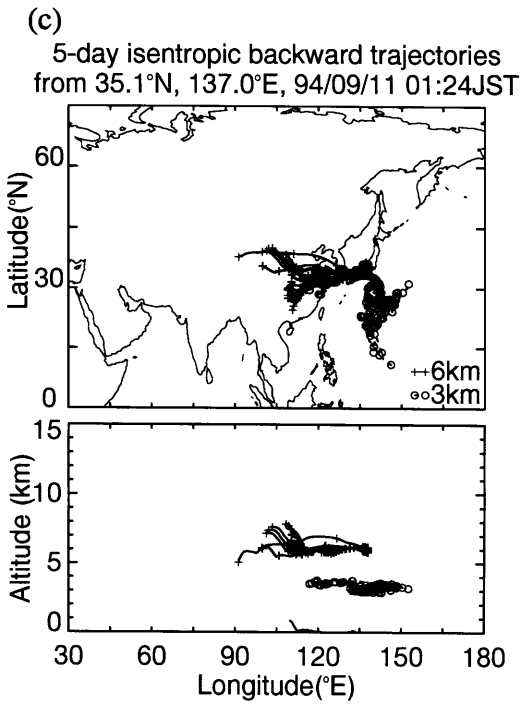

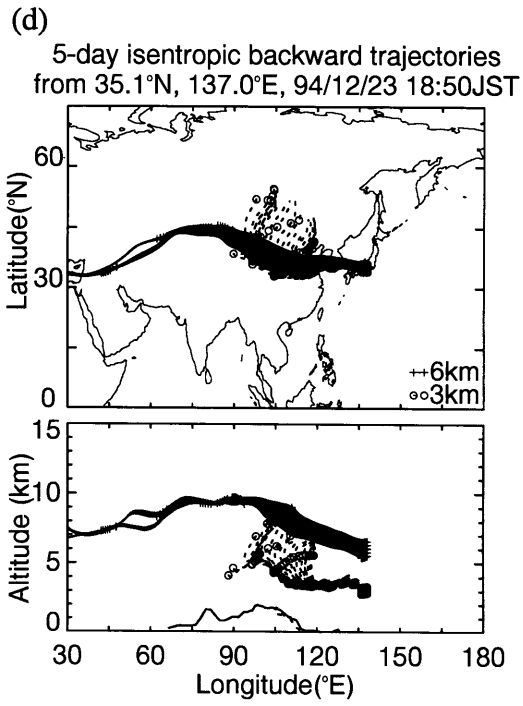

Fig. 4.6 Continued.

(a)

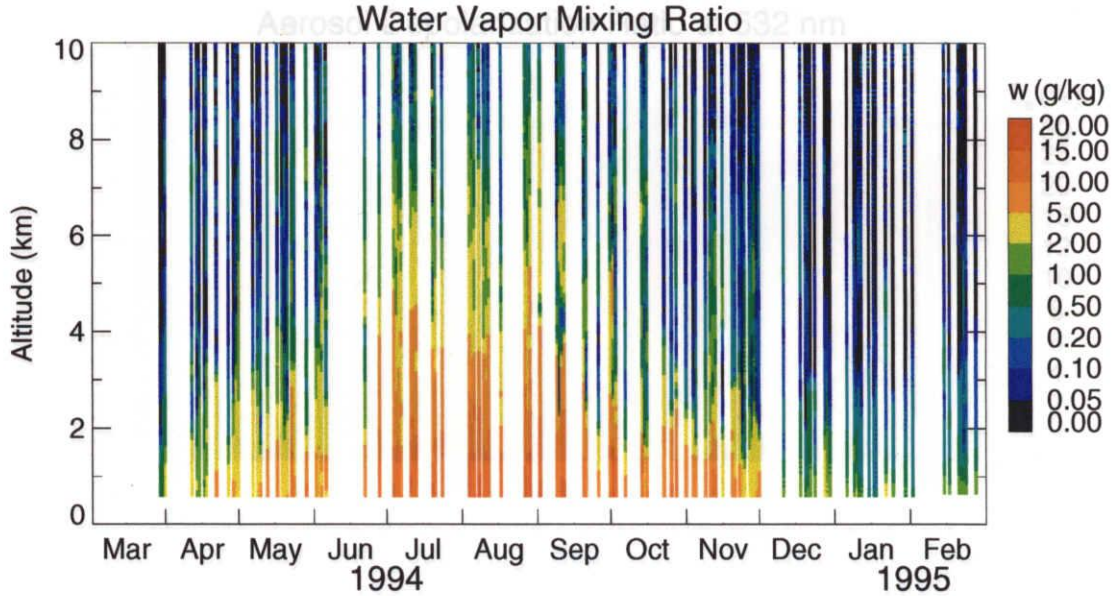

(b)

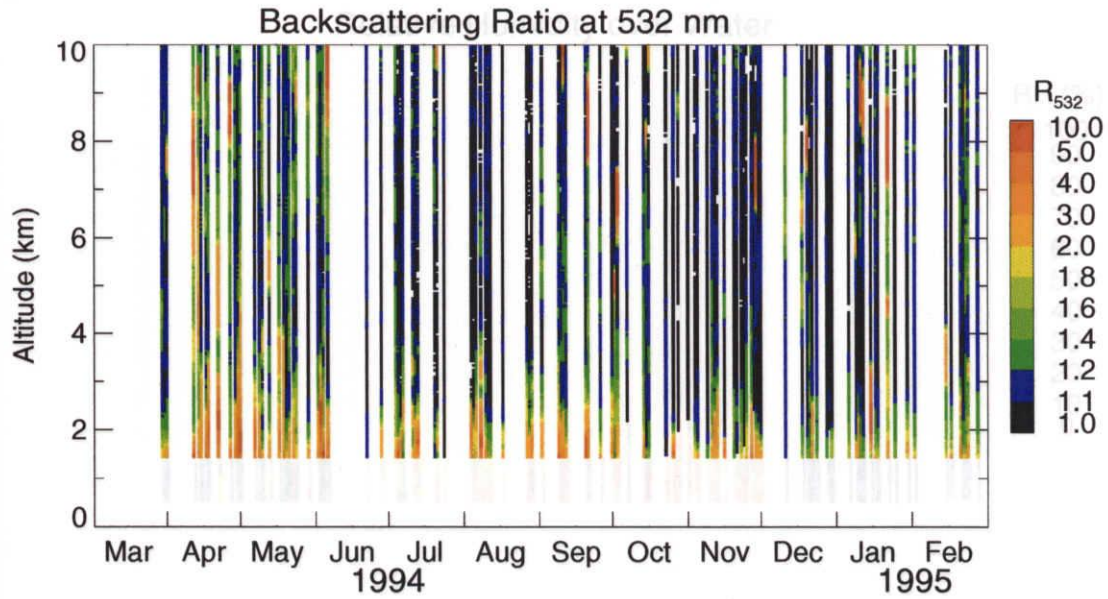

Fig. 4.7 temporal-vertical cross sections of (a) water vapor mixing ratio, (b) backscattering ratio at 532 nm, (c) aerosol depolarization ratio at 532 nm, and (d) relative humidity over water obtained with the Raman lidar at Nagoya (35.1°N, 137.0°E) for the period March 1994 to February 1995.

(c)

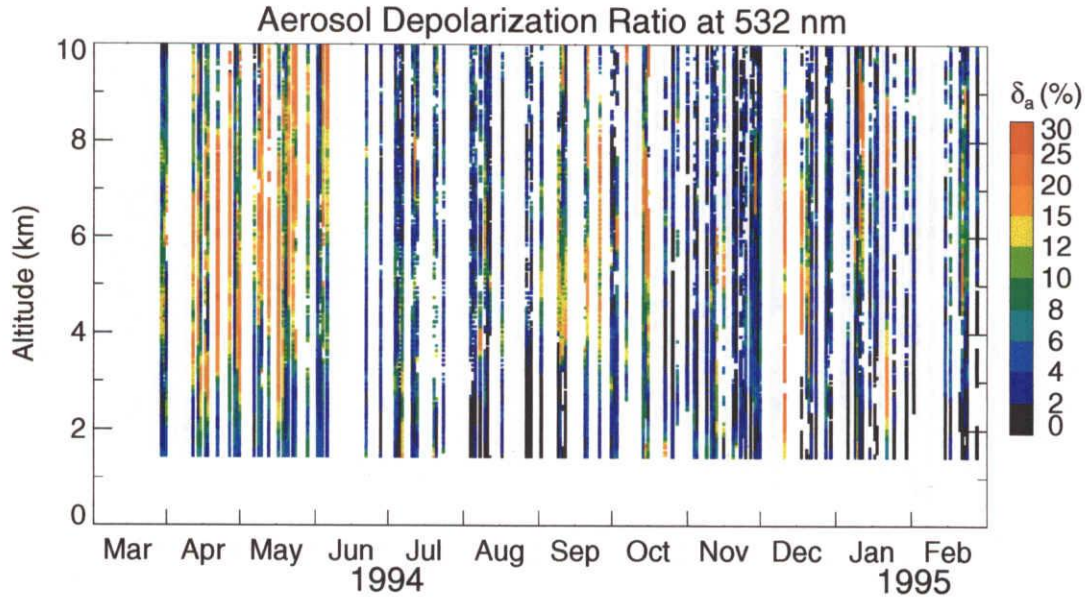

(d)

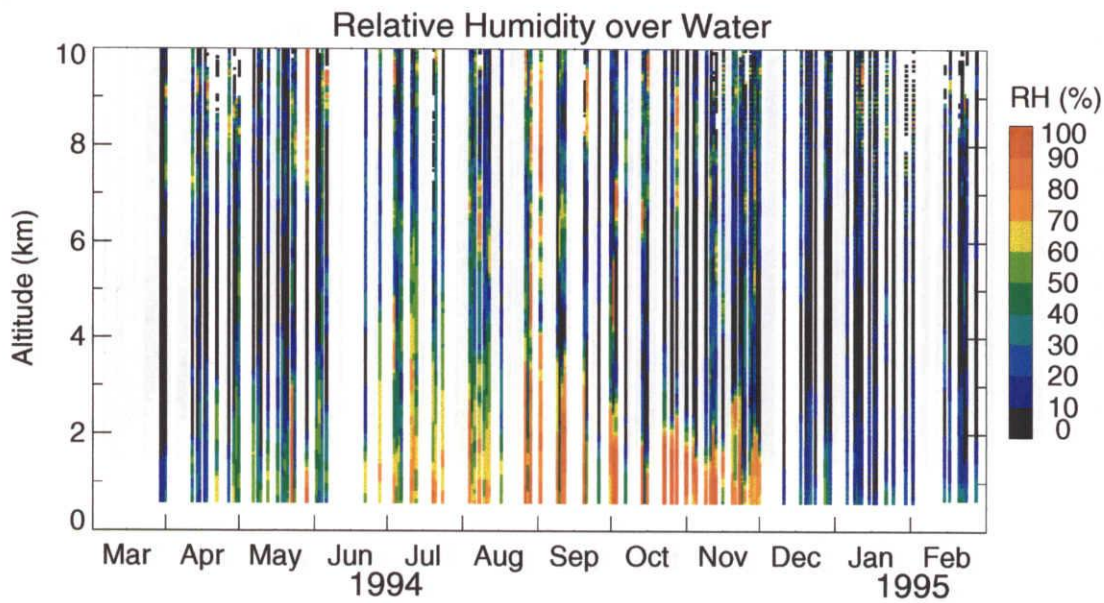

Fig. 4.7 Continued.

(a)

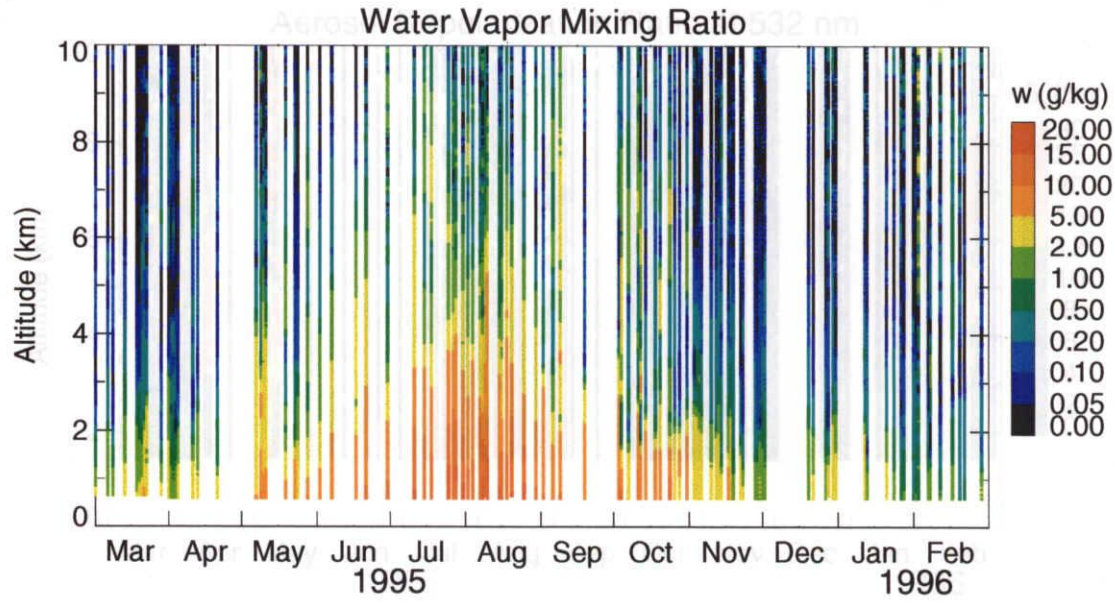

(b)

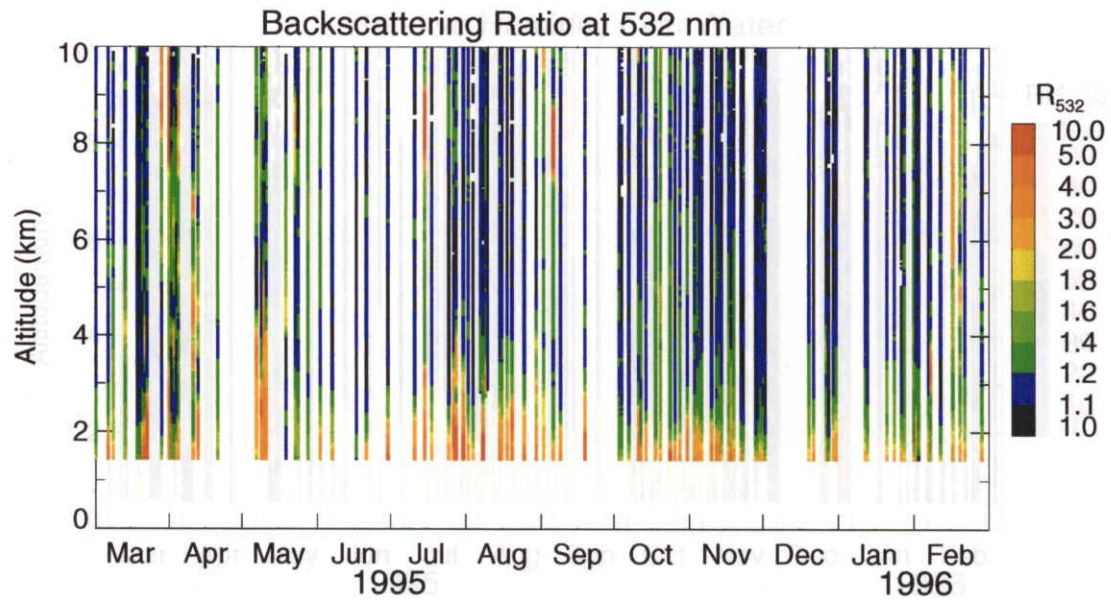

Fig. 4.8 Same as Fig. 4.7 but for the period March 1995 to February 1996.

(c)

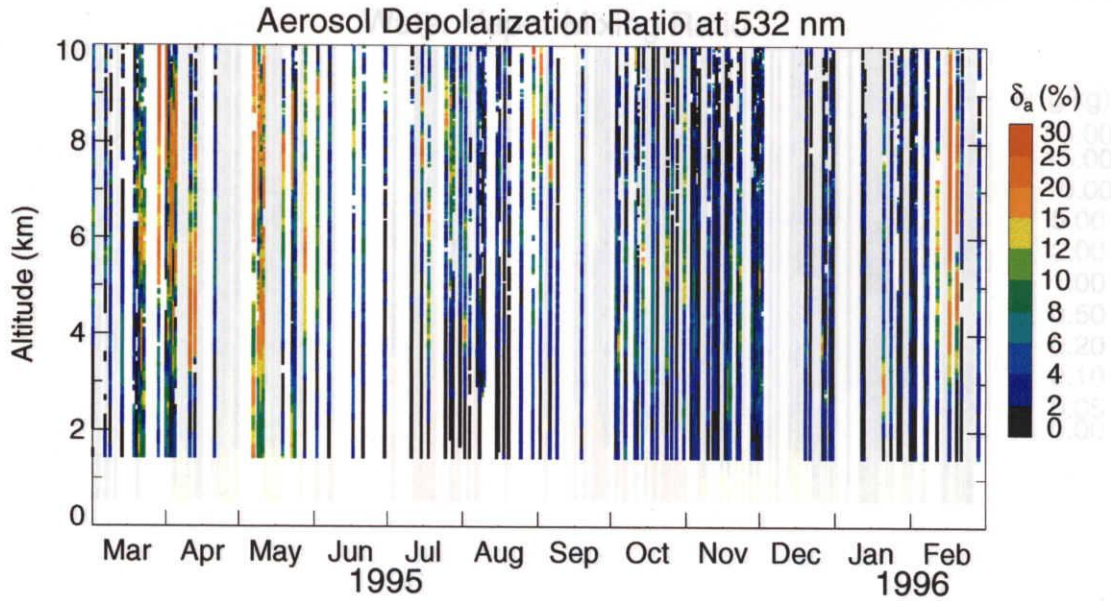

(d)

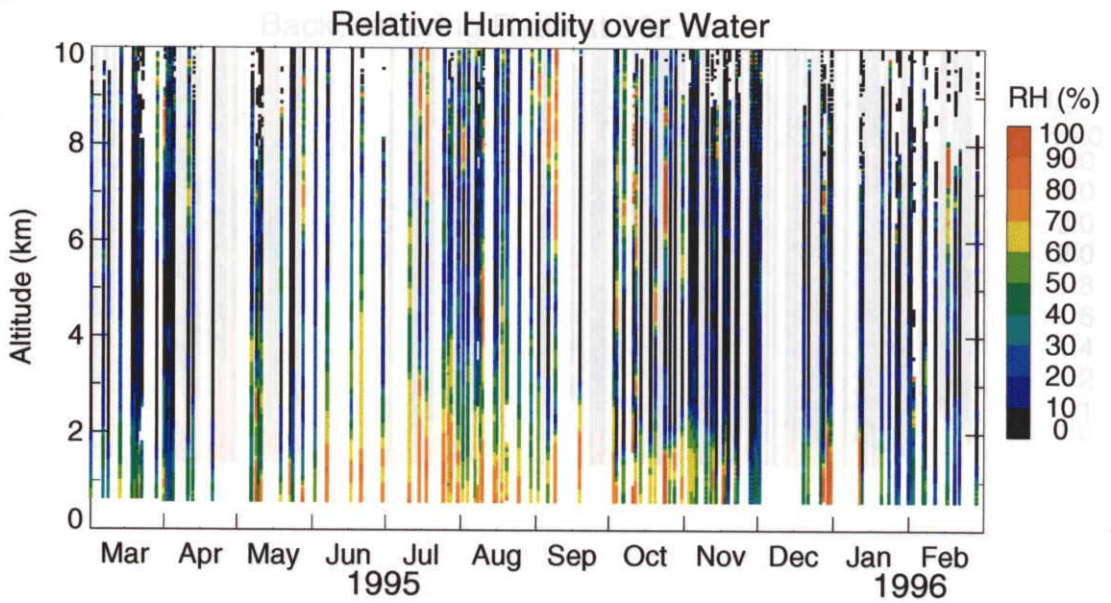

Fig. 4.8 Continued.

(a)

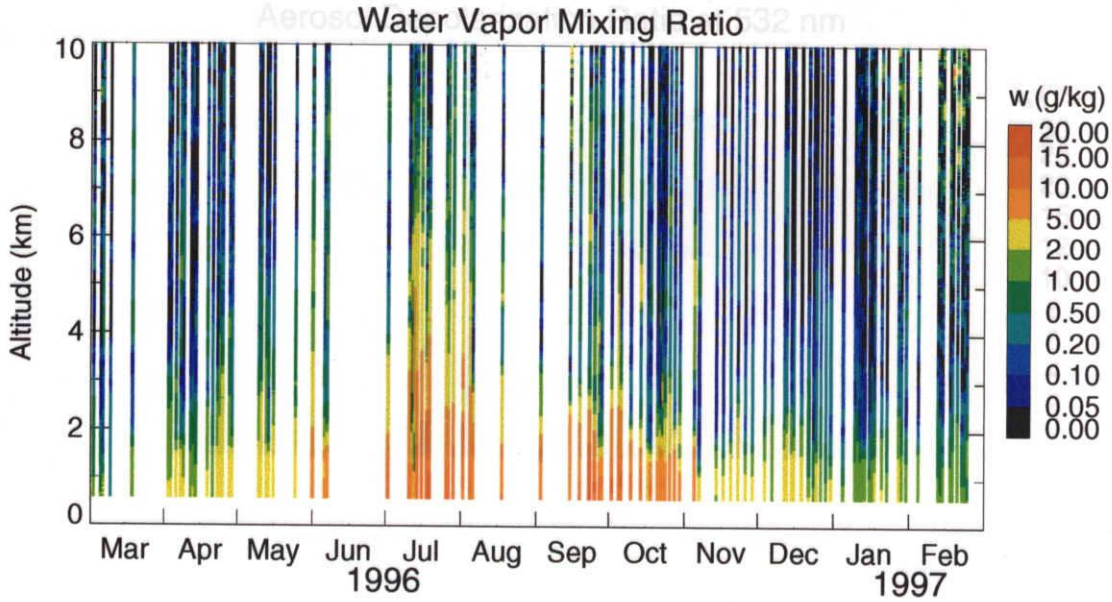

(b)

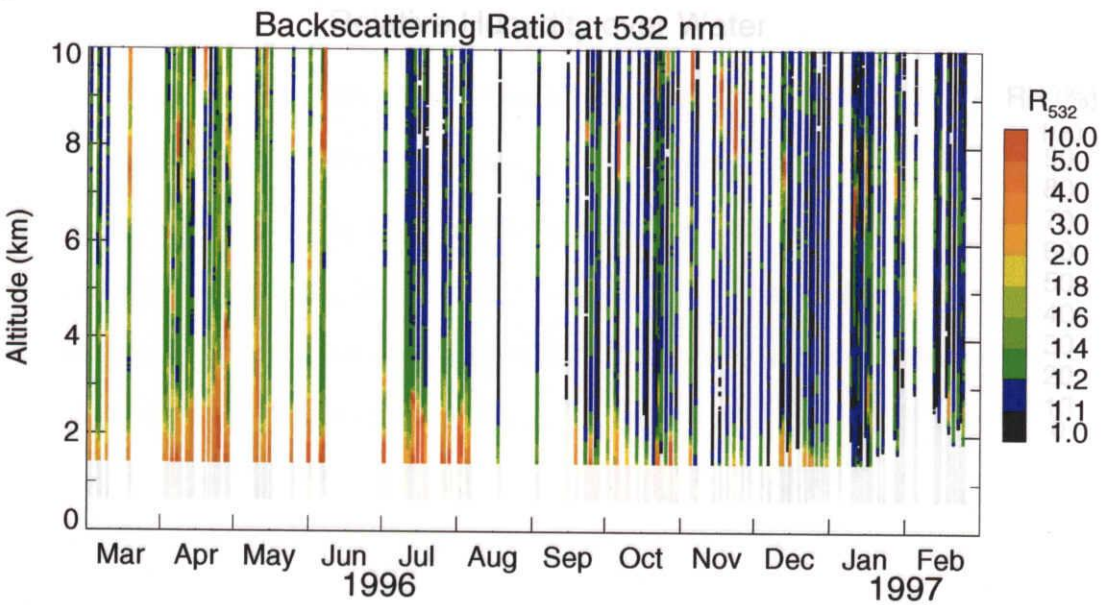

Fig. 4.9 Same as Fig. 4.7 but for the period March 1996 to February 1997.

(c)

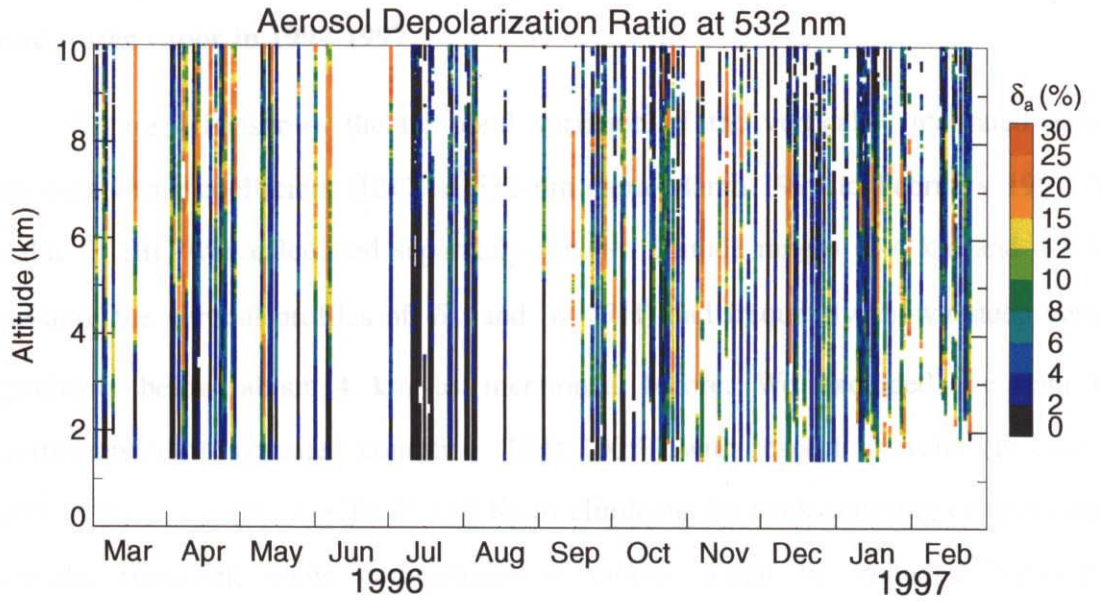

(d)

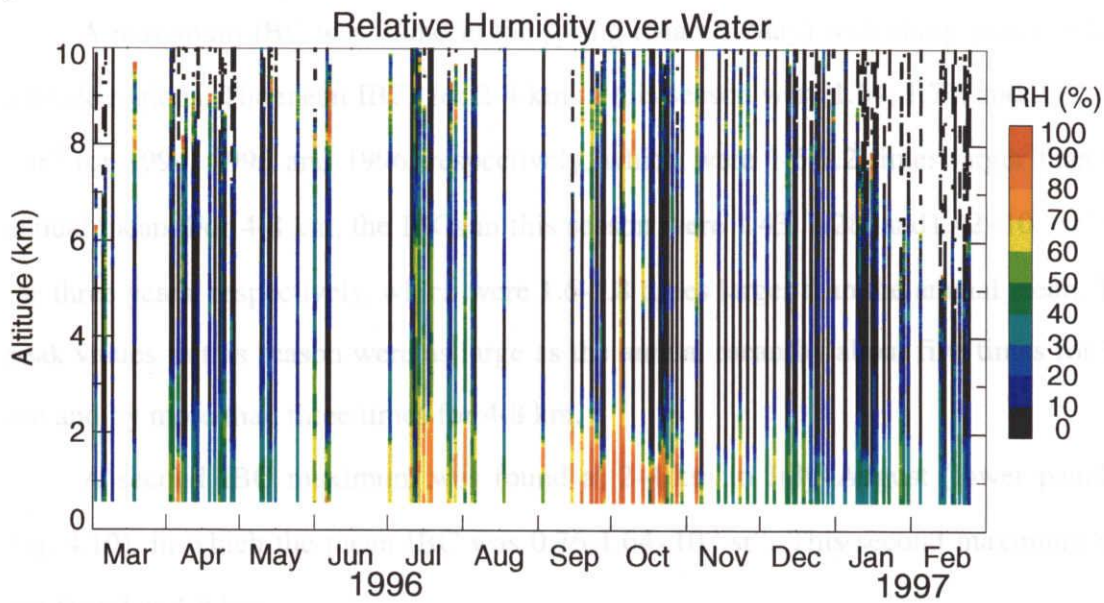

Fig. 4.9 Continued.

4.2.2 Temporal variations of vertically integrated aerosol backscattering coefficient and water vapor in 1994-1997

Figure 4.10 shows the temporal variation of the vertically integrated aerosol backscattering coefficient (IBC) at 532 nm from March 1994 to February 1997. The value of IBC was calculated separately for two altitude ranges (2-4 km and 4-8 km) because the vertical profiles of δ_a and w (RH) had frequently shown steep vertical gradients below about 4 km as mentioned before. We excluded the data that corresponded to saturated condition (RH$\geq$100%) with respect to water (in case T> 273.15 K) or ice (in case T$\leq$273.15 K) to eliminate the backscattering components of clouds. However, some components of clouds might be included because of uncertainties in the humidity measurements and because of the temporal and vertical resolution of the data.

A maximum IBC was found in the spring (March–May) with sharp peaks in both altitude regions. The mean IBCs for 2-4 km in this season were 1.64, 1.71, and 2.22×10^{-3} sr^{-1} for 1994, 1995 and 1996, respectively, which were 1.6-2.2 times larger than the annual mean. For 4-8 km, the IBCs in this season were 1.43, 1.28, and1.42×10^{-3} sr^{-1} for the three years, respectively, which were 1.6-1.8 times larger than the annual mean. The peak values in this season were as large as the annual mean by about five times for 2-4 km and by more than three times for 4-8 km.

A second IBC maximum was found at 2-4 km in July–August (lower panel in Fig. 4.10), in which the mean IBC was $0.76\text{-}1.64\times10^{-3}$ sr^{-1}. This second maximum was not found at 4-8 km.

Sasano (1996) measured the vertical profiles of the aerosol extinction coefficients by Mie scattering lidar at Tsukuba (320 km east of our lidar site) in 1990-1993. He found the annual maximum of the aerosol optical thickness in the spring-summer between 0 and 3 km and in the spring between 3 and 12 km. Although his optical parameter and height ranges are slightly different from ours, the seasonal variations in the aerosol column amounts at the two altitude regions are consistent with our results.

One difference in his results compared to ours is that the optical thickness between 0 and 3 km in the summer were sometimes higher value than that in the spring due to the large contribution of aerosol extinction below about 2 km (Fig.2 in his paper).

Figure 4.11 shows the vertically integrated water vapor content (IWVC) observed with the Raman lidar for the same period as shown in Fig. 4.10. A strong seasonal variation of the values by 2 orders of magnitude was found. The maximum occurred from the end of June to September at both altitude regions, where the values reached about 15 kg m^{-2} at 2-4 km and 10 kg m^{-2} at 4-8 km. This time of year approximately corresponds to the time of year when the second IBC maximum was found in 2-4 km.

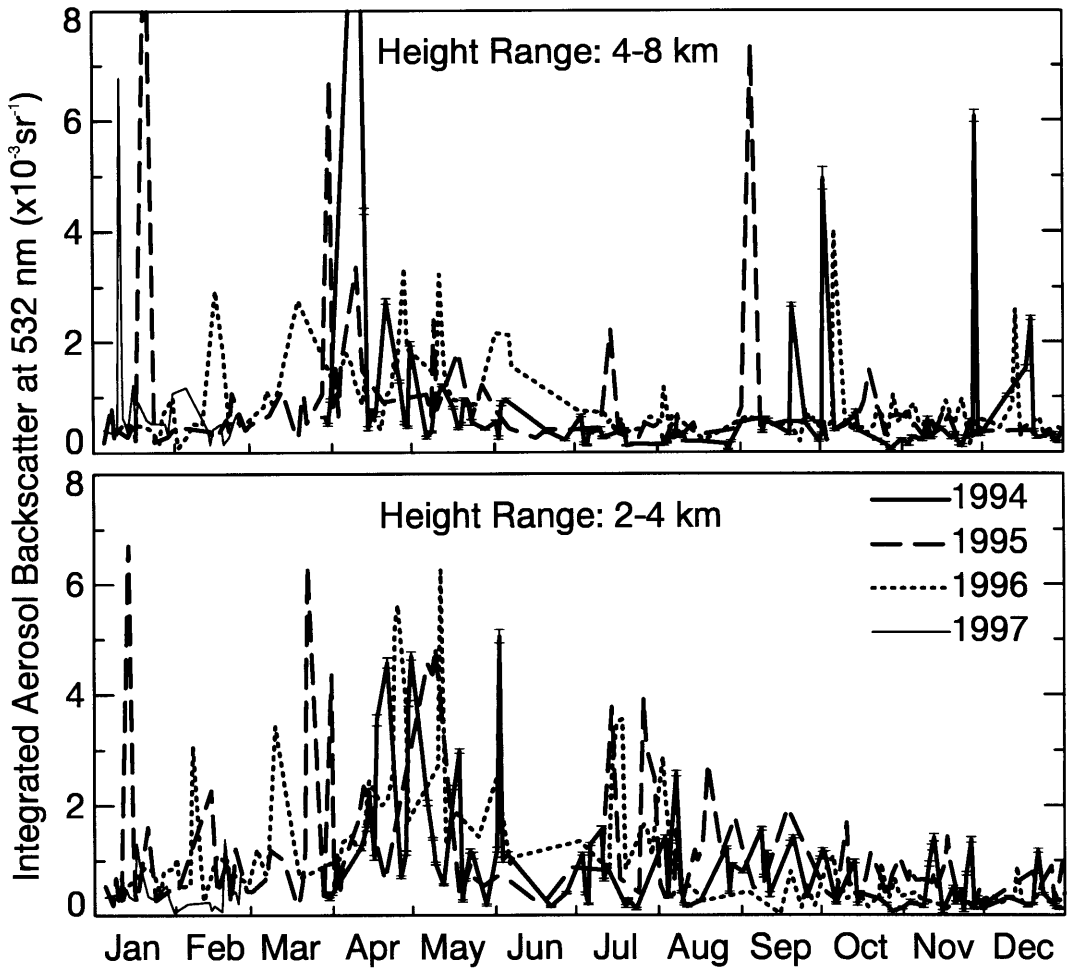

Fig. 4.10 Temporal variation of vertically integrated aerosol backscattering coefficient at 532 nm obtained with the Raman lidar at Nagoya from March 1994 to February 1997. The height ranges of the integration are 4-8 km (upper panel) and 2-4 km (lower panel), respectively.

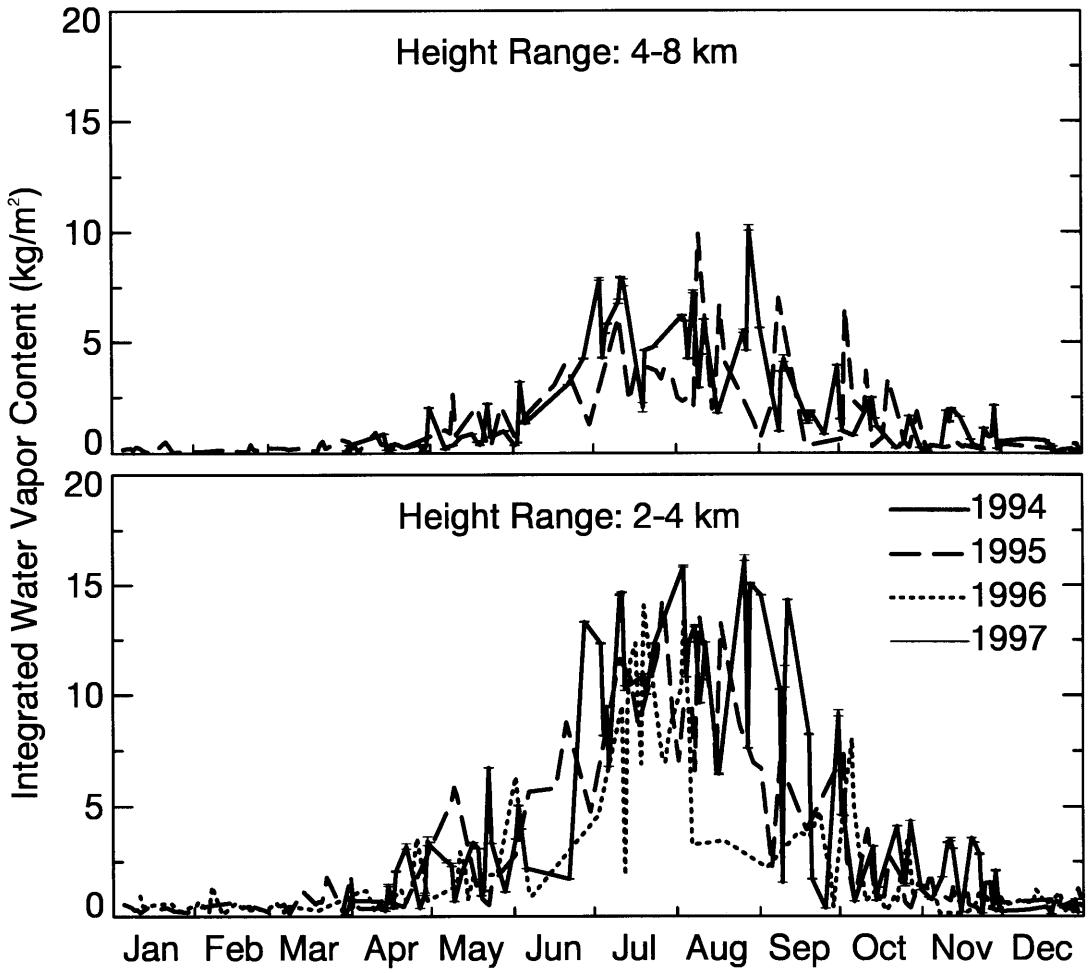

Fig. 4.11 Temporal variation of vertically integrated water vapor content obtained with the Raman lidar at Nagoya from March 1994 to February 1997. The height ranges of the integration are the same as Fig. 4.10.

4.2.3 Aerosol depolarization ratio as a function of relative humidity

Figures 4.12-14 show the scatter plots of the aerosol depolarization ratio δ_a versus the relative humidity RH with respect to water observed with the Raman lidar for the period March 1994 to February 1997. The data plotted are separately for the two altitude regions (2-4 and 4-8 km) in each season. We excluded the data whose measurement uncertainties in δ_a exceeded 5% or the RH were saturated with ice.

Figures 4.12-14 shows the seasonal and altitude dependencies of the distribution. In the spring (Figs. 4.12a, 4.13a, and 4.14a), δ_a values as high as 25% were frequently observed at both altitude regions, indicating substantial existence of nonspherical particles. It should be noted that high depolarization ratios were found in moist air region with RH as high as 80%in the 4-8 km region.

The summer data (Figs. 4.12b, 4.13b, and 4.14b) generally showed low δ_a values (< 5%) over a wide range of RH in both altitude regions and the distribution of δ_a as a function of RH indicated similar characteristics; high δ_a values (> 10%) were found only where the RH was less than about 50% and the maximum value of δ_a decreased with increasing RH.

The autumn data (Figs. 4.12c, 4.13c, and 4.14c) showed different distributions in the two altitude regions. The data in 2-4 km region (lower panels of Figs. 4.12c-14c) generally indicated low δ_a (< 5%) and the distribution was similar to that of the summer (Figs. 4.12b-14b). On the other hand, the data in 4-8 km region (upper panels of Figs. 4.12c-14c) frequently indicated high δ_a (~20%) over a wide range of RH (0-90%); this feature is similar to that found in the spring of 4-8 km (upper panels of Figs. 4.12a-14a).

The data in the winter (Figs. 4.12d, 4.13d, and 4.14d) mostly indicated low δ_a (< 5 %) with low RH (< 20%) in both altitude regions. Some data indicated high δ_a

about 25% and the frequency of these high δ_a values was higher in the 4-8 km region than in the 2-4 km region.

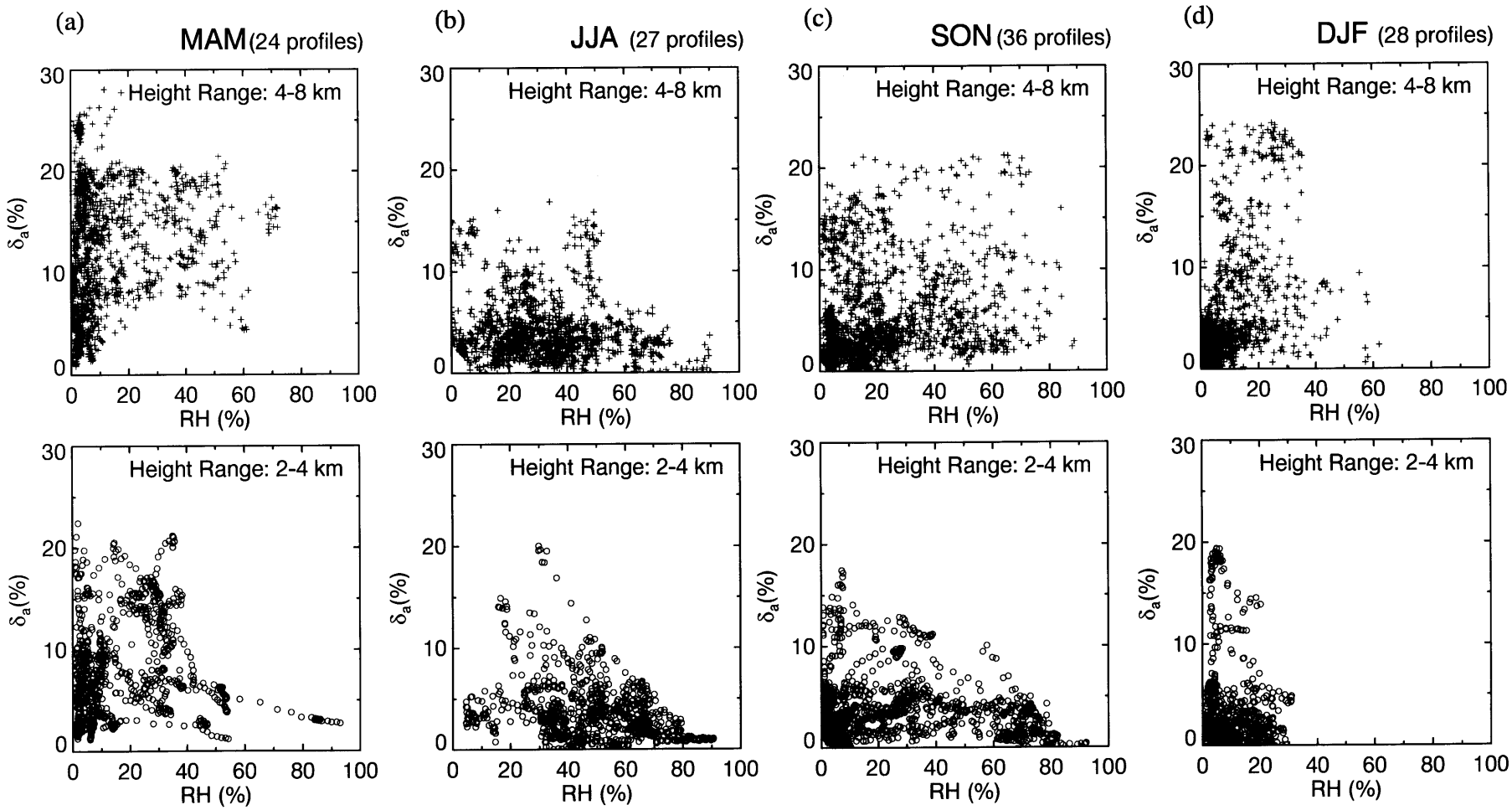

Fig. 4.12 Aerosol depolarization ratio (δ_a) as a function of relative humidity (RH) derived from the Raman lidar observations for the periods (a) March-May, (b) June-August, (c) September-November, and (d) December-February in 1994-1995. The upper panels show the data between altitudes of 4 and 8 km and the lower panels show the data between 2 and 4 km.

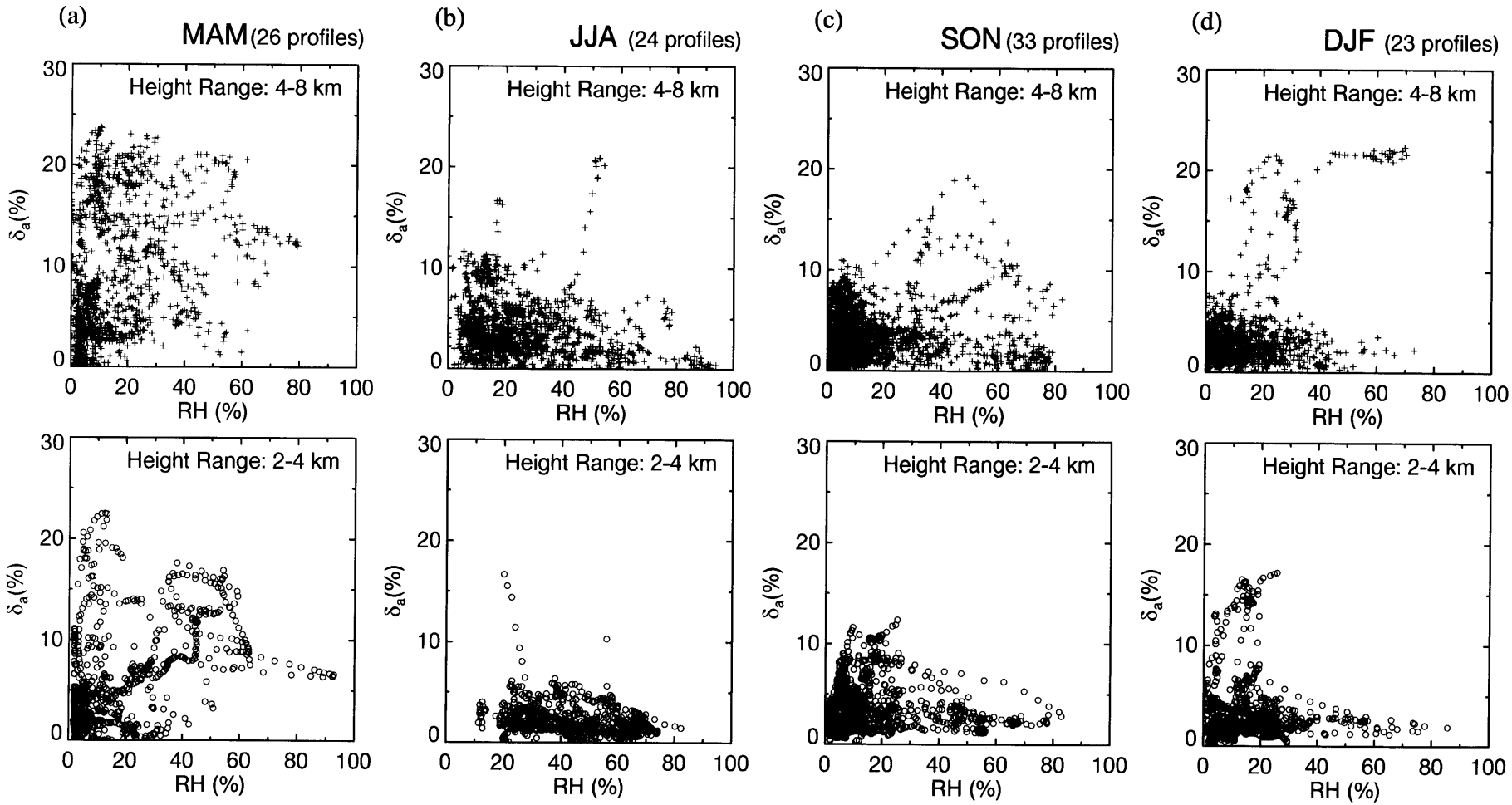

Fig. 4.13 Same as Fig. 4.12 but for the period March 1995 to February 1996.

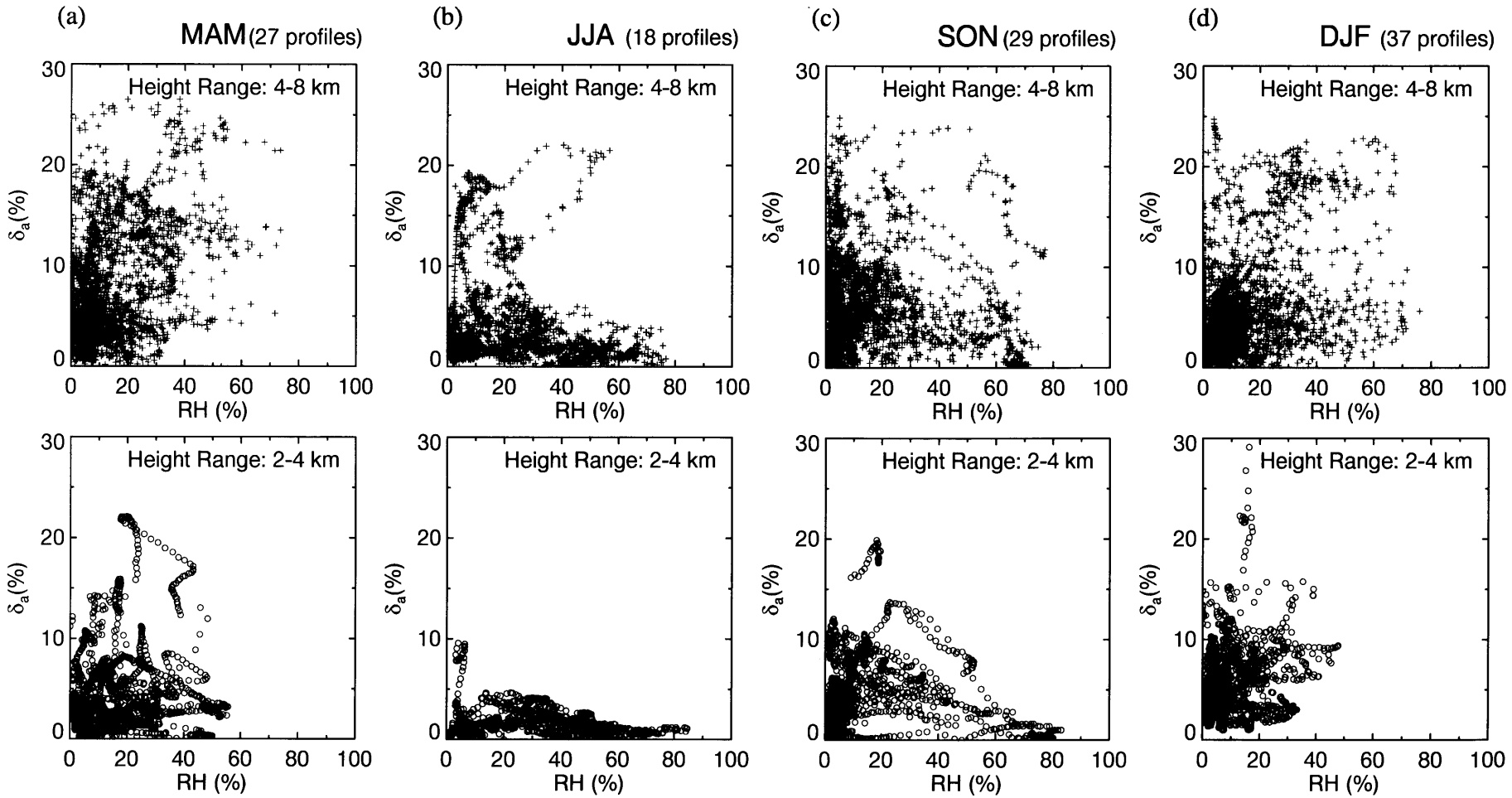

Fig. 4.14 Same as Fig. 4.12 but for the period March 1996 to February 1997.

4.2.4 Discussion

Depolarization ratio as a function of relative humidity and chemical composition of aerosols

The chemical composition of typical aerosol particles can be classified into three types according to the shape (nonsphericity) and the water-solubility (Fig. 4.15). The three types are as follows. (a) Water-insoluble particles (e.g., mineral dust): these particles are mostly nonspherical and hence indicate high δ_a values independent of RH. (b) Water-soluble particles (e.g., H_2SO_4/H_2O solution): these particles do not change phases with changes in the tropospheric condition and always indicate near zero depolarization ratios independent of RH. (c) Water-soluble deliquescent particles (e.g., NaCl, $(NH_4)_2SO_4$): they exist as solution droplets and indicate low δ_a above the deliquescence point (DRH), whereas they exist as crystalline solids and indicate high δ_a below the efflorescence point (CRH). Between the CRH and DRH, the phase (also δ_a) of them depends on the RH history of the particle (e.g., Tang and Munkelwitz, 1994). Table 4.1 shows the values of DRH and CRH of typical water-soluble aerosol particles. It should be noted that the DRH and CRH depend on temperature (Tang and Munkelwitz, 1993; Seinfeld and Pandis, 1998; Onasch et al., 1999), particle size (Chen, 1994), and internal mixing state (Tang et al., 1978; Cohen et al., 1987; Han and Martin, 1999).

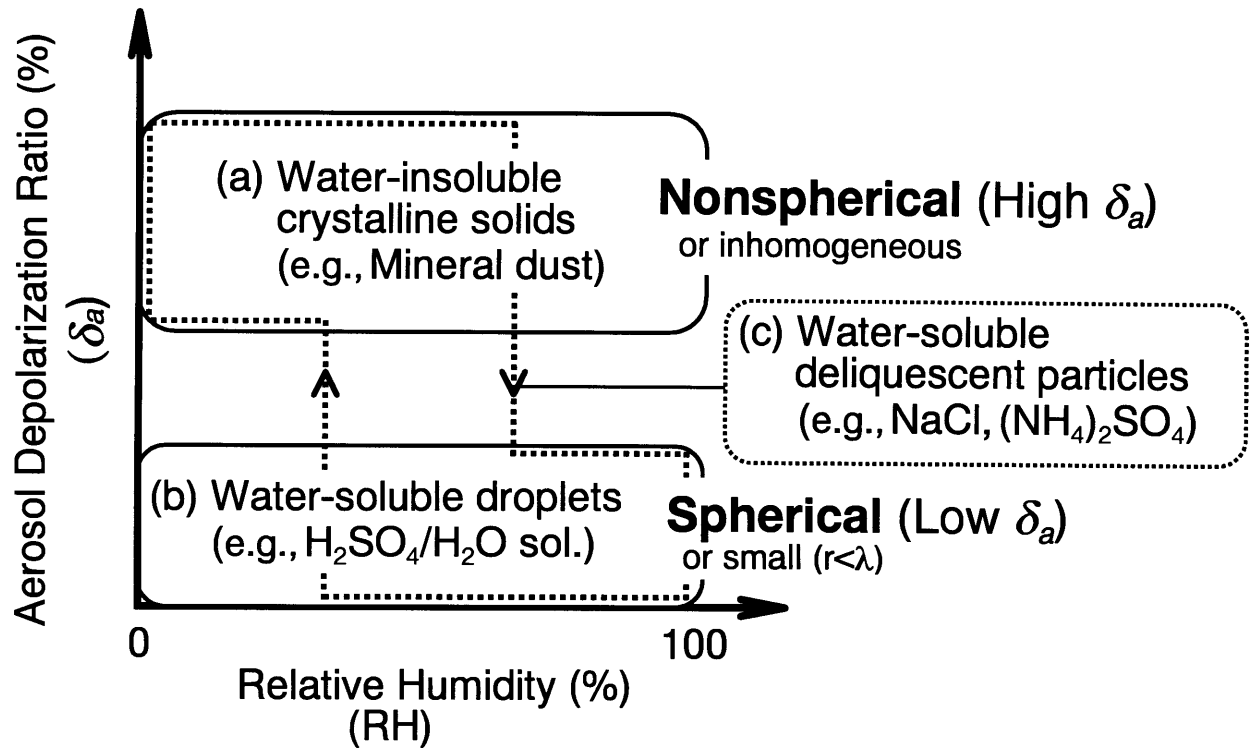

Fig. 4.15 Schematic diagram of the relationship between aerosol depolarization ratio (δ_a) and relative humidity (RH) for three aerosol types: (a) water-insoluble crystalline solids, (b) water-soluble droplets, and (c) water-soluble particles that have properties of deliquescence and efflorescence.

Table 4.1 Deliquescence (DRH) and efflorescence (CRH) humidities of major tropospheric water-soluble particles at 298 K

Composition	DRH (%)	CRH (%)	Ref.
NaCl	75.3	48-46	a
$(NH_4)_2SO_4$	80	40-37	a
NH_4HSO_4	40	20-0.05	a
NH_4NO_3	62	25-32	a
Na_2SO_4	84	59-57	a
$NaNO_3$	74.5	30-0.05	a
$NaCl/(NH_4)_2SO_4$, (mol. ratio/1.9980)	-	21*	b

[a]Tang (1996) [b]Cohen et al. (1987) *at 293K

A few researchers have measured the depolarization of the particles in the laboratory. The reported experimental data are shown in Table 4.2. Cooper et al. (1974) measured the depolarization ratio of salt particles generated in the laboratory using an apparatus similar to the lidar configuration (scattering angle $\theta \geq 177°$ at a wavelength λ=632.8 nm). They reported NaCl particles (number mean diameter was 0.07 μm and the geometric standard deviation 2.3) with δ_a = 5.6-11.1% when the ambient RH was 77-92% (> DRH) and $\delta_a \approx 20\%$ when the RH was 12% (< CRH). Sassen et al. (1989) measured the depolarization ratios of sulfuric acid droplets and crystallized ammonium sulfate in a cloud chamber ($\theta > 178°$ at λ=632.8 nm). In their experiments, the sulfuric acid droplets gradually evaporated and were crystallized by ammonium gas injection, and δ_a gradually changed from 2 to 9-13%. Kuik et al. (1991) measured the scattering matrices of water droplets and irregularly shaped SiO_2 particles ($\theta = \geq 175°$ at λ=632.8 nm). The depolarization ratios calculated from their results by $\delta_a = (1 - F_{22} / F_{11}) / 2$ are $\delta_a \approx 5\%$ for water droplets (the effective radius r_{eff} was 0.75 μm and the effective standard deviation σ_{eff} = 0.45) and $\delta_a \approx 30\%$ for SiO_2 particles (r_{eff} = 15 μm and σ_{eff} = 0.8). It should be noted that the δ_a value depends not only shape and chemical composition of the particles but also on the particles size (Asano and Sato, 1980; Mischenko and Sassen, 1998) so that the values of δ_a in Table 4.2 should be considered as typical values for each aerosol.

Table 4.2 Aerosol depolarization ratio (δ_a) measured by the laboratory experiments

Composition	δ_a (%)	RH (%)	λ (nm)	θ(°)	particle size distribution	Ref.
NaCl	5.6-11	77-92	632.8	≥177	r_m=0.07 μm, σ=2.3	a
NaCl	20	12	632.8	≥177	r_m=0.07 μm, σ=2.3	a
NaCl	29	dry	632.8	165	r_m=0.628 μm,σ=0.20 μm	b
$(NH_4)_2SO_4$	8	dry	632.8	165	r_m=0.640 μm,σ=0.21 μm	b
SiO_2	28	dry	546.0	166	r_m=0.15 μm, σ=2	c
SiO_2	30	-	632.8	175	r_{eff}=15 μm, σ_{eff}=0.8	d
H_2O droplet	5	-	632.8	175	r_{eff}=0.75μm,σ_{eff}=0.45	d
H_2SO_4	2	-	632.8	>178	-	e
$(NH_4)_2SO_4$	9-13	-	632.8	>178	-	e

[a] Cooper et al. (1974) [b] Perry et al. (1978) [c] Holland and Gagne (1970)
[d] Kuik et al. (1991) [e] Sassen et al. (1989)

The δ_a values of 25% that we observed in the 2-8 km region in the spring and 4-8 km region in the autumn and winter are close to those of NaCl crystals and irregularly shaped SiO_2 particles.

There are two possibilities to explain δ_a values less than 5% that we dominantly observed in the 2-8 km region in the summer and winter and in the 2-4 km region in the autumn. One explanation is that spherical particles like droplets predominantly exist in the air, and the other explanation is that small particles whose radii are smaller than the laser wavelength (0.532 μm) predominantly exist in the air. Mischenko and Sassen (1998) have theoretically shown that polydisperse randomly oriented nonspherical particles (ellipsoid, cylinder, and Chevyshev particles with refractive index of $1.308+1.328\times10^{-6}i$) can produce low δ_a value less than 5% at λ=0.532 μm if the effective radius is less than about 0.4 μm. In most cases, these small particles (accumulation mode) are generated by the condensation of water-soluble substances (e.g., Heitzenberg, 1993). Therefore, δ_a values less than 5% were probably due to the water-soluble particles.

Several researchers collected and analyzed free tropospheric aerosol particles in the Northwestern Pacific region. Okada (1983) found that 96% of the particles with a 0.1-0.35 μm radius were hygroscopic (contained water-soluble substanced) at an altitude of 3.15 km over Kii peninsula (about 75 km southwest of the lidar site). Yamato and Ono (1989) collected aerosol particles between 2 and 7.6 km over the Sea of Japan in wintertime and found most of the particles were composed of sulfuric acid and the fraction of ammonium sulfates increased with decreasing altitude. Ikegami et al. (1993) observed aerosol particles at 4.5 km over the northern Pacific Ocean region (0°N-34°N). They intermittently observed high number concentrations of sea salt particles in the tropical areas. They also ubiquitously found sulfate-containing particles (H_2SO_4 and $(NH_4)_2SO_4$) throughout their observation. Iwasaka et al. (1988) collected many irregularly shaped particles in the free troposphere (4.35 and 2.25 km altitudes) over

Wakasa Bay (about 130 km northwest of the lidar site) in the spring season. They concluded these particles were Kosa (Asian dust) based on transmission electron microscope (TEM) images and trajectory analysis.

Based on their results, the main aerosol constituents that control the aerosol depolarization ratios in the free troposphere over Nagoya may be as follows. (a) Nonspherical dust particles from the Asian Continent produce high δ_a values (about 25%) over a wide range of RH. (b) Spherical sulfuric acid droplets produce low δ_a values (less than 5%) over a wide range of RH. (c) Ammonium sulfate and sea-salt particles produce low δ_a values by existing as droplets when the RH is above the DRH, or above the CRH due to hysteresis. When the RH is below these phase transformation points, they exist as nonspherical crystals and indicate high δ_a values if they are larger than the laser wavelength ($r > \lambda$), or indicate low δ_a values if they are small ($r < \lambda$).

We must note that the value of δ_a measured with the lidar is averaged temporally (~ 30 minutes) and vertically (over 330-350 m) so that if several kinds of particles with different δ_a values coexist in the air, the value indicates the average weighted by the particle's backscattering cross section.

It is noteworthy that Iwasaka et al. (1988) and Ikegami et al. (1993) found that some mineral dust particles were coated with sulfuric acid solution in the free troposphere. These internal mixtures of such particles might affect their δ_a values and the dependence on RH.

Evaluation of the influence of continental and maritime air on the lidar data

As shown in Figs. 4.12-14, the aerosol depolarization ratios as a function of relative humidity indicated significant seasonal and altitude dependencies over the lidar site. This suggests that the major aerosol chemical constituents varied with season and altitude. One important step in determining the aerosol constituents at a location is

transport from the sources. Here, we attempt to estimate the contribution of continental and maritime sources on the lidar data with a simplified transport model.

The meteorological data used in the computation of the trajectories were global objective analyses supplied by the JMA (GANAL (or GAPLX after March 1996)). The data consisted of geopotential height, horizontal wind, temperature and humidity at 16 (18 for GAPLX) pressure levels from the surface to 10 hPa (humidity is available below 300 hPa) at 12 (6 for GAPLX) hour intervals. The horizontal resolution was 1.875° (1.25° for GAPLX). The trajectories were computed in the following way (see Appendix B for more detail). Twenty-five air parcels were initially located around the lidar site (35.1°N, 137.0°E) in steps of 0.5° for latitude and longitude (5×5) at the time and the altitude (potential temperature) of the lidar data. The air parcels were advected backward on the isentropic surface for five days with a time step of 1 hour. To reduce the inaccuracy produced by the isentropic assumption, we terminated the computations if the air parcel intersected with the vertically unstable layer or the Earth's surface, or the air became saturated with water or ice.

The air mass and the aerosol particles contained in it can be classified into two groups: continental and maritime. The continental air can contain both water-soluble and insoluble particles that originate from natural and anthropogenic sources over land. Their main constituents are sulfate, nitrate, ammonium, carbon, and crustal compounds (Pandis et al., 1995; Seinfeld and Pandis, 1998). The maritime air mainly contains water-soluble particles of an oceanic origin and their main constituents are sea-salt and non-sea-salt sulfates. Some distinctive constituents only produced from the continental sources are water-insoluble substances such as mineral dusts of crustal compounds.

In order to evaluate the influence of the continental and maritime air on the lidar data during transportation, we introduced the following factor defined as

$$r_{continent}(z,t)=\frac{1}{N}\sum_{n=1}^{N}\frac{1}{T}\int_{t-T}^{t} f_{n,continent}(t')dt' ,$$

where

$$f_{n,continent} = \begin{cases} 1(\textit{over the continent}) \\ 0(\textit{over the ocean}) \end{cases},$$

and

$$r_{maritime}(z,t) = 1 - r_{continental}(z,t). \qquad (4\text{-}1).$$

Here, z and t are the altitude and time of the lidar data, $N(=25)$ is the number of the air parcels computed in the trajectory, n is the air parcel's number located around the observational site, and $T(\leq 5d)$ is the duration of the trajectory. The influence of aerosol particles produced before the five days of the measurements is expected to be small because the residence time of the tropospheric particles and the precipitation cycle in mid-latitude regions are about five days each (Warneck, 1988). We must notice that Eq. (4-1) assumes a source strength that is equal at all points along the trajectories because we have little information on its spatial and temporal variations. For example, if all of the air parcels pass over the continent (ocean) throughout the trajectories, $r_{continent\,(\,maritime\,)} = 1$, or if all of the air parcels pass over the continent during half of the trajectories, $r_{continent} = r_{maritime} = 0.5$. This analysis is based on very simple assumptions so that the derived factors are considered as qualitative or at best, semi-quantitative indicators of the contributions of the two source areas.

Figures 4.16-18 show the frequency distributions of $r_{continent}$ for each season and altitude region. It is found the distributions of $r_{continent}$ in the spring and winter at both altitude regions (2-4 and 4-8 km) and those in the autumn in the 4-8 km region indicated the maximum frequency at 0.7-0.9, and more than 90% of the values were larger than 0.5, suggesting that the continental air prevailed over the lidar site in these regions. As can be seen in the backward trajectories (Figs. 4.6a, 4.6c (arrived at 6 km), and 4.6d), the air parcels in these regions had passed over the Asian Continent due to the westerly flow. The distribution of $r_{continent}$ in the summer (Figs. 4.16b, 4.17b, and 4.18b) mostly

showed the maximum at $r_{continent}$=0-0.1, indicating that the maritime air prevailed in this season. The autumn data in 2-4 km (lower panels in Figs. 4.16c, 4.17c, and 4.18c) also showed substantial fraction of small $r_{continent}$ values. The air parcels in these regions had mainly passed over the Pacific Ocean associated with the circulation of Pacific high (Figs. 4.6b and 4.6c (arrived at 3 km)).

The other feature found in Figs 4.16-18 is that $r_{continent}$ values in the 2-4 km region (lower panels) were smaller than those in the 4-8 km region (upper panels) in each season. One reason for these small $r_{continent}$ values in 2-4 km region is that the air parcels in the 2-4 km region traveled for shorter distances than in the 4-8 km region because of the weak wind speed so that the they are mainly affected by maritime source around the lidar site. The other reason is that many air parcels arrived at 2-4 km region intersected vertically unstable layer before reaching the continental areas from the lidar site. For example, 48% of the air parcels arrived at 2-4 km intersected vertically unstable layer within five days before the measurements, while 25% of them at 4-8 km intersected the unstable layer in the spring of 1994.

Figures 4.19-21 show the temporal-vertical cross section of the values of $r_{continent}$ for the period March 1994 to February 1997. Large $r_{continent}$ values (> 0.7) were generally found above about 4 km in the spring, autumn, and winter, where≤as small values (< 0.5) were found over the troposphere in the summer and below about 4 km in the autumn. It is to be noted that the seasonal-vertical variation of $r_{continent}$ was similar to that of the water vapor mixing ratio (Fig. 4.7a-9a). This correspondence (dry air had been mostly carried over the continent whereas moist air had been carried over the ocean) suggests that the factors $r_{continent}$ and $r_{maritime}$ successfully represented the characteristics of the two air mass types.

Figures 4.22-4.24 show the seasonal (three months) mean geopotential heights and wind field vector at 700 hPa (approximately at 3 km height) and 400hPa (approximately at 7 km height) in 1994-1997. A westerly flow associated with mid-

latitude jet streams predominated over the lidar site (Figs. 4.22a-24a, 4.22d-24d, and upper panels of Fig. 4.22c-24c) when large $r_{continent}$ values were found. On the other hand, the southwesterly flow associated with the circulation of Pacific high predominated over the lidar site (Fig. 4.22b-24b and lower panel of Fig. 4.22c-24c) when small $r_{continent}$ values were found.

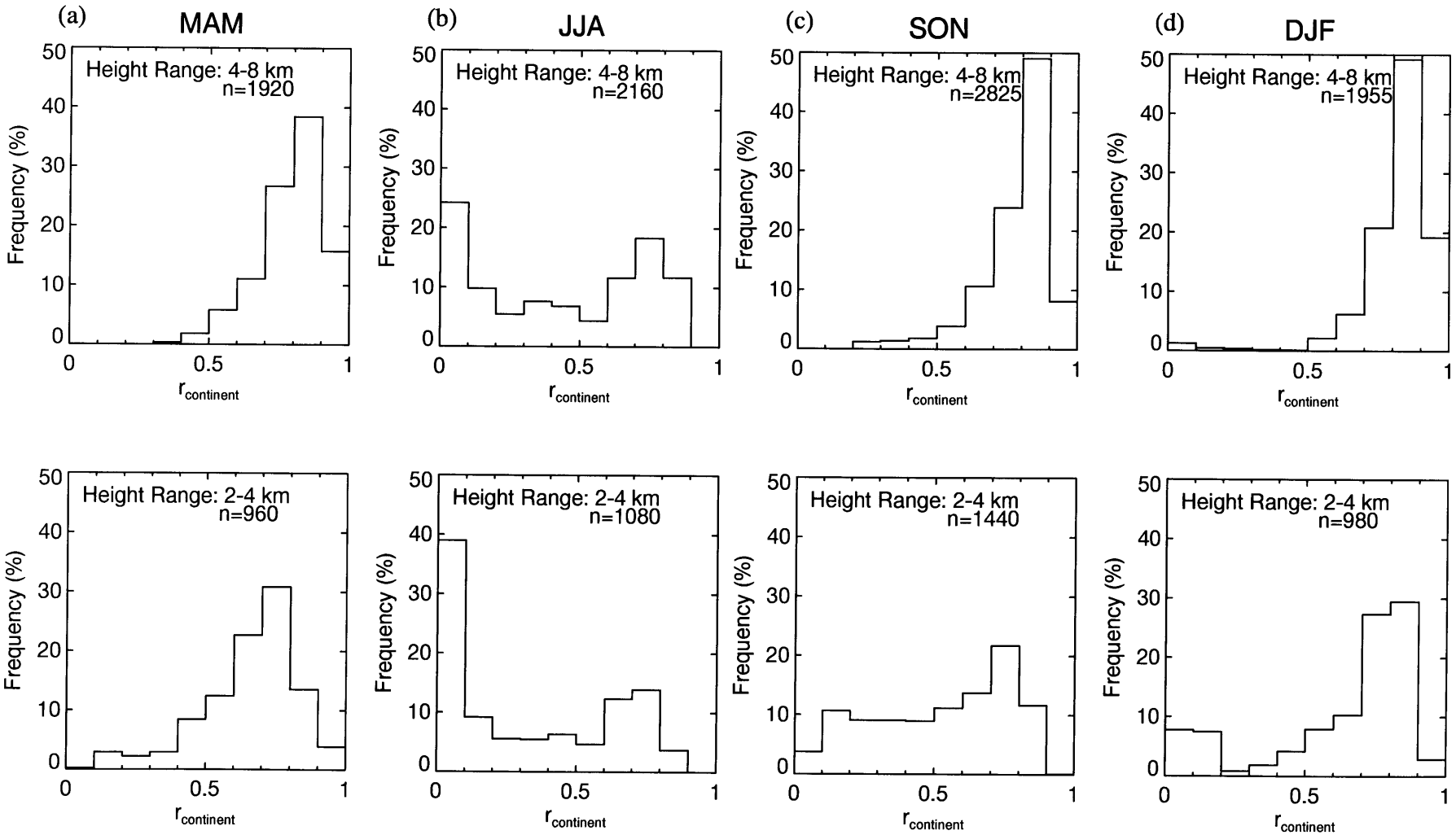

Fig. 4.16 Frequency distributions of continental transport factor $r_{continent}$ (fraction of the back trajectories passing over the continental areas on the way to the lidar site) for the periods (a) March-May, (b) June-August, (c) September-November, and (d) December-February for the period March 1994 to February 1995. The upper panel shows the data between 4 and 8 km and the lower panel shows the data between 2 and 4 km.

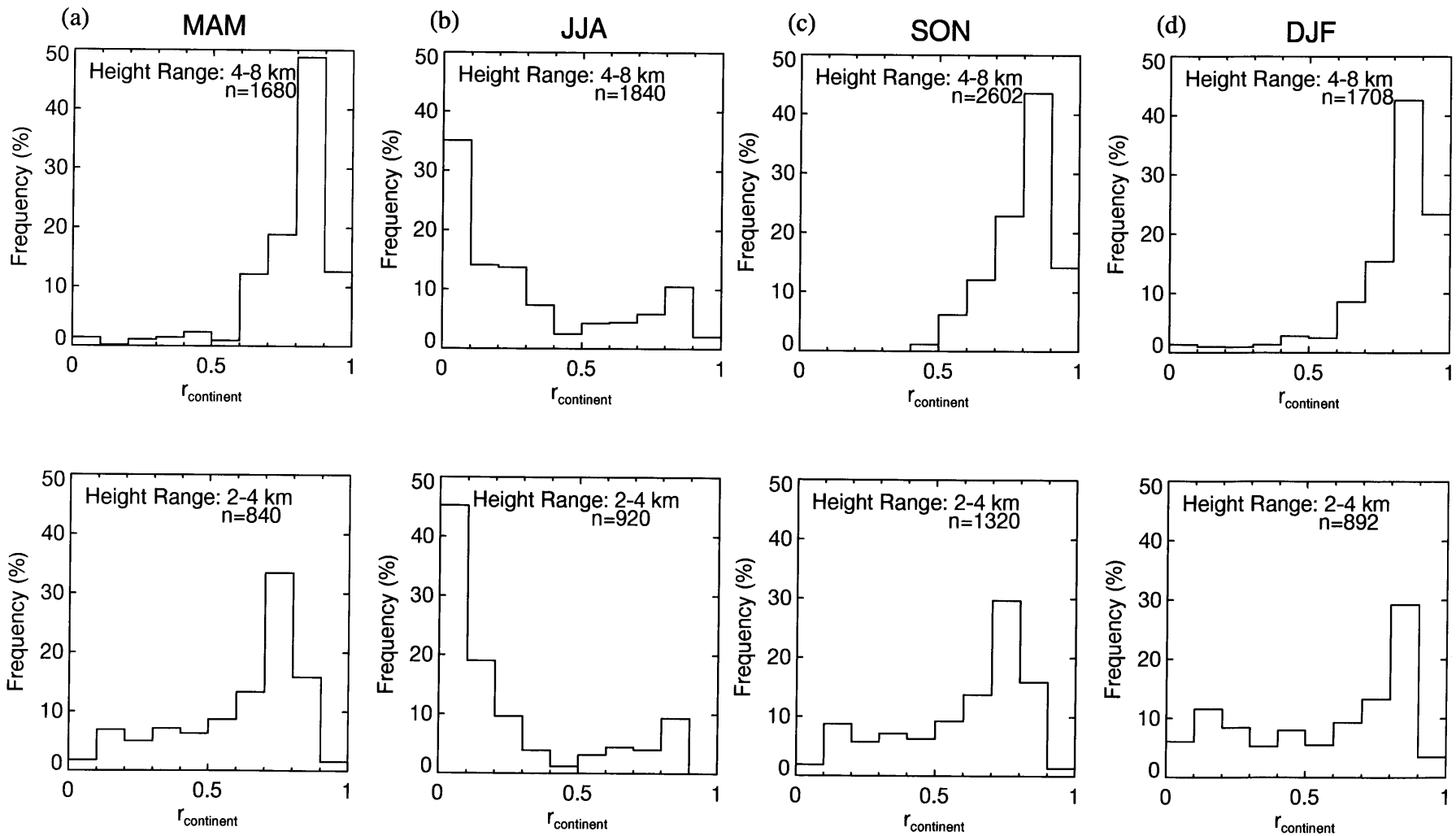

Fig. 4.17 Same as Fig. 4.16 but for the period March 1995 to February 1996.

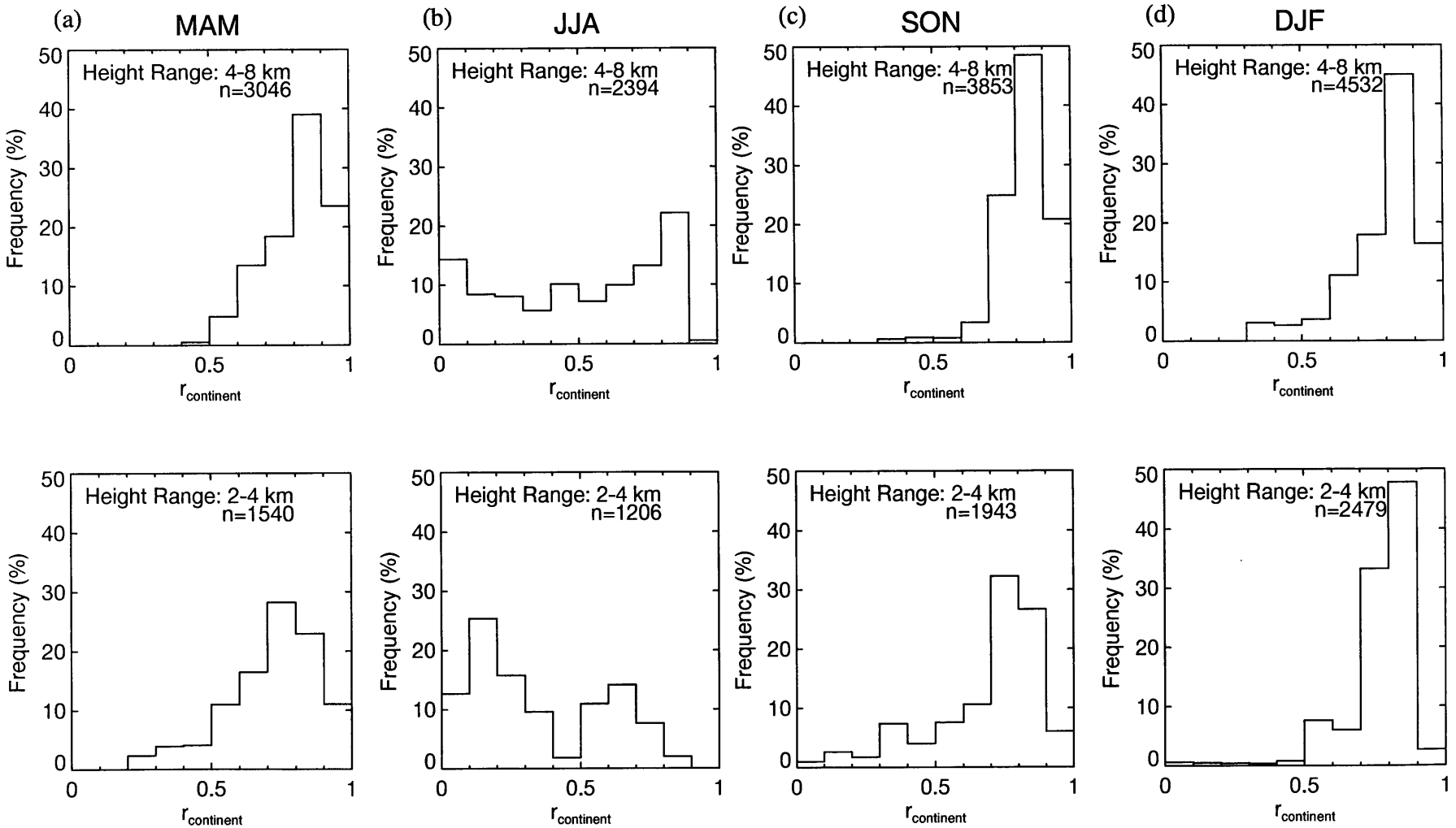

Fig. 4.18 Same as Fig. 4.16 but for the period March 1996 to February 1997.

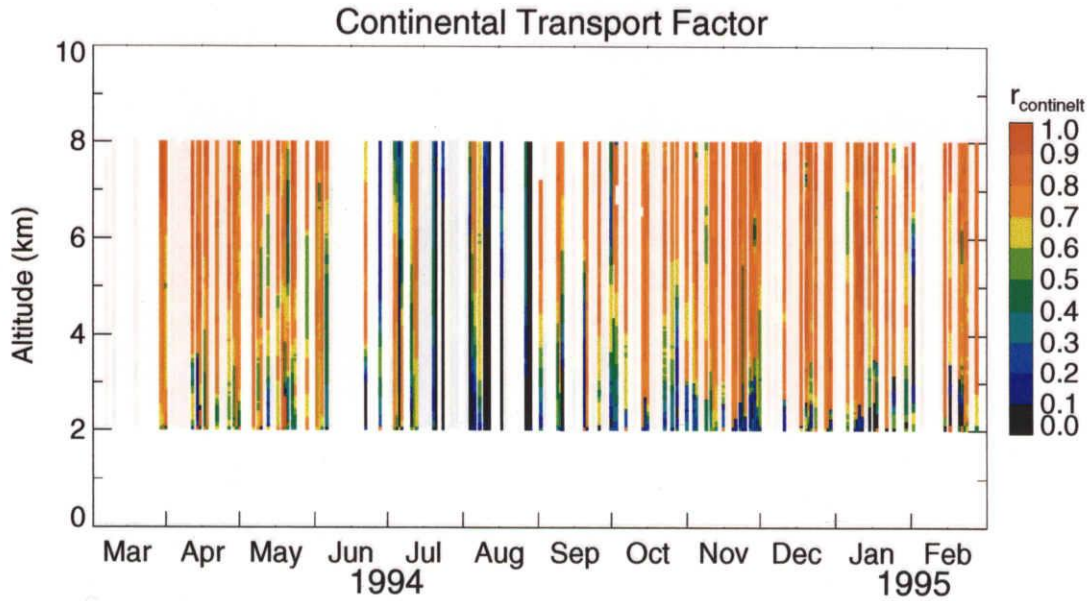

Fig. 4.19 temporal-vertical cross section of $r_{continent}$ (=fraction of the back trajectories passing over the continental area on the way to the lidar site) for the period March 1994 to February 1995.

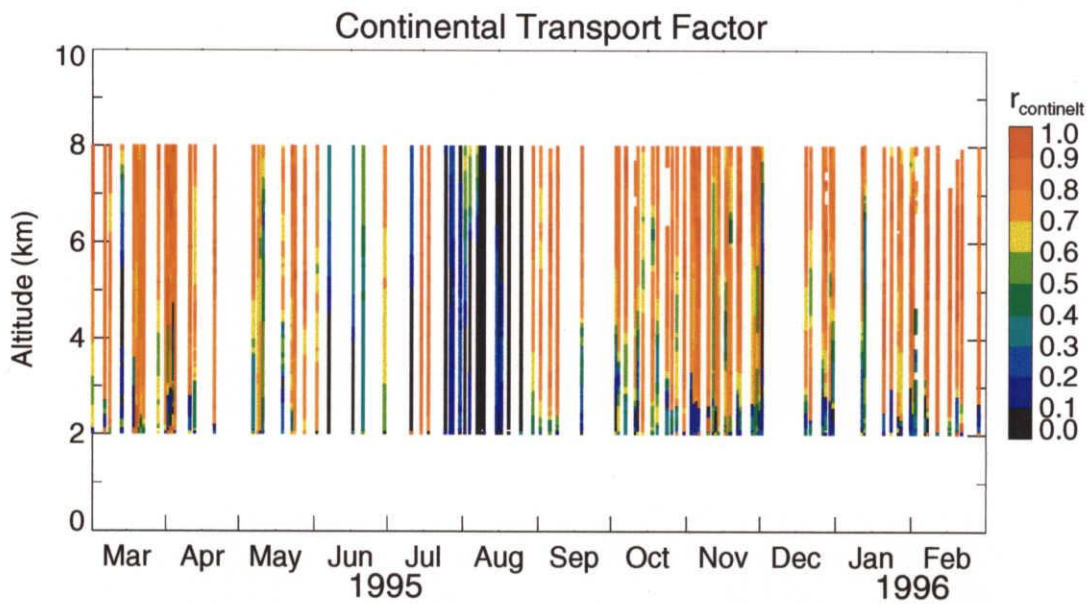

Fig. 4.20 Same as Fig. 4.19 but for the period March 1995 to February 1996.

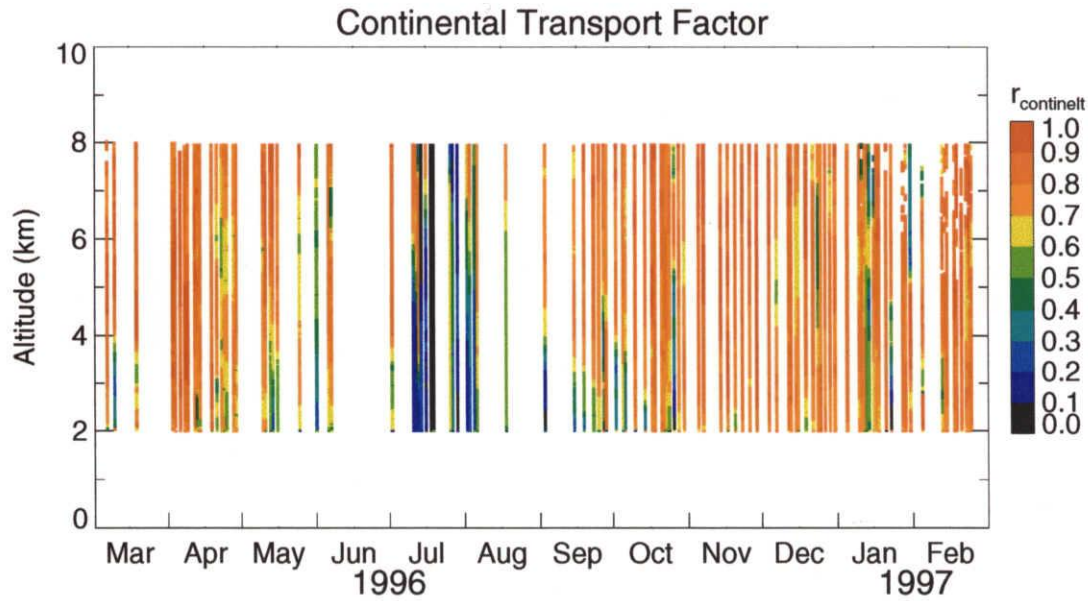

Fig. 4.21 Same as Fig. 4.19 but for the period March 1996 to February 1997.

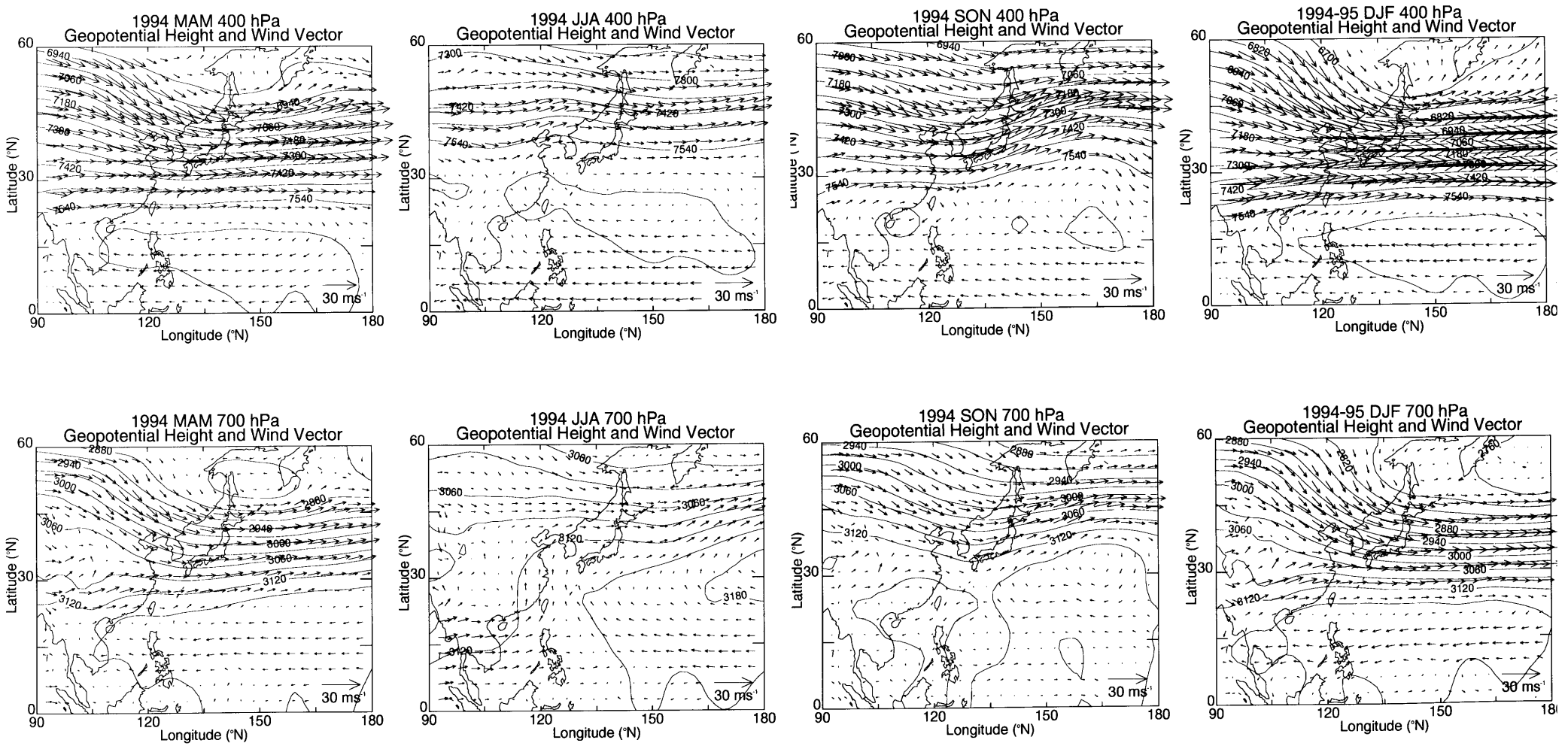

Fig. 4.22 Seasonal (three months) mean geopotential height (m) and wind vector at 400 hPa (upper panels) and 700 hPa (lower panels) in March 1994-Februa 1995. The altitudes of the pressure levels are approximately 7 km for 400 hPa and 3 km for 700 hPa.

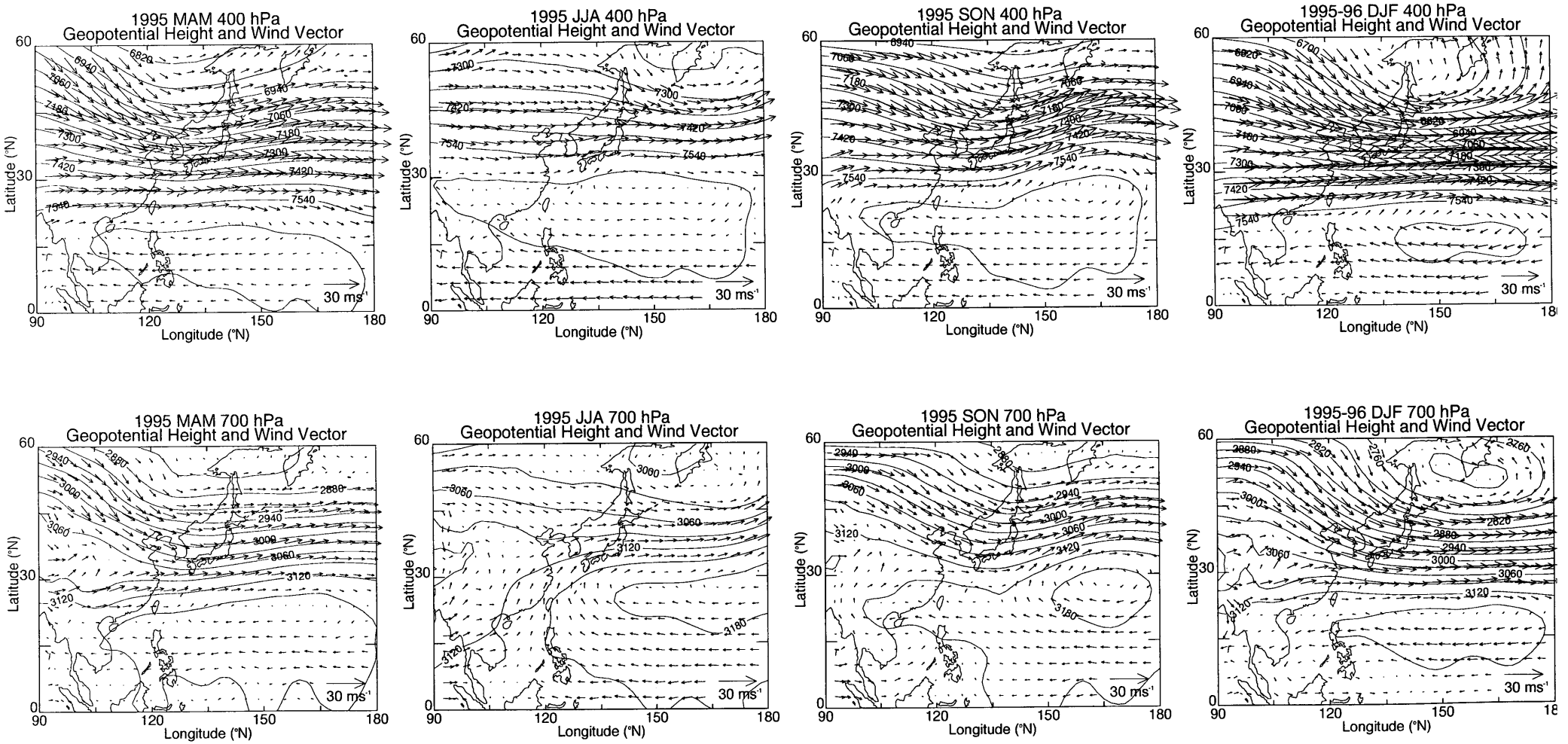

Fig. 4.23 Same as Fig. 4.22 but for the period March 1995 to February 1996.

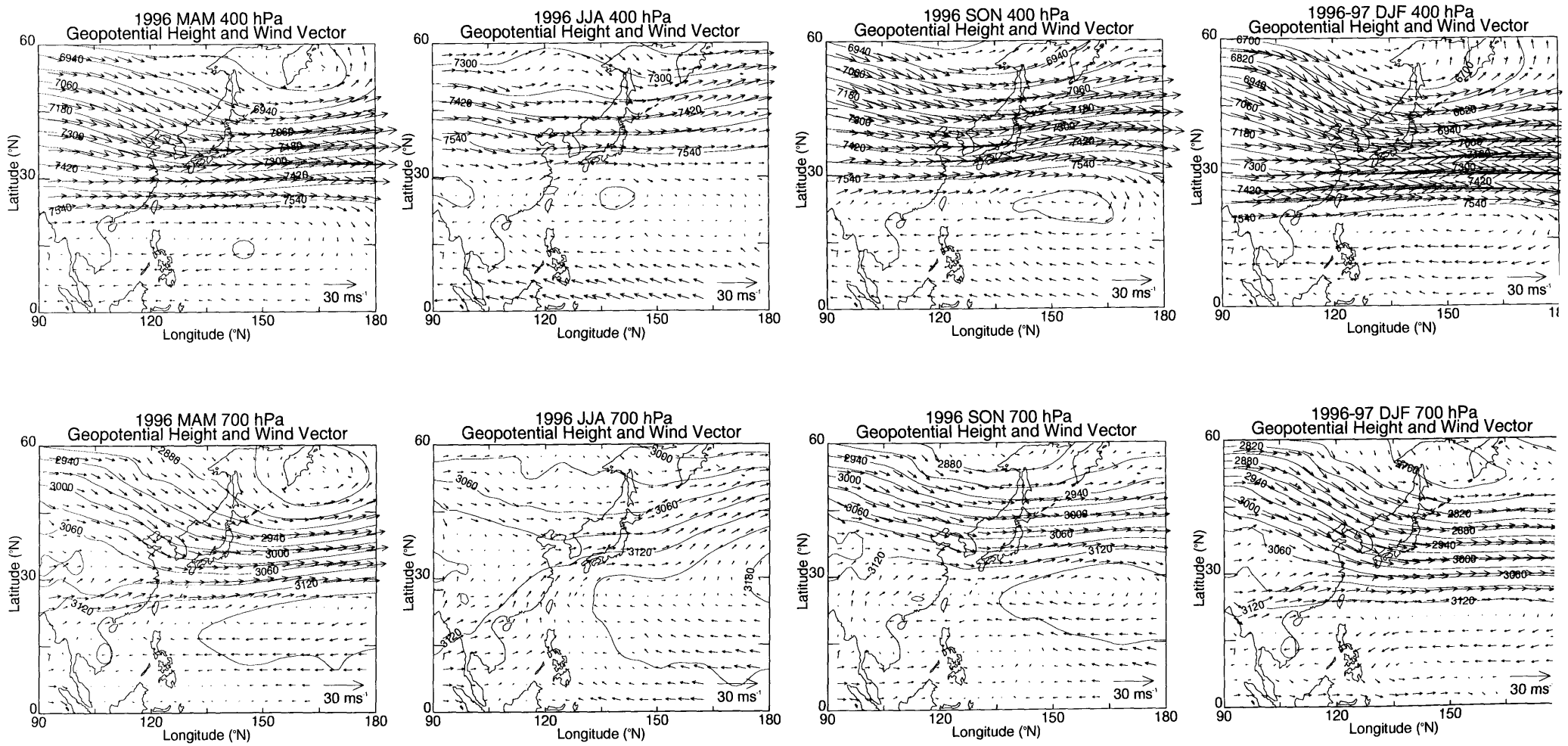

Fig. 4.24 Same as Fig. 4.22 but for the period March 1996 to February 1997.

Depolarization ratio as a function of the relative humidity for continental and maritime air

Fig. 4.25 shows the cumulative distributions of the aerosol backscattering coefficients, β_a, multiplied by the factor $r_{continent}$ (called the continental component) and $r_{maritime}$ (the maritime component) as a function of δ_a and RH. The continental components (left panels of Fig. 4.25) contained large fraction of high depolarization values ($\delta_a > 10\%$) over a wide range of RH. They also contained substantial fraction of low δ_a values. These suggest that both the water-soluble and insoluble particles were present in the continental air. On the other hand, the maritime components (right panels of Fig. 4.21) mainly consist of low depolarization values ($\delta_a < 5\%$) over a wide range of RH and small fraction of high δ_a values in dry air (RH < 40-60%), suggesting that water-soluble particles and water-soluble deliquescent particles were predominant in the maritime air. These distribution pattern for the two components are consistent with those expected for the aerosol chemical constituent from the sources; the data of high δ_a values with high RH values, which can only be produced by the water-insoluble particles, are almost categorized into the continental component. This result suggests that the transport pathways from the source areas (the Asian Continent and the Pacific Ocean) and the ambient relative humidity significantly controlled the aerosol depolarization ratio in the free troposphere over Nagoya.

It is interesting that high δ_a values (> 10%) were hardly found where the RH above 40% in the maritime component (right panels of Fig. 4.25). This might be due to the hysteresis effects of NaCl or $(NH_4)_2SO_4$ particles; the particles had deliquesced into droplets in moist air (> DRH) and remained phase below the DRH and above the CRH. Rood et al. (1989) have reported the ubiquitous existence of metastable droplets in the surface rural atmospheres at RH between 45 and 75%. To investigate the phase states of aerosol particles in the free troposphere more precisely, direct sampling and in-situ measurement are indispensable. Also, more accurate and finer temporal and spatial

resolution of meteorological data (humidity, wind, pressure, and temperature) are required to study the RH history of the air parcels during the transportation.

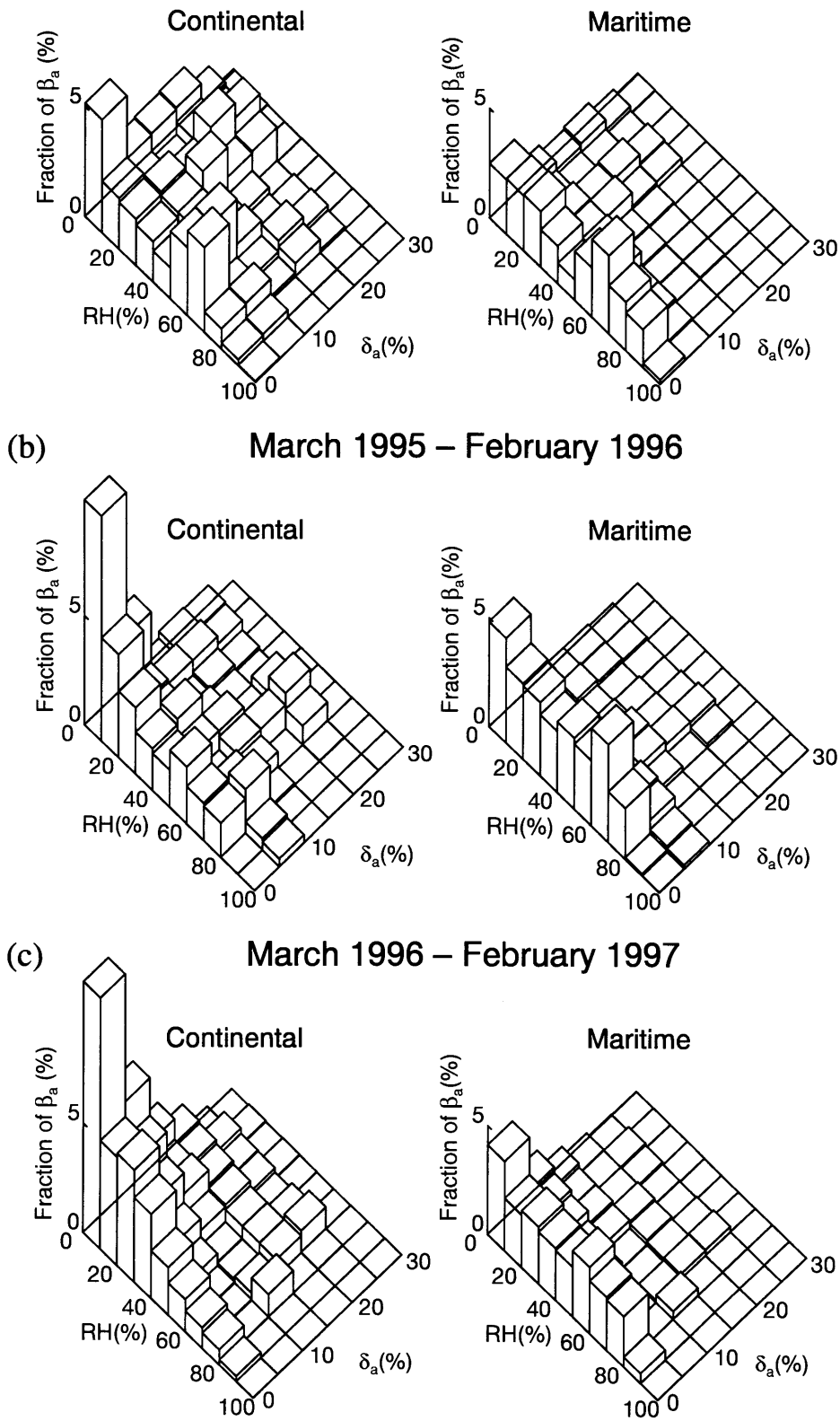

Fig. 4.25 Cumulative distributions of aerosol backscattering coefficients (β_a) multiplied by the factor $r_{continent}$ (Continental; left) and $r_{maritime}$ (Maritime; right) as a function of aerosol depolarization ratio (δ_a) and relative humidity (RH) between altitudes of 2 and 8 km for the period March 1994 to February 1997. Note that these factors ($r_{continent}$ and $r_{maritime}$) are derived assuming a uniformity of the source strength along the back trajectories.

Contribution of the continental and maritime air to the column amount of aerosols

Figure 4.26 shows the vertically integrated aerosol backscattering coefficients (IBC) between 2 and 8 km separated into two components (continental and maritime) in the same manner as the data shown in Fig. 4.25. The two components of the IBC are calculated by

$$IBC(Continental) = \int_{z_{bottom}}^{z_{top}} \beta_a(z) r_{continent}(z) dz \tag{4-2}$$

for the continental component and

$$IBC(Maritime) = \int_{z_{bottom}}^{z_{top}} \beta_a(z) r_{maritime}(z) dz \tag{4-3}$$

for the maritime component. We must emphasize these values are crude estimates because of the underlying assumption of uniformity of source strength along the trajectories.

We found that the spring maximum mainly consists of the continental component. It is conjectured a large amount of mineral dust particles that originated from Asian arid region were transported in the free troposphere to Japan, since the maximum occurrence of dust storms in the Asian arid region has been reported in the spring (Chun, 1996; Parungo et al., 1995) and westerly flow prevails over the Asian Continent (Figs 4.22a-24a). The other feature shown in Fig. 4.26 is that the predominance of maritime IBC over the continental IBC in the summer season. This was caused by changes in circulation pattern of the air mass over the lidar site due to the Pacific high pressure (Figs. 4.22b-24b). Thus, water-soluble particles originated from the Pacific Ocean probably predominated over the lidar site in this season. The ratios of the annual IBC for the two components (continental/maritime) were 2.0, 1.4, and 1.7 for each annual period in March 1994 to February 1997.

A summary of the observations is shown in Table 4.3. The IBC, IWVC, δ_a, RH, and $r_{continent}$ values show almost the same seasonal and altitude characteristics for the 3 year. However, information on the source strength and that on the vertical transport processes (e.g., transport from the planetary boundary layer to the free troposphere) are necessary to characterize the aerosol constituents and to evaluate the contributions of the aerosol sources on the lidar data quantitatively.

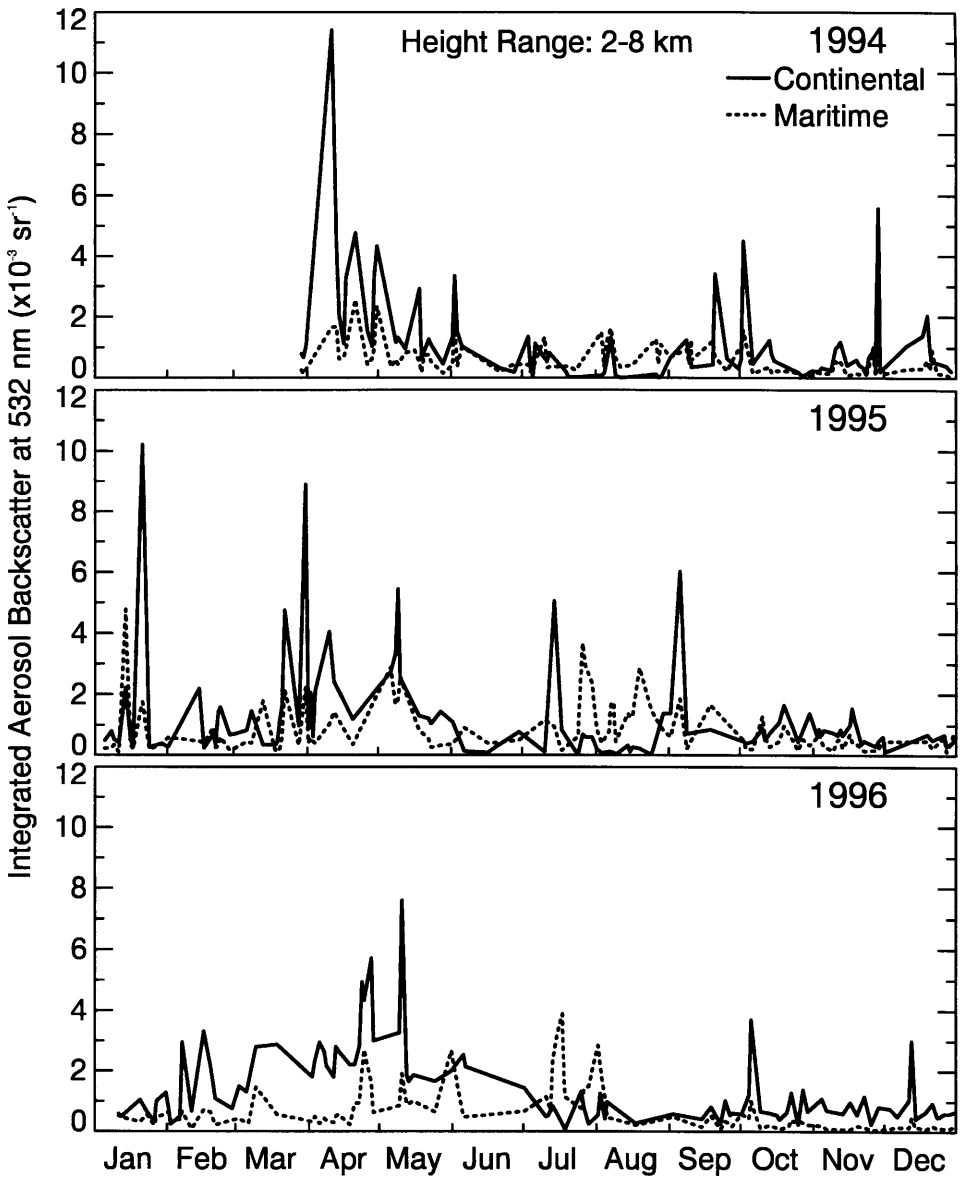

Fig. 4.26 Temporal variation of vertically integrated aerosol backscattering coefficients at 532 nm between 2 and 8 km weighted by the factors ($r_{continent}$ and $r_{maritime}$) that derived from the backward trajectories assuming a uniformity of the source strength along the trajectories. The solid lines indicate the continental component ($= \int_{z_{bottom}}^{z_{top}} \beta_a(z) r_{continent}(z) dz$) and the dotted lines indicate the maritime component ($= \int_{z_{bottom}}^{z_{top}} \beta_a(z) r_{maritime}(z) dz$).

Table 4.3 Three month mean of vertically integrated backscattering coefficients (IBC), vertically integrated water vapor content (IWVC), aerosol depolarization ratio (δ_a), relative humidity (RH) and continental transport factor ($r_{continent}$) at the altitude ranges of 4-8 km and 2-4 km over Nagoya for the period March 1994 to February 1997

Month		MAM			JJA			SON			DJF		
Year		1994	1995	1996	1994	1995	1996	1994	1995	1996	1994/5	1995/6	1996/7
Number of obs.		24	26	27	27	24	18	36	33	29	28	23	37
4-8km	IBC ($\times 10^{-3} sr^{-1}$)	1.43	1.28	1.42	0.31	0.48	0.72	0.70	0.74	0.69	0.89	0.59	0.74
	IWVC (kg/m^2)	0.58	0.61	0.61	4.78	3.45	3.73	1.44	1.17	0.95	0.21	0.26	0.25
	δ_a (%)	13	14	9	6	6	7	11	6	8	13	8	11
	RH (%)	14	17	14	31	26	24	21	15	15	10	12	12
	$r_{continent}$	0.83	0.80	0.82	0.44	0.28	0.52	0.79	0.81	0.84	0.83	0.81	0.84
2-4km	IBC ($\times 10^{-3} sr^{-1}$)	1.64	1.72	2.22	0.92	1.30	1.56	0.61	0.71	0.40	0.77	0.78	0.40
	IWVC (kg/m^2)	1.86	1.48	1.37	9.98	9.18	7.47	3.53	1.88	1.92	0.39	0.55	0.51
	δ_a (%)	9	9	6	4	2	1	4	4	4	4	4	7
	RH (%)	19	20	19	49	46	34	27	15	16	10	16	10
	$r_{continent}$	0.68	0.66	0.75	0.36	0.25	0.35	0.58	0.66	0.68	0.75	0.73	0.80

5 Conclusions

We have developed the Raman lidar system and the data analyzing procedure that simultaneously measure the vertical profiles of humidity, aerosol extinction, backscattering, and depolarization ratio in the troposphere. The Raman lidar technique allows us to study the aerosol optical properties and their relation to the ambient relative humidity in their natural state as well as their vertical and temporal structure in the free troposphere. We estimated the aerosol hygroscopicity (water-solubility) from the relation between the aerosol depolarization ratio and the relative humidity based on the humidity dependence of the particle shape (phase). The Raman lidar has an advantage over conventional Mie/Rayleigh lidar since it can measure the aerosol extinction and backscattering coefficients independently as well as the humidity, and the resulting aerosol extinction-to-backscatter ratio can be used to study the aerosol microphysical properties.

The measurements were carried out at Nagoya (35.1°N, 137.0°E) for the period March 1994 to February 1997 and total 332 vertical profiles were obtained. The observed results revealed the following aerosol optical characteristics related to the relative humidity and the transport pathways from the source areas.

The aerosol extinction (355 nm)-to-backscatter (532 nm) ratio showed relatively small values (3-17 sr) when the relative humidity was near or above the ice saturation point (> 90%RH with respect to ice), whereas they indicated a wide range of values (3-91 sr) in unsaturated air (≤ 90%RH with respect to ice). The values obtained near or above the ice saturation point were approximately consistent with that of the previous model calculation of cirrus cloud particles. This suggests that the extinction-to-backscatter ratio can be used for discrimination of the cirrus cloud particles from the other aerosol particles by combining with the other aerosol parameters measured with the lidar.

Temporal variations of the humidity and aerosol parameters were observed at the altitude range of 1.0-2.2 km during 30 minutes on April 17, 1994, in which the relation between the aerosol parameters and the relative humidity indicated that the total volume backscattering cross section and the sphericity of the aerosol particles were larger in moist air than in dry that. It was suggested that the observed relation was due to the presence of hygroscopic particles in this region since the relative humidities (13-38%) were near the phase transformation (crystallization or deliquescence) humidities of major tropospheric hygroscopic particles. At the altitude range of 2.2-3.5 km high depolarization ratios with the relative humidities of ~35% that were as high as the maximum at 1.0-2.2 km were observed, suggesting that the two altitude regions (1.0-2.2 km and 2.2-3.5 km) had different aerosol constituent (hygroscopicity) or the relative humidity history.

Seasonal and altitude variations of the aerosol optical properties and the relation to the relative humidity and the transport pathway were found as follows:

(1) The vertical distributions of aerosol depolarization ratio and humidity (both the water vapor mixing ratio and the relative humidity) frequently showed a steep vertical gradient between altitudes of 2 and 4 km throughout the year except for the summer, where the depolarization ratio sharply increased and the humidity decreased with height at almost the same level.

(2) The vertically integrated aerosol backscattering coefficients showed an annual maximum with sharp rises in the spring (March-May) in the 2-4 km and 4-8 km ranges. The three months mean in this season was larger than the annual mean by 1.6-2.2 times in the 2-4 km range and by 1.6-1.8 times in the 4-8 km range. The second maximum was found in the mid-late summer (July-August) for 2-4 km.

(3) Aerosol depolarization ratios as high as 25% were observed frequently in the 2-8 km region in the spring (MAM) and occasionally in the 4-8 km region in the autumn (SON) and winter (DJF). In the 4-8 km region these high values were observed with the relative humidities up to 80%, suggesting the presence of water-insoluble

particles such as mineral dusts in this region. Most of the air parcels in these regions had passed over the Asian Continent due to a westerly flow.

(4) Depolarization ratios less than 5% were predominant in the 2-8 km region in the summer (JJA) and in the 2-4 km region in the autumn over a wide range of relative humidities. In these regions, high depolarization ratios (δ_a > 10%) were observed only in relatively dry air (RH < 50%). These suggest the predominance of water-soluble particles (e.g., sulfuric acid droplets) and water-soluble deliquescent particles (e.g., sea-salt or ammonium sulfate particles) in these regions. The air parcels had mainly passed over the Pacific Ocean associated with the circulation of the Pacific high.

(5) Low depolarization ratios (δ_a < 5%) with low relative humidities (RH < 20%) were predominant in the winter, suggesting the predominance of water-soluble particles in this season. The air parcels had passed over the Asian Continent.

Our results suggest that the transportation pathways from the source areas (the Asian Continent and the Pacific Ocean) and the ambient relative humidity critically control the aerosol depolarization ratio in the free troposphere over Nagoya. The observed results showed that the aerosol optical properties (the backscattering ratio (coefficient) and the depolarization ratio) were vertically inhomogeneous and highly variable according to season. These data might be valuable to assess the effects of the free tropospheric aerosols on the Earth's atmospheric system, e.g., radiative transfer, cloud microphysical process, and global geochemical cycle. The assessment of the influence of these aerosol inhomogeneity and variability on the atmospheric processes is a future work. However, coincident measurement and comparison of lidar and in situ sampling data are indispensable for an interpretation and application of the lidar data that clarifies the physical and chemical characteristics of the free tropospheric aerosols. Furthermore, information on the aerosol source strengths and that on the vertical transport processes are necessary to characterize the aerosol constituents and to evaluate the contributions of the aerosol sources on the lidar data quantitatively.

Acknowledgements

I would like to thank Prof. Y. Iwasaka for giving me a chance to study the atmospheric aerosols and supervising my works. I also thank Prof. T. Shibata for giving me many important suggestions with regard to my works and critically reviewing the manuscript.

I thank Dr. S. A. Kwon, Mr. Y. S. Kim, and Mr. K. Tamura of our laboratory (Dr. Kwon is now at Hangyang University in Korea) for operating the Raman lidar with me. I am also grateful to Mr. H. Adachi of our laboratory for calculating the molecular depolarization ratio of the interference filter utilized in this study and suggesting the correction method for deriving the aerosol depolarization ratio from the lidar data. Thanks are offered to Mr. M. Watanabe and the other members of our laboratory for help with the Radiosonde measurements.

I am indebted to Dr. T. Murayama of Tokyo University of Mercantile Marine for enlightening me on the use of depolarization ratio for studying the hygroscopic properties of the tropospheric aerosols. I wish to express my thanks to Dr. T. Nagai of Meteorological Research Institute for the provision of the global objective analysis (GANAL) data. I also thank technical officers Mr. M. Nagatani and Mr. H. Nakada for making the photon counter and the other devices of the lidar system. And also to Dr. K. Matsunaga, Dr. K. Osada, Dr. M. Hayashi, Mr. T. Ojio, Mr. K. Hara, Ms. M. Kido, Ms. Y. Inomata, Mr. K. Lee, Mr. S. Ishii, Mr. Y. Okuhara, Mr. M. Araki, Mr. S. Furuike, Mr. T. Ohashi, Ms. C. Nishita, and Ms. A. Yabe, I express my great thanks.

This research was supported by Japan Ministry of Education, Science, Sports and Culture (Grant-in-Aid for Creative Fundamental Research, Studies of Global Environmental Change with special reference to Asia and Pacific Regions, led by Professors Tamura, S., University of Tokyo, Matsuno, T., Hokkaido University, and Tanaka, M., Tohoku University; Grant number: 02NP0101, 03NP0201, 04NP0201, and 05NP0201).

Appendix A Calculation of the Raman backscattering cross section of oxygen

The absolute wavenumber of the Stokes Raman lines is expressed as

$$\tilde{\nu} = \tilde{\nu}_0 - \Delta\tilde{\nu} \ [\mathrm{m}^{-1}], \tag{A-1}$$

where $\tilde{\nu}_0$ is the wavenumber of the incident radiation and $\Delta\tilde{\nu}$ is the wavenumber shift of the Raman scattering. The wavenumber shifts associated with the fundamental vibration transition $v = 0 \rightarrow v = 1, \Delta J = 0, \pm 2$ are expressed as follows (Long, 1977): For Q-branches ($\Delta J = 0$) the wavenumber shifts are given by

$$\Delta\tilde{\nu}_Q = \Delta G + (B_1 - B_0)J(J+1) \ [\mathrm{m}^{-1}], \tag{A-2}$$

where $J = 0, 1, 2, \ldots$, and those for the S-branch ($\Delta J = +2$) are given by

$$\Delta\tilde{\nu}_S = \Delta G + 2B_1 - (3B_1 + B_0)J + (B_1 - B_0)J^2 \ [\mathrm{m}^{-1}], \tag{A-3}$$

where $J = 0, 1, 2, \ldots$, and those for the O-branch ($\Delta J = -2$) are given by

$$\Delta\tilde{\nu}_O = \Delta G + 6B_1 - (5B_1 - B_0)J + (B_1 - B_0)J^2 \ [\mathrm{m}^{-1}] \tag{A-4}$$

where $J = 2, 3, \ldots$. Here, $\Delta G = G(1) - G(0)$ is the difference of the vibration term $G(v)$ between the ground vibrational level and the first excited vibrational level, which equals to the wavenumber shift associated with the vibrational transition of $v = 0 \rightarrow v = 1$, and B_v is given by $B_v = B_e - \alpha_e(v + 1/2)$ where the subscript e refers to the equilibrium configuration. For oxygen molecule, ΔG=155638.1 [m^{-1}],

B_e=144.563 [m^{-1}], and α_e =1.59+6.41×10^{-3}(v+1/2)^2-2.85×10^{-4}(v+1/2)^3 [m^{-1}] (Huber and Herzberg, 1979).

The differential backscattering cross sections for the Raman lines are calculated by Placzek polarizability theory (Kobayashi and Inaba, 1972). For Q-branch the cross sections are given by

$$\left(\frac{d\sigma(\pi)}{d\Omega}\right)_Q = \frac{(2\pi)^4(\tilde{\nu}_0-\tilde{\nu}_j)^4 b_j^{\,2} g_J(2J+1)e^{-hc\tilde{\nu}_j/kT}}{1-e^{-hc\tilde{\nu}_j/kT}} \frac{}{\sum_J g_J(2J+1)e^{-hc\tilde{\nu}_j/kT}} \left(\alpha'^2 + \frac{J(J+1)}{(2J-1)(2J+3)}\frac{7}{45}\gamma'^2\right)$$

[m^2 sr^{-1}], (A-5)

and those for S- and O-branches are given by

$$\left(\frac{d\sigma(\pi)}{d\Omega}\right)_{O,S} = \frac{(2\pi)^4(\tilde{\nu}_0-\tilde{\nu}_j)^4 b_j^{\,2} X_J g_J(2J+1)e^{-hc\tilde{\nu}_j/kT}}{1-e^{-hc\tilde{\nu}_j/kT}} \frac{}{\sum_J g_J(2J+1)exp^{-hc\tilde{\nu}_j/kT}} \frac{7}{45}\gamma'^2 \text{ [m}^2\text{ sr}^{-1}\text{]}, \quad \text{(A-6)}$$

where

$$X_J = \frac{3}{2}\frac{(J+1)(J+2)}{(2J+1)(2J+3)} \quad \text{(A-7)}$$

for S-branch and

$$X_J = \frac{3}{2}\frac{J(J-1)}{(2J+1)(2J-1)} \quad \text{(A-8)}$$

for O-branch. Here $\tilde{\nu}_j$ is the wavenumber associated with the vibrational-rotational transition that is equal to $\Delta\tilde{\nu}$, $b_j(=[h/(8\pi^2 c\tilde{\nu}_j)]^{1/2})$ is the zero-point vibrational amplitude of j-th vibrational mode, g_J is the nuclear spin statistical weight, J is the initial rotational-angular-momentum quantum number, h is the Planck's constant, c is the speed of light, k is the Boltzmann's constant, T is the temperature, α'^2 and γ'^2 are the isotropic and anisotropic parts of the derived polarizability tensor associate with

the normal coordinate, respectively. For oxygen, g_J is 1 for odd J and 0 for even J (e.g., Long, 1977) and $g_j\alpha'^2 = 0.27\times10^{-24}N_A$ and $g_j\gamma'^2 = 1.08\times10^{-37}N_A$ [m^{4}kg^{-1}] (Inaba, 1976) where g_j is the degeneracy of the j-th vibrational mode, and N_A is the Avogadro's number.

Appendix B Trajectory analysis

The procedure for calculating the isentropic trajectory is described below.

Data set

The meteorological data used in the calculation of the trajectory were the global objective analysis data (GANAL (or GAPLX after March 1996)) supplied with the Japan Meteorological Agency. The data consist of geopotential height, horizontal wind, temperature and humidity at 16 (18 after March 1996) pressure levels. The pressure levels are Surface, 1000, (925,) 850, 700, (600,) 500, 400, 300, 250, 200, 150, 100, 70, 50, 30, 20, and 10 hPa. The humidity data is available below 300 hPa. The time resolution is 12 h (6 h after March 1996). The horizontal resolution is 1.875° (1.25° after March 1996) for latitude and longitude.

Surface elevation data (ETOPO5) was supplied with NOAA National Geophysical Data Center. The original data consist of land and sea floor elevations on a 5-minute latitude/longitude grid. We used this data after degrading and adjusting to the resolution of GANAL or GAPLX data.

Interpolation of gridded data

The meteorological parameter at a point is obtained by interpolating the grid data. The interpolations are made by log-linearly for vertical, bilinearly for horizontal, and linearly for time. A meteorological parameter $X_{\lambda\phi\theta t}$ at an arbitrary point $(\lambda,\phi,\theta(z),t)$, where λ is the longitude, ϕ is the latitude, θ is the potential temperature, z is the height, and t is the time, is calculated by following procedure.

(1) Sixteen grid points $(\lambda_i,\phi_i,\theta_i,t_i)(i=1,2)$ surrounding the point (λ,ϕ,θ,t) are selected and the parameters $X_{\lambda_i\phi_i\theta_i t_i}$ are obtained from the grid data.

(2) Eight parameters $X_{\lambda_i\phi_i\theta t_i}$ on the isentropic surface θ are calculated from the sixteen parameters by log-linear interpolation for potential temperature as

$$X_{\lambda_i\phi_i\theta\, t_i} = \frac{X_{\lambda_i\phi_i\theta_2 t_i}\, ln(\theta_2/\theta) + X_{\lambda_i\phi_i\theta_1 t_i}\, ln(\theta/\theta_1)}{ln(\theta_2/\theta_1)}. \tag{B-1}$$

(3) Four parameters $X_{\lambda_i\phi_i\theta\, t}$ at the time t are calculated from the eight parameters by linear interpolation for time as

$$X_{\lambda_i\phi_i\theta\, t} = \frac{X_{\lambda_i\phi_i\theta t_2}(t_2 - t) + X_{\lambda_i\phi_i\theta t_1}(t - t_1)}{t_2 - t_1}. \tag{B-2}$$

(4) Finally the parameter $X_{\lambda\phi\theta\, t}$ is obtained from the four parameters using bilinear interpolation for horizontal space as

$$X_{\lambda\phi\theta\, t} = \frac{X_a(\phi_2 - \phi) + X_b(\phi - \phi_1)}{\theta_2 - \theta_1}, \tag{B-3}$$

where $$X_a = \frac{X_{\lambda_1\phi_1\theta\, t}(\lambda_2 - \lambda) + X_{\lambda_2\phi_1\theta\, t}(\lambda - \lambda_1)}{\lambda_2 - \lambda_1}$$

and $$X_b = \frac{X_{\lambda_1\phi_2\theta\, t}(\lambda_2 - \lambda) + X_{\lambda_2\phi_2\theta\, t}(\lambda - \lambda_1)}{\lambda_2 - \lambda_1}.$$

The potential temperature is calculated by $\theta = T(1000/P)^{R_d/C_p}$ [K], where T is the temperature [K], P is the atmospheric pressure [hPa], R_d is the gas constant for dry air (=287.04 J kg^{-1} K^{-1}), and C_p is the specific heat capacity of dry air at constant pressure (=1005.7 J kg^{-1} K^{-1}).

Calculation of trajectory

The trajectory of the air parcel is calculated on the isentropic surface by using the fourth-order Runge-Kutta scheme. The air parcel at a position $\boldsymbol{x}(t_i)$ is advected to the next position by using the following equation.

$$x(t_{i+1}) = x(t_i) + \Delta t\left(\frac{1}{6}v_1 + \frac{1}{3}v_2 + \frac{1}{3}v_3 + \frac{1}{6}v_4\right), \tag{B-4}$$

where

$$v_1 = v(x(t_i), t_i),$$

$$v_2 = v(x(t_i) + v_1 \Delta t/2, t_i + \Delta t/2),$$

$$v_3 = v(x(t_i) + v_2 \Delta t/2, t_i + \Delta t/2),$$

and $v_4 = v(x(t_i) + v_3 \Delta t, t_i + \Delta t)$.

Here, $v(x,t)$ is the horizontal wind vector on the isentropic surface and Δt is the time step of the calculation. We used $\Delta t = -1$ h for the calculation of the backward trajectories.

Isentropic analysis assumes adiabatic and inviscid motion of air parcel. This assumption is unsuitable in saturated moist air or in the planetary boundary layer where diabatic processes or turbulent mixing are important. In order to reduce the inaccuracies of the isentropic analysis, we terminated the computation of the trajectory if the air parcel intersected the vertically unstable layer ($\partial\theta/\partial z < 0$) or Earth's surface, or the air was saturated with respect to water or ice.

Since the lidar observes the finite volume of air that passes over the lidar site during the observation period, the air parcels in the volume can be transported from different areas due to the spatial inhomogeneity of the wind field. For this reason and in order to improve the statistical significance of the results, we calculated twenty-five trajectories whose initial positions were located at around the lidar site (35.1°N, 137.0°E) with horizontal interval of 0.5° for longitude-latitude (5×5) on the same isentropic surface.

7 References

Adachi, H., T. Shibata, Y. Iwasaka, and M. Fujiwara, 1998, Mixing State of Liquid and Solid Polar Stratospheric Clouds: Analysis of Lidar Returns Measured at Ny-Ålesund, Spitsbergen, submitted to *Appl. Opt.*

Albrecht, B. A., 1989, Aerosols, Cloud Microphysics, and Fractional Cloudiness, *Science*, **245**, 1227-1230.

Ångström, A, 1964, The parameters of atmospheric turbidity, *Tellus*, **16**, 64-75.

Ansmann, A., M., Riebesell, and C. Weitkamp, 1990, Measurement of atmospheric aerosol extinction profiles with a Raman lidar, *Opt. Lett.*, **15**, 746-748.

Ansmann, A., M., Riebesell, U. Wandinger, C. Weitkamp, E. Voss, W. Lahmann, and W. Michaelis, 1992a, Combined Raman elastic-backscatter LIDAR for vertical profiling of moisture, aerosol extinction, backscatter, and LIDAR ratio, *Appl. Phys.*, **B55**, 18-28.

Ansmann, A., U. Wandinger, M., Riebesell, C. Weitkamp, and W. Michaelis, 1992b, Independent measurement of extinction and backscatter profiles in cirrus cloud by using a combined elastic-backscatter lidar, *Appl. Opt.*, **31**, 7113-7131.

Asano, S. and M. Sato, 1980, Light scattering by randomly oriented spheroidal particles, *Appl. Opt.*, **19**, 962-974.

Baumgardner, D., and B. Huebert, 1993, The airborne aerosol inlet workshop: Meeting report, *J. Aerosol Sci.*, **24**, 835-845.

Bohren, C. F. and D. R. Huffman, 1983, *Absorption and Scattering of Light by Small Particles*, Wiley, New York, 530pp.

Boucher, O. and T. L. Anderson, 1995, General circulation model assessment of the sensitivity of direct climate forcing by anthropogenic sulfate aerosols to aerosol size and chemistry, *J. Geophys. Res.*, **100**, 26117-26134.

Bribes, J. L., R. Gaufrès, M. Monan, M. Lapp, and C. M. Penny, 1976, Raman band contours for water vapor as a function of temperature, *App. Phys. Lett.*, **28**, 336-337.

Bucholtz, A., 1995, Rayleigh-scattering calculations for the terrestrial atmosphere, *Appl. Opt.*, **34**, 2765-2773.

Buck, A. L., 1981, New Equations for Computing Vapor Pressure and Enhancement Factor, *J. App. Meteorol.*, **20**, 1527-1532.

Charlson, R. J., S. E. Schwartz, J. M. Hales, R. D. Cess, J. A. Coakley, Jr., J. E. Hansen, and D. J. Hofmann, 1992, Climate Forcing by Anthropogenic Aerosols, *Science*, **255**, 423-430.

Chen, J.-P., 1994, Theory of Deliquescence and Modified Köhler Curves, *J. Atmos. Sci.*, **51**, 3505-3516.

Chun, Y. K., 1996, Long range transport of Yellow Sand with special emphasis on the dust rise condition in the source regions, Doctoral thesis, Seoul National University, 129pp. (In Korean).

Coakely, J. A. Jr., R. D. Cess, and F. B. Yurevich, 1983, The Effects of Tropospheric Aerosols on the Earth's Radiation Budget: A Parameterization for Climate Models, *J. Atmos. Sci.*, **30**, 116-138.

Cohen, M. D., R. C. Flagan, and J. H. Seinfeld, 1987, Studies of Concentrated Electrolyte Solutions Using the Electrodynamic Balance. 3. Solute Nucleation, *J. Phys. Chem.*, **91**, 4583-4590.

Cooney, J., 1970, Remote Measurements of Atmospheric Water Vapor Profiles Using the Raman Component of Laser Backscatter, *J. App. Meteorol.*, **9**, 182-184.

Cooper, D. I., W. E. Eichinger, S. Barr, W. Cottingame, M. V. Hynes, C. F. Keller, C. F. Lebeda, and D. A. Poling, 1996, High-Resolution Properties of the Equatorial Pacific Marine Atmospheric Boundary Layer from Lidar and Radiosonde Observations, *J. Atmos. Sci.*, **53**, 2054-2075.

Cooper, D. W., J. W. Davis, and R. L. Byers, 1974, Measurements of depolarization by dry and humidified salt aerosols using lidar analogue, *Aerosol Science*, **5**, 117-123.

Dentener, F. J., G. R. Carmichael, Y. Zhang, J. Lelieveld, and P. J. Crutzen, 1996. Role of mineral aerosol as a reactive surface in the global troposphere, *J. Geophys. Res.*, **101**, 22869-22889.

Dlugi, R., S. Jordan, and E. Lindemann, 1981, The heterogeneous formation of sulfate aerosols in the atmosphere, *J. Aerosol Sci.*, **12**, 185-197.

Duce, R. A., C. K. Unni, B. J. Ray, J. M. Prospero, and J. T. Merrill, 1980, Long range transport of soil dust from Asia to tropical North Pacific: Temporal variability, *Science*, **209**, 1522-1524.

Duce, R. A., 1991, Sources, distributions, and fluxes of mineral aerosols and their relationship to climate, In *Aerosol Forcing of Climate*, edited by R. J. Charlson and J. Heitzenberg, John Wiley, New York, pp.43-72.

Fernald, F. G., 1984, Analysis of atmospheric lidar observations: some comments, *Appl. Opt.*, **23**, 652-653.

Ferrare, R. A., S. H. Melfi, D. N. Whiteman, K. D., Evans, F. J. Schmidlin, and D. O'C. Starr, 1995, A Comparison of Water Vapor Measurements Made by Raman Lidar and Radiosondes, *J. Atmos. Ocean. Tech.*, **12**, 1177-1195.

Ferrare, R. A., S. H., Melfi, D. N. Whiteman, K. D. Evans, M. Poellot, and Y. J. Kaufmann, 1998, Raman lidar measurements of aerosol extinction and backscattering 2. Derivation of aerosol refractive index, single-scattering albedo, and humidification factor using Raman lidar and aircraft size distribution measurements, *J. Geophys. Res.*, **103**, 19673-19689.

Han, J.-H. and S. T. Martin, 1999, Heterogeneous nucleation of the efflorescence of $(NH_4)_2SO_4$ particles internally mixed with Al_2O_3, TiO_3, and ZrO_2, *J. Geophys. Res.*, **104**, 3543-3553.

Hänel, G., 1976, The properties of atmospheric aerosol particles as function of the relative humidity at thermodynamic equilibrium with the surrounding atmosphere, *Advances in Geophysics*, **19**, 73-188.

Hatakeyama, S., K. Murano, H. Mukai, F. Sakamaki, H. Bandow, I. Watanabe, M. Yamato, S. Tanaka, and H. Akimoto, 1997, SO_2 and Sulfate Aerosols over the Seas between Japan and the Asian Continent, *J. Aerosol Res., Japan*, **12**, 91-95.

Haury, G., S. Jordan, and C. Hofmann, 1978, Experimental investigation of the aerosol-catalyzed oxidation of SO_2 under atmospheric conditions, *Atmos. Environ.*, **12**, 281-287.

Hayasaka, T., Y. Meguro, Y. Sasano, and T. Takamura, 1998, Stratification and size distribution of aerosols retrieved from simultaneous measurements with lidar, a sunphotometer, and an aureolemeter, *App. Opt.*, **37**, 961-970.

Heitzenberg, J., 1993, Fine particles in the global troposphere A review, *Tellus*, **41B**, 149-160.

Hoell, J. M., D. D., Davis, S. C. Liu, R. E. Newell, H. Akimoto, R. J. McNeal, and R. J. Bendura, 1997, The Pacific Exploratory Mission-West Phase B: February-March, 1994, *J. Geophys. Res.*, **102**, 28223-28239.

Holland, A. C. and G. Gagne, 1970, The Scattering of Polarized Light by Polydisperse Systems of Irregular Particles, *Appl. Opt.*, **9**, 1113-1121.

Huber, K. P. and G. Herzberg, 1979, *Molecular Spectra and Molecular Structure IV. Constants of Diatomic Molecules*, Van Nostrand Reinhold, New York, 716pp.

Ikegami, M., K. Okada, Y. Zaizen, and Y. Makino, 1993, Aerosol Particles in the Middle Troposphere over the Northern Pacific, *J. Meteorol. Soc. Japan*, **71**, 517-528.

Inaba, H., 1976, Detection of Atoms and Molecules by Raman and Resonance Fluorescence, In *Laser Monitoring of the Atmosphere*, edited by E. D. Hinkley, Springer-Verlag, Berlin, pp. 153-236.

Iwasaka, Y., M. Yamato, R. Imasu, and A. Ono, 1988, Transport of Asian dust (KOSA) particles; importance of weak KOSA events on the geochemical cycle of soil particles, *Tellus*, **40B**, 494-503.

Kent, G. S., G. K. Yue, U. O. Farrukh, and A. Deepak, 1983, Modeling of atmospheric aerosol backscatter at CO_2 laser wavelengths. 1: Aerosol properties modeling techniques, and associated problems, *Appl. Opt.*, **22**, 1655-1665.

Klett, J. D., 1981, Stable analytical inversion solution for processing lidar returns, *Appl. Opt.*, **20**, 211-220.

Kobayashi, T. and H. Inaba, 1972, Spectral Analysis of Air Pollution with Laser Radar Techniques, *Journal of the spectroscopic society of Japan*, **21**, 295-315 (In Japanese).

Koch, S. E., P. B. Dorian, R. Ferrare, S. H. Melfi, W. C. Skillman, and D. Whiteman, 1991, Structure of an Internal Bore and Dissipating Gravity Current as Revealed by Raman Lidar, 1991, *Mon. Wea. Rev.*, **119**, 857-887.

Koepke, P., and M. Hess, 1988, Scattering functions of tropospheric aerosols: the effects of nonspherical particles, *Appl. Opt.*, **27**, 2422-2430.

Kuik, F., P. Stammers, and J. W. Hovenier, 1991, Experimental determination of scattering matrices of water droplets and quartz particles, *Appl. Opt.*, **30**, 4872-4881.

Kwon, S. A., Y. Iwasaka, T. Shibata, and H. Nakane, 1997, Application of Discriminant Analysis to Classify the Properties of Atmospheric Aerosol Particles Measured by a Lidar in Spring, *J. Aerosol Res., Japan*, **12**, 209-219 (In Japanese).

Lacis, A. A., and M. I. Mischenko, 1995, Climate Forcing, Climate Sensitivity, and Climate Response: A Radiative Modeling Perspective on Atmospheric Aerosols, In *Aerosol Forcing of Climate*, edited by R. J. Charlson and J. Heitzenberg, John Wiley, New York, pp.11-42.

Larsen, J. C., E. W. Chiou, W. P. Chu, M. P. McCormick, L. R. McMaster, S. Oltmans, and D. Rind, 1993, A Comparison of the Stratospheric Aerosol and Gas Experiment II Tropospheric Water Vapor to Radiosonde Measurements, *J. Geophys. Res.*, **98**, 4897-4917.

Liao, H. and J. H. Seinfeld, 1998, Radiative forcing by mineral dust aerosols: sensitivity to key variables, *J. Geophys. Res.*, **103**, 31637-31645.

Long, D. A., 1977, *Raman Spectroscopy*, McGraw-Hill, London, 179pp.

Melfi, S. H., J. D., Lawrence, Jr., and M. P. McCormick, 1969, Observation of Raman scattering by water vapor in the atmosphere, *Appl. Phys.Lett.*, **15**, 295-297.

Melfi, S. H., 1972, Remote measurements of the atmosphere using Raman scattering, *Appl. Opt.*, **11**, 1605-1610.

Melfi, S. H. and D. N. Whiteman, 1985, Observation of lower-atmospheric moisture structure and its evolution using a Raman lidar, *Bull. Am. Meteor. Soc.*, **66**,1288-1292.

Melfi, S. H., D. N. Whiteman, and R. A., Ferrare, 1989, Observations of atmospheric fronts using Raman lidar moisture measurements, *J. Appl. Meteorol.*, **28**, 789-806.

Merrill, J. T., M. Uematsu, and R. Bleck, 1989, Meteorological analysis of log range transport of mineral aerosols over Northern Pacific, *J. Geophys. Res.*, **94**, 8584-8598.

Mischenko, M. I., A. A. Lacis, B. E. Carlson, and L. D. Travis, 1995, Nonsphericity of dust-like tropospheric aerosols: implications for aerosol remote sensing and climate modeling, *Geophys. Res. Lett.*, **22**, 1077-1080.

Mishchenko, M. I., L. D. Travis, and D. W. Mackowski, 1996, T-matrix computations of light scattering by nonspherical particles: a review, *J. Quant. Spectrosc. Radiat. Transfer*, **55**, 535-575.

Mischenko, M. I., L. D. Travis, R. A. Kahn and R. A. West, 1997, Modeling phase functions for dustlike tropospheric aerosols using shape mixture of randomly oriented polydisperse spheroids, *J. Geophys. Res.*, **102**, 16831-16847.

Mischenko, M. I. and K. Sassen, 1998, Depolarization of lidar returns by small ice crystals: An application to contrails, *Geophys. Res. Lett.*, **25**, 309-312.

Mozurkewich, M. and J. G. Calvert, 1988, Reaction probability of N_2O_5 on Aqueous aerosols, *J. Geophys. Res.*, **93**, 15889-15896.

Msibi, I. M., Y. Li, J. P. Shi, and R. M. Harrison, 1994, Determination of heterogeneous reaction probability using deposition profile measurement in annular reactor; Application to the N_2O_5/H_2O reaction, *J. Atm. Chem.*, **18**, 291-300.

Murayama, T., M. Furushima, A. Oda, N. Iwasaka, and K. Kai, 1996, Depolarization ratio measurements in the atmospheric boundary layer by lidar in Tokyo, *J. Meteorol. Soc. Japan*, **74**, 571-578.

Nakajima, T., M. Tanaka, M. Yamano, M. Shiobara, K. Arao, and Y. Nakainishi, 1989, Aerosol Optical Characteristics in the Yellow Sand Events Observed in May, 1982 at Nagasaki - Part II Models, *J. Meteorol. Soc. Japan*, **67**, 279-291.

Okada, K., 1983, Nature of Individual Hygroscopic Particles in the Urban Atmosphere, *J. Meteorol. Soc. Japan*, **61**, 727-736.

Onasch, T. B., R. L. Siefert, S. D. Brooks, A. J. Prenni, B. Murray, M. A. Wilson, and M. A. Tolbert, 1999, Infrared spectroscopic study of the deliquescence and efflorescence of ammonium sulfate aerosol as a function of temperature, *J. Geophys. Res.*, **104**, 21317-21326.

Orr, C. Jr., F. K. Hurd, and W. J. Corbett, 1958, Aerosol size and relative humidity, *J. Colloid Sci.*, **13**, 472-482.

Pandis S. N., A. S. Wexler, and J. H. Seinfeld, 1995, Dynamics of Tropospheric Aerosols, *J. Phys. Chem.*, **99**, 9646-9659.

Parungo, F., Y. Kim C. Zhu, J. Harris, R. Schnell, X. Li, D. Yang, X. Fang, M. Zhou, Z. Chen, and K. Park, 1995, *Asian dust storms and their effects on radiation and climate*, STC rep. 2906, Natl. Oceanic and Atmos. Admin. Air Resources Lab., Silver Spring, MD, 56pp.

Perry, R. J., A. J. Hunt, and D. R. Huffman, 1978, Experimental determinations of Muller scattering matrices for nonspherical particles, *Appl. Opt.*, **17**, 2700-2710.

Pilinis, C. and X. Li, 1998, Particle shape and internal in homogeneity effects on the optical properties of tropospheric aerosols of relevance to climate forcing, *J. Geophys. Res.*, **103**, 3789-3800.

Pollack, J. B. and J. N. Cuzzi, 1980, Scattering by Nonspherical Particles of Size Comparable to a Wavelength: A New Semi-Empirical Theory and Its Application to Tropospheric Aerosols, *J. Atmos. Sci.*, **37**, 868-881.

Porter J. N., A. D. Clarke, G. Ferry, and R. F. Pueschel, 1992, Aircraft studies of size-size dependent aerosol sampling through inlets, *J. Geophys. Res.*, **97**, 3815-3824.

Prospero, J. M., R. J. Charlson, V. Mohnen, R. Jaenicke, A. C., Delany, J. Moyers, W. Zoller, and K. Rahn, 1983, The atmospheric aerosol system: An overview, *Rev. Geophys. Space Phys.*, **12**, 1607-1629.

Prospero, J. M. and D. L. Savoie, 1989, Effect of continental sources on nitrate concentrations over the Pacific Ocean, *Nature*, **339**, 687-689.

Pueschel, R. F., J. M. Livingston, G. V. Ferry, and T. E. DeFelice, 1994, Aerosol abundance and optical characteristics in the Pacific Basin free troposphere, *Atmos. Environ.*, **28**, 951-960.

Ravishankara, A. R., 1997, Heterogeneous and Multiphase Chemistry in the Troposphere, *Science*, **276**, 1058-1065.

Rea, D. K., 1994, The paleoclimatic record provided by eolian deposition in the deep sea: The geologic history of wind, *Rev. Geophys.*, **32**, 159-195.

Reichardt, J., A. Ansmann, M. Serwazi, C. Weitkamp, and W. Michaelis, 1996, Unexpectedly low ozone concentration in midlatitude tropospheric ice clouds: A case study, *Geophys. Res. Lett.*, **23**, 1929-1932.

Rood, M. J., M. A. Shaw, T. V. Larson, and D. D. Covert, 1989, Ubiquitous nature of ambient metastable aerosol, *Nature*, **337**, 537-539.

Russell, P. B., T. J. Swissler, and M. P. McCormick, 1979, Methodology for error analysis and simulation of lidar aerosol measurements, *Appl. Opt.*, **18**, 3783-3797.

Sasano, Y., E. V. Browell, and S. Ismail, 1985, Error caused by using a constant extinction/backscattering ratio in the lidar solution, *Appl. Opt.*, **24**, 3929-3932.

Sasano, Y., 1996, Tropospheric aerosol extinction coefficient profiles derived from scanning lidar measurements over Tsukuba, Japan, from 1990 to 1993, *Appl. Opt.*, **35**, 4941-4952.

Sassen, K., H. Zhao, and B-K. Yu, 1989, Backscatter laser depolarization studies of simulated stratospheric aerosols: crystallized sulfuric acid droplets, *Appl. Opt.*, **28**, 3024-3029.

Seinfeld, J. H., and S. N. Pandis, 1998, *Atmospheric Chemistry and Physics: From Air Pollution to Climate Change*, Wiley-Interscience, New York, p491-544.

Shibata, T., T. Sakai, M. Hayashi, T. Ojio, S. A. Kwon, and Y. Iwasaka, 1996a, Raman lidar observations: simultaneous measurements of water vapor, temperature and aerosol vertical profiles, Part I, *J. Geomag. Geoelectr.*, **48**, 1127-1135.

Shibata, T., T. Sakai, M. Hayashi, T. Ojio, S. A. Kwon, and Y. Iwasaka, 1996b, Raman lidar observations: simultaneous measurements of water vapor, temperature and aerosol vertical profiles, Part I, *J. Geomag. Geoelectr.*, **48**, 1137-1144.

Soden, B. J., S. A. Ackerman, D. O'C. Starr, S. H. Melfi, and R. A. Ferrare, 1994, Comparison of upper tropospheric water vapor from GOES, Raman lidar, and cross-chain loran atmospheric sounding system measurements, *J. Geophys. Res.*, **99**, 21005-21016.

Takamura, T., Y. Sasano, and T. Hayasaka, 1994, Tropospheric aerosol optical properties derived from lidar, Sun photometer, and optical particle counter measurements, *Appl. Opt.*, **33**, 7132-7140.

Takano, Y. and K-N. Liou, 1989, Solar Radiative Transfer in Cirrus Cloud. Part I: Single-Scattering and Optical Properties of Hexagonal Ice Crystals, *J. Atmos. Sci.*, **46**, 3-19.

Talbot, R. W., J. E. Dibb, B. L. Lefer, J. D. Bradshaw, S. T. Sandholm, D. R. Blake, N. J. Blake, G. W. Sachse, J. E. Collins, Jr., B. G. Heikes, J. T. Merrill, G. L. Gregory, B. E. Anderson, H. B. Singh, D. C. Thornton, A. R. Bandy, and R. F. Pueschel, 1997, Chemical characteristics of continental outflow from Asia to the troposphere over the western Pacific Ocean during February – March 1994: Results from PEM-West B, *J. Geophys. Res.*, **102**, 28255-28274.

Tanaka, M., M., Shiobara, T. Nakajima, M. Yamano, and K. Arao, 1989, Aerosol Optical Characteristics in the Yellow Sand Events Observed in May, 1982 at Nagasaki - Part I Observations, *J. Meteorol. Soc. Japan*, **67**, 267-278.

Tang, I. N. and H. R. Munkelwitz, and J. G. Davis, 1978, Aerosol growth studies - IV. Phase transformation of mixed salt aerosols in a moist atmosphere, *Atmos. Environ.*, **9**, 505-511.

Tang, I. N. and H. R. Munkelwitz, 1993, Composition and temperature dependence of the deliquescence properties of hygroscopic aerosols, *Atmos. Environ.*, **27A**, 467-473.

Tang, I. N. and H. R. Munkelwitz, 1994, Water activities, densities, and refractive indices of aqueous sulfates and sodium nitrate droplets of atmospheric importance, *J. Geophys. Res.*, **99**, 18801-18808.

Tang, I. N., 1996, Chemical and size effects of hygroscopic aerosols on light scattering coefficient, *J. Geophys. Res.*, **101**, 19245-19250.

Toon, O. B. and J. B. Pollack, 1976, A global average model of atmospheric aerosols for radiative transfer calculations, *J. Appl. Meteorol.*, **15**, 225-246.

Tsunogai, S. and T. Kondo, 1982, Sporadic transport and deposition of continental aerosols to the Pacific Ocean, *J. Geophys. Res.*, **87**, 8870-8874.

Twomey, S., 1977a, The Influence of Pollution on the Shortwave Albedo of Clouds, *J. Atmos. Sci.*, **34**, 1149-1152.

Twomey, S., 1977b, *Atmospheric Aerosols*, Elsevier, Amsterdam, 302pp.

Twomey, S., 1991, Aerosol, clouds and radiation, *Atmos. Environ.*, **25A**, 2435-2442.

Vaughan, G., D. P. Wareing, L. Thomas, and V. Mitev, 1988, Humidity measurement in the free troposphere using Raman backscatter, *Q. J. Roy. Meteorol. Soc.*, **114**, 1471-1484.

Wandinger, U., 1998, Multiple-scattering influence on extinction- and backscatter-coefficient measurements with Raman and high-spectral-resolution lidars, *Appl. Opt.*, **37**, 417-427.

Warneck, P., 1988, *Chemistry of the Natural Atmosphere*, Academic Press, San Diego, 575pp.

Warren, S. G., 1984, Optical constants of ice from the ultraviolet to the microwave, *Appl. Opt.*, **23**, 1206-1225.

Whiteman, D. N., S. H. Melfi, and R. A. Ferrare, 1992, Raman lidar system for the measurement of water vapor and aerosols in the Earth's atmosphere, *Appl. Opt.*, **31**, 3068-3082.

Xiao, H., G. R. Carmichael, and J. Durchenwald, 1997, Long-range transport of SO_X and dust in East Asia during the PEM B Experiment, *J. Geophys. Res.*, **102**, 28589-28612.

Yamato, M. and A. Ono, 1989, Chemical and Physical Properties of Stratospheric Aerosol Particles in the Vicinity of Tropopause Folding, *J. Meteorol. Soc. Japan*, **67**, 147-165.

Zhang, Y., Y. Sunwoo, V. Kotamarthi, and G. R. Carmichael, 1994, Photochemical Oxidant Processes in the Presence of Dust: An Evaluation of the Impact of Dust on Particulate Nitrate and Ozone Formation, *J. Appl. Meteorol.*, **33**, 813-824.

Zhang, Y. and G. R. Carmichael, 1999, The Role of Mineral Aerosol in Tropospheric Chemistry in East Asia-A model study, *J. Appl. Meteorol.*, **38**, 353-366.

Zhuang, G., Y. Zhen, R. A. Duce, and P. R. Brown, 1992, Link between iron and sulphur cycles suggested by detection of Fe(II) in remote marine aerosols, *Nature*, **355**, 537-539.